Techniques for Compressible Flow Calculations on Multi-Zone Grids

by

Taekyu Reu

Dissertation submitted to the Faculty of the

Virginia Polytechnic Institute and State University

in partial fulfillment of the requirements for the degree of

Doctor of Philosophy

in

Aerospace Engineering

APPROVED:

Dr. Robert W. Walters, Chairman

Dr. Bernard Grossman

Dr. Joseph A. Schetz

Dr. Roger L. Simpson

Dr. Rakesh K. Kapania

August, 1988

Blacksburg, Virginia

Techniques for Compressible Flow Calculations on Multi-Zone Grids

by

Taekyu Reu

Dr. Robert W. Walters, Chairman

Aerospace Engineering

(ABSTRACT)

In order to simulate inviscid/viscous compressible flowfields about 3-D realistic aerodynamic bodies, the combined use of an implicit, upwind biased real gas scheme with 3-D fully conservative patched grid techniques is discussed. An "equivalent" gamma formulation is implemented in order to model real gas effects in Van Leer's flux vector splitting (FVS) and Roe's flux difference splitting (FDS) scheme. A hybrid approximate-factorization (AF)/relaxation algorithm is used as an efficient solver of the Euler, parabolized Navier-Stokes, and thin-layer Navier-Stokes equations. Two different approaches, clipping and Ramshaw's rezoning algorithms, for performing a conservative flux calculation are described and compared in terms of numerical efficiency. In order to show the real gas effects in the upwind schemes, two test problems are solved. Also to demonstrate the capability of the patched grid approach, the turbulent flowfield about 3-D analytic forebody is calculated as another test problem. Due to the poor results of the Baldwin-Lomax turbulent model for separated flows, only the attached flowfield is considered in the analytic forebody calculation. Finally, as applications of this approach, the inviscid/viscous flowfields about several

aerodynamic bodies are calculated including a generic hypersonic aircraft, a model of the SR-71 aircraft, and F-18 forebody with strakes.

Acknowledgements

The author would like to express his deepest appreciation to his advisor, Dr. Robert W. Walters for his invaluable aid and advice throughout this study. Without his tremendous support, it would have been difficult to accomplish this work. He also wishes to thank Dr. B. Grossman, Dr. J.A. Schetz, Dr. R.L. Simpson, and Dr. R.K. Kapania for serving on the Advisory Committee and for their comments and suggestions on this study.

He wishes to thank Dr. J.L. Thomas of the NASA Langley Rearch Center for his assitances and suggestions.

He also would like to thank his fellow graduate students who shared their time in everyway.

Finally, he would like to thank his parents and especially his wife, , for their support and patient throughout the course of this study.

Table of Contents

1. Introduction 1

2. Governing Equations 5

2.1 Thin-layer Approximation 6

2.2 Finite Volume Discretization 7

2.3 Turbulence Simulation 11

3. Conservative zonal boundary treatment 12

3.1 Flux Conservation Condition 12

3.2 Clipping Algorithm 14

3.3 Ramshaw Algorithm 16

4. Upwind Schemes 19

4.1 Real Gas Effects 20

4.2 Van Leer Flux-Vector Splitting 22

4.3 Roe's Flux Difference Splitting 25

4.4 Spatial Accuracy 36

4.5 Extension to Viscous Flows 38

5. Implicit Algorithm **40**

5.1 Euler Implicit Time Integration 40

5.2 Evaluation of the Jacobians for a Real Gas. 42

5.2.1 Inviscid Jacobians of Van Leer's FVS 42

5.2.2 Inviscid Jacobians of Roe's FDS 44

5.2.3 Viscous Jacobian terms 45

5.3 Hybrid Algorithm 46

5.4 Modified Algorithm for Space Marching 48

5.5 Application to Multi-Zone grids 50

6. Results and Discussions **51**

6.1 Time Comparison 51

6.2 Test Problems 52

6.2.1 Supersonic 2-D Wedge Problem 52

6.2.2 Shock-Boundary Layer Interaction 53

6.2.3 Analytic Forebody 54

6.3 Applications 55

6.3.1 Hypersonic Aircraft 55

6.3.2 Model SR-71 56

6.3.3. F-18 Forebody with Strakes 57

7. Concluding Remarks **59**

References **61**

Figures 66

Tables 100

Appendix A. Nondimensionalization of the Navier-Stokes Equations 102

Appendix B. Coordinate Transformation 107

Appendix C. Flow Chart of the Clipping Algorithm 112

Appendix D. Ramshaw algorithm 114

Vita 119

List of Illustrations

Figure 1. Body-fitted coodinate system..... 67

Figure 2. Cell-centered finite volume formulation..... 68

Figure 3. Schemetic view of a patched grid..... 69

Figure 4. Arbitrary overlapping cell faces at a zonal interface..... 70

Figure 5. Clipping procedure..... 71

Figure 6. Special considerations for Ramshaw algorithm..... 72

Figure 7. Enlarged view of a 10 ^{o} wedge patched grid..... 73

Figure 8. Lower surface temperature distribution of the 10 ^{o} wedge..... 74

Figure 9. Temperature contours of (a) Roe's FDS and (b) Van Leer's FVS. 75

Figure 10. Two zone patched grid of a flat plate..... 76

Figure 11. Pressure contours of shock-boundary layer interaction problem.. 77

Figure 12. Comparison of wall skin friction coefficient distribution with experiment..... 78

Figure 13. Two zone patched grid of an analytic forebody..... 79

Figure 14. Pressure contours in the symmetry plane of the analytic forebody. 80

Figure 15. Comparison of the longitudinal surface pressure distribution with experiment (Ref.57) in the symmetry plane. 81

Figure 16. Comparison of pressure contours in the first plane downstream of the zonal interface with single grid pressure contours..... 82

Figure 17. Highly stretched two zone patched grid of the analytic forebody. 83

Figure 18. Pressure contours in the symmetry plane of the analytic forebody. 84

Figure 19. Comparison of the longitudinal surface pressure distribution with experiment (Ref.57) in the symmetry plane. 85

Figure 20. Pressure contours in the planes just (a) ahead of and (b) behind the zonal interface. 86

Figure 21. (a) Hypersonic aircraft (single grid from Ref.8), (b) zone 1 cross plane grid, and (c) zone 2 cross plane grid at the zonal interface. 87

Figure 22. Pressure contours in the cross planes immediately (a) ahead of and (b) behind the zonal interface of the hypersonic aircraft..... 88

Figure 23. Pressure contours in the last plane of the hypersonic aircraft..... 89

Figure 24. Model SR-71. 90

Figure 25. Pressure contours in the cross planes just (a) ahead of and (b) behind the first zonal interface. 91

Figure 26. Pressure contours in the cross planes just (a) ahead of and (b) behind the third zonal interface..... 92

Figure 27. Pressure contours in the last plane. 93

Figure 28. Pressure contours in the plane of symmetry..... 94

Figure 29. Computational Grid of F-18, (a) enlarged view and (b) surface grid95

Figure 30. F-18 cross plane grid of (a) zone 1 and (b) zone 2 at the zonal interface. 96

Figure 31. Pressure contours in the plane of symmetry..... 97

Figure 32. Enlarged view of pressure contours in the cross plane just (a) ahead of and (b) behind the zonal interface. 98

Figure 33. (a) Pressure contours in the last plane and (b) the enlarged view. 99

Table 1. Relative CPU Time of Conservative Interpolation..... 101

List of Symbols

$\tilde{A}$ .....Jacobian matrix based on Roe averaging

a .....speed of sound

e.....internal energy per unit mass

e_0.....total energy per unit mass

F, G, H.....inviscid flux vector in Cartesian coordinates

$\hat{F}, \hat{G}, \hat{H}$.....inviscid flux vector in a body fitted coordinates

F_v, G_v, H_v.....viscous flux vector in Cartesian coordinates

h_0 .....total enthalpy per unit mass

J .....Jacobian of a transformation matrix

k .....thermal conductivity

M.....Mach number

p .....static pressure

Pr.....Prandtl number

q .....speed, ($= \sqrt{u^2 + v^2 + w^2}$)

Q .....vector of conservative variables

R.....steady state residual

Re.....Reynolds number

S.....surface area

t.....time

T.....static temperature or transformation matrix

u, v, w .....velocity component in Cartesian coordinates

$\bar{u}$.....contravariant velocity in body fitted coordinates

V .....cell volume

x, y, z.....Cartesian coodinate system

Greek symbols

α .....angle of attack

γ .....specific heat ratio for a perfect gas

$\tilde{\gamma}$, Γ.....equivalent gamma

ε.....tolerance

ξ, η, ζ.....body fitted coordinate system

λ .....eigenvalue of Jacobian matrix

μ.....molecular viscosity

ρ .....density

ω .....Vigneron coefficient

Subscripts

i, j, k .....indices of body fitted coordinate system

∞ .....free stream condition

Superscripts

* .....local Cartesian coordinates value

$\wedge$.....body fitted coordinates value

$\sim$ .....real gas value or Roe averaged value

$-$ .....dimensional value

1. Introduction

In recent years, with the advancement in computational fluid dynamics (CFD) and computer hardware, the numerical analysis of 3-D compressible inviscid/viscous flow associated with realistic aerodynamic bodies has been investigated (Ref.1-5). Also, due to the renewed interest in the hypersonic flight regime, hypersonic internal/external flowfields have been studied (Ref.6-8) and the development of more accurate and efficient computer codes, as design tools, which can resolve even the engine-airframe integration problem has been needed because of the difficulty of simulating the wide range of the actual hypersonic flight conditions in a wind tunnel (Ref.9). However, under high-altitude and hypersonic flight condtions, the external flow field generally experiences strong shock waves and chemical reactions due to shock heating so that the perfect gas assumption is no longer valid and real gas effects need to be considered. Also computational grids should be properly clustered and stretched to get better

solutions around 3-D complex aerodynamic bodies, which may not be achieved by a single grid generation code.

The early efforts (Refs.10-11) to compute 3-D high-speed flow fields with real gas effects were based on the central difference schemes which need user controlled artifical viscosity to capture discontinuities. Due to the false dissipation caused by the artificial viscosity, it is often necessary to tune the artifical viscosity for every calculation, which makes these schemes less robust. Hence, upwind schemes (Refs.12-20) are used here due to their shock capturing properties. The upwind schemes numerically simulate the signal propagation properties of hyperbolic equations, and with the careful treatment of viscous terms, these schemes are quite robust, capable of solving problems across a wide Mach number range. Recently, upwind schemes have been applied to real gas computations by several researchers (Refs.21-24). Grossman and Walters (Ref.21-22) developed an "equivalent" gamma formulation to model real gas effects in upwind schemes and applied it to equilibrium air calculations. In their calculations, the simplified curve fits for the equilibrium air properties, developed by Srinivasan et.(Ref.25) were used as the equilibrium air equation of state.

In addition to real gas effects in high-speed flows, another difficulty in flow field simulation (especially around a 3-D complex geometry) is the generation of a proper computational grid which is sufficiently stretched and clustered to resolve the flow field. In order to overcome this problem, several approaches have been investigated including the Cartesian grid, unstructured grid and composite (multiple or multi-zone) grid approach. The Cartesian grid (Refs.26-27) is trivial

to generate, but it does not cluster efficiently to resolve boundary layers on curved surfaces. The unstructured grid (Refs.28-30) has the most flexibility in grid generation approaches. However, it requires more memory and due to its ordering, it is less amenable to the use of iterative algorithms such as approximate factorization (AF) and line relaxation schemes. So the unstructured grid approach is still impractical for 3-D viscous flow calculations. The composite grid (multi-zone grid) approach has recently been used to generate grids about 3-D complex geometries. Usually grid continuity is forced at zonal boundaries for conventional single grid codes (Refs.31-33). Here, however, grids are generated independently in each zone so that grid lines do not have to be continuous at zonal boundaries. Each zone can be overset or patched at a zonal boundary to get more flexibilty in the grid generation process (Refs.34-42). With a zonal approach, conservative or non-conservative calculations can be performed depending on the interpolation at the zonal interface. Here, only conservative numerical methods for zonal interpolation are discussed. Beside the ease of the grid generation, other advantages of the zonal approaches are that different equations may be solved in each zone (Ref.43) and that different numerical schemes can be used in each zone (Ref.39).

In this study, upwind schemes with real gas effects and the patched grid approach are discussed and used to calculate high-speed flow fields about 3-D complex aerodynamic bodies. The implicit upwind finite volume scheme with the efficient iteration strategy described by Newsome et. al (Ref.44) has been implemented, which was developed for the thin-layer Navier-Stokes, parabolized

Navier-Stokes, and the Euler equations. The flux vector splitting scheme (FVS) of Van Leer and the flux difference splitting scheme (FDS) of Roe were modified to simulate real gas effects by following the approach of Grossman and Walters (Ref. 21-22). Also, to flexibly handle 3-D geometries, the multi-zone grid, particularly the patched grid approach, has been investigated. At the zonal interface, the spatial fluxes of mass, momentum, and energy normal to the interface are interpolated to maintain the accuracy of the solution across the zonal boundary. This approach is fully conservative so that strong discontinuities can move through a zonal boundary very smoothly. For interpolating the flux at a zonal interface, two different approaches, which are the clipping algorithm (Ref.45) and the Ramshaw algorithm (Ref.46-47), are described and compared in terms of numerical efficiency. The Ramshaw algorithm is implemented for most of the 3-D calculations in this study due to its efficiency.

The following sections discuss the governing equations and 'real' gas considerations, efficient conservative interpolations on arbitrary zonal meshes, and an implicit relaxation procedure. Finally, several applications are presented to show the capabilty of the patched grid approach.

2. Governing Equations

As mentioned in Introduction, the external hypersonic flow field generally experiences chemical reactions including dissociation and ionization proceeding at finite rates, diffusion of atoms and ions, and recombination processes due to high temperature. Governing equations for this kind of flows - nonequilibrium reacting flows, can be found in Ref.61. In order to simplify the problem in this study, an equilbrium gas with equimolecular weights (Ref.61-62) is considered. Furthermore, by assuming equimolecular weights in molecular diffusion terms of the governing equations (Ref.61-62) and the unity Lewis number which is the ratio of coefficients for diffusion of mass to diffusion of heat (Ref.62), the governing equations take the familar forms for an one-component gas, the Navier-Stokes equations, shown in Appendix A.

2.1 Thin-layer Approximation

In order to solve the full Navier-Stokes equations, a grid should be appropriately clustered in all directions in order to resolve the viscous terms adequately. However, for 3-D compressible flow calculations, it is generally impractical due to the required computer memory and CPU time. However, at high Reynolds numbers, the dominant viscous effects are the results of diffusion normal to a body surface. Hence, for many problems, it is natural to use the thin-layer Navier-Stokes equations as an approximation to the complete Navier-Stokes equations. In the thin-layer approximation, the viscous terms containing derivatives parallel to the body surfaces are neglected, but all other terms in the momentum equations are retained. One advantage of retaining the normal momentum equation is that separated flow regions can be computed in a straight-forward manner, even though the thin-layer approximation is not valid in massively separated flow regions.

The nondimensionalized full Naver-Stokes equations in a body-fitted coordinates system shown in Fig.1 can be written as

$$\frac{1}{J}\frac{\partial Q}{\partial t}+\frac{\partial}{\partial \xi}(\hat{F}-\hat{F}_v)+\frac{\partial}{\partial \eta}(\hat{G}-\hat{G}_v)+\frac{\partial}{\partial \zeta}(\hat{H}-\hat{H}_v)=0 \qquad (1)$$

where $Q=(\rho, \rho u, \rho v, \rho w, \rho e_0)$ is the vector of conserved variables. The flux vectors are defined in Appendix A.

Applying the thin-layer approximation to the above equations, the nondimensionalized thin-layer Navier-Stokes equations in the body-fitted coordinates can be written in the conservative form as

$$\frac{1}{J}\frac{\partial Q}{\partial t}+\frac{\partial \hat{F}}{\partial \xi}+\frac{\partial \hat{G}}{\partial \eta}+\frac{\partial}{\partial \zeta}(\hat{H}-\hat{H}_v)=0 \tag{2}$$

where J is the Jacobian of the transformation matrix. The nondimensionalization and coordinate transformation are explained in Appendices A and B.

2.2 Finite Volume Discretization

Even though the governing equations in Eq.(2) are commonly written in a differential form, finite volume formulation is based on the integral form which can be written as

$$\frac{\partial}{\partial t}\iiint Q\,dV+\iint \vec{F}\bullet\hat{n}\,dS=0 \tag{3}$$

where $\vec{F}$ is the flux vector and $\hat{n}$ is a unit normal vector pointing outward from the surface, S, bounding the volume, V.

By applying Eq.(3) to a finite volume which is a hexahedral cell formed by the grid points as shown in Fig.2 , and by assigning computational coordinates

(ξ, η, ζ) to the cell indices (i, j, k), the surface integral term of Eq.(3) can be discretized as

$$
\begin{aligned}
\iint \vec{F}\bullet\hat{n}\,dS \cong\ & [(\vec{F}\bullet\hat{n})\,|\Delta S|\,]_{i+\frac{1}{2}} + [(\vec{F}\bullet\hat{n})\,|\Delta S|\,]_{i-\frac{1}{2}} + [(\vec{F}\bullet\hat{n})\,|\Delta S|\,]_{j+\frac{1}{2}} \\
& + [(\vec{F}\bullet\hat{n})\,|\Delta S|\,]_{j-\frac{1}{2}} + [(\vec{F}\bullet\hat{n})\,|\Delta S|\,]_{k+\frac{1}{2}} + [(\vec{F}\bullet\hat{n})\,|\Delta S|\,]_{k-\frac{1}{2}} \\
=\ & \left[\left(\vec{F}\bullet\frac{\nabla\xi}{|\nabla\xi|}\right)\frac{|\nabla\xi|}{J}\right]_{i+\frac{1}{2}} - \left[\left(\vec{F}\bullet\frac{\nabla\xi}{|\nabla\xi|}\right)\frac{|\nabla\xi|}{J}\right]_{i-\frac{1}{2}} \\
& + \left[\left(\vec{F}\bullet\frac{\nabla\eta}{|\nabla\eta|}\right)\frac{|\nabla\eta|}{J}\right]_{j+\frac{1}{2}} - \left[\left(\vec{F}\bullet\frac{\nabla\eta}{|\nabla\eta|}\right)\frac{|\nabla\eta|}{J}\right]_{j-\frac{1}{2}} \\
& + \left[\left(\vec{F}\bullet\frac{\nabla\zeta}{|\nabla\zeta|}\right)\frac{|\nabla\zeta|}{J}\right]_{k+\frac{1}{2}} - \left[\left(\vec{F}\bullet\frac{\nabla\zeta}{|\nabla\zeta|}\right)\frac{|\nabla\zeta|}{J}\right]_{k-\frac{1}{2}} \\
=\ & \hat{F}_{i+\frac{1}{2}} - \hat{F}_{i-\frac{1}{2}} + \hat{G}_{j+\frac{1}{2}} - \hat{G}_{j-\frac{1}{2}} + (\hat{H} - \hat{H}_v)_{k+\frac{1}{2}} - (\hat{H} - \hat{H}_v)_{k-\frac{1}{2}}
\end{aligned}
$$

For convenience, whenever the logical indices are simply i, j, or k, they are dropped. In the above, $\dfrac{|\nabla\xi|}{J}$ is the directed area of the cell face and $\dfrac{\nabla\xi}{|\nabla\xi|}$ is the unit normal vector of an $\xi = constant$ cell face. According to this interpretation, all metric terms are calculated geometrically. For example, the term $\dfrac{1}{J}$ corresponds to the cell volume V which can be easily calculated in the physical domain. Similarly, the volume integral of Eq.(3) can be written as

$$
\frac{\partial}{\partial t}\iiint Q\,dV = \frac{\partial < Q >_{ijk}}{\partial t} V_{ijk}
$$

where the quantity $< Q >_{ijk}$ is regarded as a cell-averaged value, i.e.,

$$< Q >_{ijk} = [\frac{1}{V}\iiint_V Q\, dV]_{ijk}$$

Using the above results and replacing the cell-averaged value by the cell-centered value, the semi-discrete conservative form of the governing equations is obtained.

$$\begin{aligned}(V\frac{\partial Q}{\partial t})_{i,j,k} + (\hat{F}_{i+\frac{1}{2},j,k} - \hat{F}_{i-\frac{1}{2},j,k}) + (\hat{G}_{i,j+\frac{1}{2},k} - \hat{G}_{i,j-\frac{1}{2},k}) \\ + (\hat{H} - \hat{H}_v)_{i,j,k+\frac{1}{2}} - (\hat{H} - \hat{H}_v)_{i,j,k-\frac{1}{2}} = 0\end{aligned} \tag{4}$$

where

$$Q = \begin{bmatrix} \rho \\ \rho u \\ \rho v \\ \rho w \\ \rho e_0 \end{bmatrix} \qquad \hat{F},\ \hat{G},\ \hat{H} = \frac{|\nabla \hat{k}|}{J} \begin{bmatrix} \rho\bar{u} \\ \rho u\bar{u} + \hat{k}_x p \\ \rho v\bar{u} + \hat{k}_y p \\ \rho w\bar{u} + \hat{k}_z p \\ (\rho e_0 + p)\bar{u} \end{bmatrix}$$

$$\bar{u} = \hat{k}_x u + \hat{k}_y v + \hat{k}_z w$$

$$\hat{k} = \frac{k}{|\nabla k|} \qquad \textit{for } k = \xi, \eta, \zeta \textit{ respectively}$$

and

$$\hat{H}_v = \frac{M_\infty \mu}{Re_L} \frac{|\nabla\zeta|^2}{J} \begin{bmatrix} 0 \\ u_\zeta + \hat{\zeta}_x \phi \\ v_\zeta + \hat{\zeta}_y \phi \\ w_\zeta + \hat{\zeta}_z \phi \\ [(\frac{q^2}{2})_\zeta + \alpha_\zeta] + W\phi \end{bmatrix}$$

where

$$\phi = (\hat{\zeta}_x u_\zeta + \hat{\zeta}_y v_\zeta + \hat{\zeta}_z w_\zeta)/3$$

$$\alpha_\zeta = \frac{\bar{k}\bar{T}_\infty}{\bar{\mu}\bar{a}_\infty^2} \frac{\partial T}{\partial \zeta} = \frac{1}{Pr(\gamma - 1)} \frac{\partial a^2}{\partial \zeta} \quad \textit{(for a perfect gas)}$$

$$Re_L = \frac{\bar{\rho}_\infty \bar{q}_\infty \bar{L}}{\bar{\mu}_\infty} \qquad M_\infty = \frac{\bar{q}_\infty}{\bar{a}_\infty} \qquad q^2 = u^2 + v^2 + w^2$$

$$W = \hat{\zeta}_x u + \hat{\zeta}_y v + \hat{\zeta}_z w$$

This approximation is fully conservative so that it is valid in the presence of the discontinuities such as shocks and contact surfaces.

To close the equation set, an equation of state must be employed. For a perfect gas, the pressure is obtained from the perfect gas law and the molecular viscosity μ is calculated from Sutherland's law. Also, a Prandtl number is assumed to be constant to determine the thermal conductivity. For an equilibrium air model, the simplified curve fits developed by Srinivasan et.al (Ref.25) are used as the equation of state to calculate the thermodynamic properties of equilbrium air. (See Appendix A for details.)

2.3 Turbulence Simulation

By using a simple eddy viscosity model, the effects of turbulence can be simulated. In Eq.(4), the molecular viscosity μ and the thermal conductivity k are replaced by an effective viscosity μ_e and an effective conductivity k_e:

$$\mu_e = \mu + \mu_t = \mu(1 + \frac{\mu_t}{\mu})$$

$$k_e = k + k_t = \frac{C_p}{Pr}\mu + \frac{C_p}{Pr_t}\mu_t \qquad (5)$$

$$= \frac{C_p\mu}{Pr}(1 + \frac{Pr}{Pr_t}\frac{\mu_t}{\mu})$$

where μ_t is the turbulent viscosity and Pr_t is the turbulent Prandtl number. In this study, only the perfect gas case was considered with $Pr = 0.72$ and $Pr_t = 0.9$. To evaluate the turbulent viscosity, μ_t, the Baldwin-Lomax two layer algebraic eddy viscosity model (Ref.48-49) is employed. In the outer region of the Baldwin-Lomax turbulence model, the distribution of vorticity is used to determine length scales so that the necessity for finding the edge of the boundary layer is avoided.

3. Conservative zonal boundary treatment

3.1 Flux Conservation Condition

In the case of multi-zone calculations, each zone has an independently generated grid which causes a grid discontinuity at a zonal interface as shown Fig.3. In order to satisfy the conservation law at the zonal boundary, the surface integral of Eq.(3) at the interface should be same whether it is computed in zone 1 or in zone 2, which means the total flux should be conserved through the zonal boundary.

Using a superscript to indicate the zone number as shown in Fig.3, the conservation requirement on an $\xi = constant$ surface becomes

$$\sum_{j^1}^{J^1}\sum_{k^1}^{K^1} < \hat{F} >_{j^1k^1} \Delta S_{j^1k^1} = \sum_{j^2}^{J^2}\sum_{k^2}^{K^2} < \hat{F} >_{j^2k^2} \Delta S_{j^2k^2} \qquad (6)$$

where $< \hat{F} >$ is the area-averaged flux at a cell face. Even though this constraint does ensure flux conservation across the zonal interface, it does not restrict the local transport of flux from cell to cell across the patched grid boundary. This can be accomplished by enforcing conservation on a local level which was presented by Hessenius and Rai (Ref.35). Conservation on the (j^2, k^2) cell face requires that

$$[< \hat{F} > \Delta S]_{j^2k^2} = \int\int_{\Delta S_{j^2k^2}} [(\vec{F} \cdot \hat{n}) dS]^1$$

This integration on the right hand side of the above equation may be replaced by a discrete sum over the number of cells in Zone 1 that overlap the (j,k) cell face in Zone 2, i.e.

$$[< \hat{F} > \Delta S]_{j^2k^2} = \sum_{j^1}\sum_{k^1} [< \hat{F} > \Delta S^o]_{j^1k^1} \tag{7}$$

where ΔS^o is the area of the polygon that overlaps the (j^1, k^1) cell face in Zone 1 and the (j^2, k^2) cell face in Zone 2, and $[< \hat{F} > \Delta S^o]_{j^1k^1}$ is the contribution of the (j^1, k^1) cell face to the flux of the (j^2, k^2) cell face in Zone 2. For computational purposes, the above relation can be written as

$$\hat{F}_{j^2k^2} = \sum_{j^1}\sum_{k^1} \hat{F}_{j^1k^1} N_{j^1k^1}^{j^2k^2} \tag{8}$$

where

$$N_{j^1k^1}^{j^2k^2} = \frac{\Delta S^o}{\Delta S^{j^1k^1}}$$

is a weight function which varies between 0 and 1. Assuming that the fluxes in zone 1 are known, the conservative interpolation problem is reduced to the problem of finding the area of overlap as seen in Eq.(8). In this study, two different algorithms are considered to calculate the overlapping areas.

3.2 Clipping Algorithm

At a zonal interface, the cell faces of both zone are arbitrarily overlapped. Fig.4 shows two typical overlapping cell faces. As a simple way to calculate the area of overlap, ΔS^o , a clipping algorithm is considered which is widely used in the field of computer graphics to remove the part of an image that lies outside of a graphics window (Ref.45). This technique was first applied to computational fluid dynamic applications by Hessenius and Rai (Ref.35). The idea is to find the vertex points of the overlapping polygon by clipping the part of the cell faces not common to both zones as seen in Fig.5. Instead of subdividing each cell face into two triangles as done by Hessenius and Rai, quadrilateral cell faces were directly used to calculate overlapping areas. This is possible and more efficient, because the cell faces and the polygons resulting from the clipping are always convex and

all vertex points on a zonal boundary are coplanar. A flowchart of the clipping algorithm used in this study, which is similar to the one in Ref.35, can be found in Appendix C. Given the ordered vertex points, the area of overlap can be obtained from

$$\Delta S^o = \frac{1}{2} \sum_{i=1}^{n} (y_i z_{i+1} - y_{i+1} z_i) \tag{9}$$

In addition to the clipping algorithm, a proper searching algorithm should be employed to determine which cells in zone 1 overlap a zone 2 cell. In this study, the summation over all of the cell faces in zone 1 for every cell face in zone 2 was implemented, i.e.,

$$\sum_{j^2=1}^{J^2} \sum_{k^2=1}^{K^2} \hat{F}_{j^2 k^2} = \sum_{j^2=1}^{J^2} \sum_{k^2=1}^{K^2} \sum_{j^1=1}^{J^1} \sum_{k^1=1}^{K^1} \hat{F}_{j^1 k^1} N_{j^1 k^1}^{j^2 k^2} \tag{10}$$

Even though this algorithm has been applied in 3-D inviscid flow-field calculations, it is not practical. It can be seen from Eq.(10) that doubling the mesh size in both zones results in an increase in work by 2^4. The CPU time can be reduced by using a efficient searching algorithm such as a tree search algorithm (Ref.55).

3.3 Ramshaw Algorithm

In a recent paper by John Ramshaw (Ref.46), a novel and numerically efficient approach for finding the area of overlap was discussed. This idea was first proposed by Dukowicz (Ref.47) and later, simplified by Ramshaw for Lagrangian hydrodynamics calculations to resolve rezoning problems. The details and programming considerations are discussed in Appendix D. A brief review of the implementation described by him follows. He observed that the overlap area lies entirely within a single cell of zone 1 and a single cell of zone 2 and that it is constructed with the edge segments of the zone 1 cell faces and the zone 2 cell faces as seen in Fig.4. Moreover, since the area of the polygon given in Eq.(9) is a sum of the contributions from its edges, the entire determination of the areas of all polygons formed (and therefore all of the weights, N_{j1k1}^{j2k2}) can be found by a single sweep over the zone 1 mesh lines and the zone 2 mesh lines. Since an edge of the polygon is common to two overlapping areas, the left one (L) and the right one (R), it is convenient to compute the contribution of a line segment to two overlapping areas at the same time. In a global point of view, the overlapping area of polygon P can be expressed as

$$\Delta S^{o} = \frac{1}{2} \sum_{s} \varepsilon_{s}^{P} (y_1^s z_2^s - y_2^s z_1^s) \tag{11}$$

where the summation is over all the sides of P and where

$\varepsilon_s^P = +1$; P lies to the left of side s

$\varepsilon_s^P = -1$; P lies to the right of side s

When sweeping along the grid lines of zone 1, the contribution to the flux $\hat{F}_{j^2k^2}$ of zone 2 is

$$\Delta_s^o = \frac{1}{2}(<\hat{F}>_L - <\hat{F}>_R)(y_1^s z_2^s - y_2^s z_1^s)$$

where, $<\hat{F}>_L$ and $<\hat{F}>_R$ are cell area-averaged fluxes of zone 1 which lie to the left and right of the sweeping line segment of zone 1. During the sweep along the grid lines of zone 2, the contribution to the left cell flux of zone 2 is

$$\Delta_s^N = \frac{1}{2}<\hat{F}>_o (y_1^s z_2^s - y_2^s z_1^s)$$

and the contribution to the right cell flux is $-\Delta_s^N$. $<\hat{F}>_o$ is the cell area-averaged flux of zone 1 containing the line segment s. Finally, the total contribution to the surface integral in zone 2 is given by

$$\sum_{j^2=1}^{J^2}\sum_{k^2=1}^{K^2} \hat{F}_{j^2k^2} = \sum_{j^2=1}^{J^2}\sum_{k^2=1}^{K^2} \varepsilon_s^P \Delta_s^N + \sum_{j^1=1}^{J^1}\sum_{k^1=1}^{K^1} \Delta_s^o \qquad (12)$$

It can be seen from Eq.(12) that doubling the grid size in each direction in both zones increases the computational work by only a factor 2^2 in contrast with 2^4 increase associated with clipping via Eq.(10). It should be emphasized that the results produced by the clipping procedure and the Ramshaw algorithm are

identical. Therefore, due to the efficiency of the Ramshaw algorithm, it was used in most of the applications of the multi-zone algorithm.

4. Upwind Schemes

In order to discritize the inviscid flux terms, upwind schemes are considered. Due to the natural dissipation of upwind schemes, they are used here for the hyperbolic part of the conservation equations along with a central difference treatment of the viscous terms. In addition, since the implicit coefficient matrix of an upwind scheme is nearly diagonally dominant, relaxation algorithms can be implemented. In this study, two typical upwind schemes, the Van Leer Flux Vector Split (FVS) scheme (Ref.13) and Roe's Flux Difference Split (FDS) scheme (Ref.12), are considered. Also, to modify the upwind schemes for a real gas, the "equivalent" gamma formulation developed by Grossman and Walters (Ref.21-22) is fully implemented. An advantage of this formulation is that the existing perfect gas program can be easily modified for a real gas calculation.

4.1 Real Gas Effects

In order to explain the real gas effect in upwind schemes, the 1-D Euler equations in a Cartesian coordinate system are considered,

$$\frac{\partial Q}{\partial t} + \frac{\partial F}{\partial x} = 0 \tag{13}$$

where

$$Q = \begin{bmatrix} \rho \\ \rho u \\ \rho e_0 \end{bmatrix} \qquad F = \begin{bmatrix} \rho u \\ \rho u^2 + p \\ (\rho e_0 + p)u \end{bmatrix}$$

A general equation of state is given by

$$p = p(\rho, e) \tag{14}$$

and the speed of sound is given by definition as

$$a^2 = \left(\frac{\partial p}{\partial \rho}\right)_s \tag{15}$$

Since Eq.(14) is given as $p = (\gamma - 1)\rho e$ for a perfect gas, an equivalent gamma, $\tilde{\gamma}$, can be considered for a real gas such that

$$p = (\tilde{\gamma} - 1)\rho e \tag{16}$$

where obviously $\tilde{\gamma} = \tilde{\gamma}(\rho, e)$. Introducing $\tilde{\gamma}$, Eq(16) is still valid as a general equation of state and it is useful for evaluating the Jacobian matrix. Similarly, another gamma, Γ, can be defined based on the speed of sound as

$$a^2 = \Gamma \frac{p}{\rho} \tag{17}$$

where $\Gamma = \Gamma(\rho, e)$.

Using Eq(16), the Jacobian matrix can be obtained as

$$A = \frac{\partial F}{\partial Q} = \tilde{A} + \rho e \tilde{\gamma}_\rho \begin{bmatrix} 0 & 0 & 0 \\ 1 & 0 & 0 \\ u & 0 & 0 \end{bmatrix} - e\tilde{\gamma}_e \begin{bmatrix} 0 & 0 & 0 \\ e_0 - u^2 & u & -1 \\ u(e_0 - u^2) & u^2 & -u \end{bmatrix} \tag{18}$$

where

$$\tilde{A} = \begin{bmatrix} 0 & 1 & 0 \\ (\tilde{\gamma} - 3)u^2/2 & (3 - \tilde{\gamma})u & \tilde{\gamma} - 1 \\ -\tilde{\gamma}uE + (\tilde{\gamma} - 1)u^3 & \tilde{\gamma}E - 3(\tilde{\gamma} - 1)u^2/2 & \tilde{\gamma}u \end{bmatrix} \tag{19}$$

Since $\tilde{\gamma} = \gamma = constant$ for a perfect gas, $A = \tilde{A}$ and $AQ = F$. However, for a real gas,

$$AQ = F + \rho e \tilde{\gamma}_p \begin{bmatrix} 0 \\ \rho u \\ \rho \end{bmatrix} \neq F$$

Thus the Euler equations are not homogeneous for a real gas , as is the case for a perfect gas, and the existing perfect-gas flux-split algorithms are not generally applicable for a real gas. However, by introducing the "equivalent" gamma formulation with physically reasonable assumptions, the upwind schemes can be modified for a real gas. In following two sections, the modified forms of the upwind schemes - Van Leer FVS and Roe FDS for a real gas are obtained and discussed.

4.2 Van Leer Flux-Vector Splitting

In Flux-Vector Splitting (FVS) schemes, the flux vector is split according to the characteristic direction of signal propagation. The flux vector is decomposed into two components, a forward flux F^+ and a backward flux F^-

$$F = F^+ + F^-$$

where the Jacobian matrix of F^+ has non-negative eigenvalues and the Jacobian of F^- has non-positive eigenvalues. For supersonic flow, $F^+ = F$ and $F^- = 0$ if $M \geq 1$. Likewise, $F^- = F$ and $F^+ = 0$ if $M \leq -1$. For subsonic flow, $|M| < 1$, both F^+ and F^- make a contribution to the total flux. The corresponding numerical flux formula is

$$F(Q_L, Q_R) = F^+(Q_L) + F^-(Q_R)$$

Since the Van Leer FVS scheme has continuously differentiable flux contributions and smoother solutions near sonic and stagnation points than the Steger-Warming FVS scheme (Ref.16,52) only the Van Leer FVS scheme is considered.

From Eq.(13) and Eq.(16), the flux F can be written as

$$F(\rho, \tilde{a}, \tilde{M}) = \begin{bmatrix} \rho\tilde{a}\tilde{M} \\ \rho\tilde{a}^2(\tilde{M}^2 + \frac{1}{\tilde{\gamma}}) \\ \rho\tilde{a}^3\tilde{M}(\frac{\tilde{M}^2}{2} + \frac{1}{\tilde{\gamma}-1}) \end{bmatrix} \tag{20}$$

where $\tilde{a}$ and $\tilde{M}$ are the "equivalent speed of sound" and "equivalent Mach number", respectively, given by

$$\tilde{a}^2 = \tilde{\gamma}\frac{p}{\rho} \qquad \tilde{M} = \frac{u}{\tilde{a}}$$

The flux F given by Eq.(20) can be split following the procedures of Ref.13 as

$$F^{\pm} = \begin{bmatrix} f_1^{\pm} \\ f_2^{\pm} \\ f_3^{\pm} \end{bmatrix} = \begin{bmatrix} \pm\rho\tilde{a}(\tilde{M} \pm 1)^2/4 \\ f_1^{\pm}[(\tilde{\gamma}-1)u \pm 2\tilde{a}]/\tilde{\gamma} \\ f_1^{\pm}[(\tilde{\gamma}-1)u \pm 2\tilde{a}]^2/2(\tilde{\gamma}^2-1) \end{bmatrix} \tag{21}$$

Here, this flux splitting is based on $\tilde{A}$ and the "equivalent" $\tilde{a}$ instead of A and the true speed of sound a given by Eq.(17).

Comparing the split flux vector of Eq.(21) with the one given in Ref.13 for a perfect gas, it can be realized that M, a and γ for a perfect gas are replaced by $\tilde{M}$, $\tilde{a}$ and $\tilde{\gamma}$ for a real gas. This is natural since the 'real' gas equation of state, Eq.(16), has the same functional form as the perfect gas case. Noting the above results, $\hat{F}^{\pm}$ for a perfect gas in a 3-D general coodinate system which are given in Ref.13 can be easily modified for a real gas by using the "equivalent" terms. So finally, for subsonic flow ($|\bar{u}| < \tilde{a}$) , the Van Leer splitting of $\hat{F}$ for a real gas is given by

$$\hat{F}^{\pm} = \frac{|\nabla\xi|}{J} \begin{bmatrix} f_1^{\pm} \\ f_1^{\pm}[\hat{\xi}_x(-\bar{u} \pm 2\tilde{a})/\tilde{\gamma} + u] \\ f_1^{\pm}[\hat{\xi}_y(-\bar{u} \pm 2\tilde{a})/\tilde{\gamma} + v] \\ f_1^{\pm}[\hat{\xi}_z(-\bar{u} \pm 2\tilde{a})/\tilde{\gamma} + w] \\ f_5^{\pm} \end{bmatrix} \tag{22}$$

where

$$f_1^{\pm} = \pm \frac{\rho\tilde{a}}{4}(\tilde{M} \pm 1)^2$$

$$f_5^{\pm} = f_1^{\pm}\{[\frac{-(\tilde{\gamma}-1)\bar{u}^2 \pm 2(\tilde{\gamma}-1)\bar{u}\tilde{a} + 2\tilde{a}^2}{\tilde{\gamma}^2 - 1}] + \frac{q^2}{2}\}$$

$$\tilde{M} = \bar{u}/\tilde{a}$$

$$(\hat{\xi}_x, \hat{\xi}_y, \hat{\xi}_z) = \frac{(\xi_x, \xi_y, \xi_z)}{|\nabla\xi|}$$

$$\bar{u} = \hat{\xi}_x u + \hat{\xi}_y v + \hat{\xi}_z w$$

The other split fluxes, $\hat{G}^{\pm}$ and $\hat{H}^{\pm}$ follow similarly.

4.3 Roe's Flux Difference Splitting

The Roe's Flux Difference Splitting (FDS) scheme is based on an approximate Riemann problem (Ref.12,20)

$$\frac{\partial Q}{\partial t} + \tilde{A}\frac{\partial Q}{\partial x} = 0 \tag{23}$$

where $\tilde{A}$ is a locally constant matrix for each pair of initial data (Q_L, Q_R). The requirements for $\tilde{A}$ are given in Ref.12 as

(i) $\tilde{A}(Q, Q) = A(Q)$

(ii) $\tilde{A}(Q_L, Q_R)$ has a complete set of real eigenvalues and eigenvectors.

(iii) $\tilde{A}(Q_L, Q_R)\bullet(Q_R - Q_L) = F(Q_R) - F(Q_L)$

The procedure for generating $\tilde{A}$ is given in Ref.12 for a perfect gas in terms of parameter vectors. In this section, following the approach of Grossman and Walters (Ref.21-22), the Roe scheme for a real gas in a 3-D general coordinate system is derived.

In the Roe scheme, the flux at an $\xi = constant$ cell face is given by

$$\begin{aligned} \hat{F}_{i+\frac{1}{2}} &= \frac{1}{2}(\hat{F}_R + \hat{F}_L - |\tilde{A}|(Q_R - Q_L)) \\ &= \frac{1}{2}(\hat{F}_R + \hat{F}_L - S|\Lambda|S^{-1}\Delta Q) \end{aligned} \tag{24}$$

where Λ is a diagonal matrix whose elements are composed of the eigenvalues of $\tilde{A}$ and the columns of the matrix S consist of the right eigenvectors of $\tilde{A}$. To

determine the matrix $\tilde{A}$, consider a local coordinate system (ξ^*, η^*, ζ^*) on a $\xi = constant$ cell face such that $\xi^* = \xi$ and η^* and ζ^* are both orthogonal to ξ^* In the following equations, the superscript * means the values in the local coordinate system. Using the transformation matrix which is defined as

$$T = \begin{bmatrix} 1 & 0 & 0 & 0 & 0 \\ 0 & \hat{\xi}_x^* & \hat{\xi}_y^* & \hat{\xi}_z^* & 0 \\ 0 & \hat{\eta}_x^* & \hat{\eta}_y^* & \hat{\eta}_z^* & 0 \\ 0 & \hat{\zeta}_x^* & \hat{\zeta}_y^* & \hat{\zeta}_z^* & 0 \\ 0 & 0 & 0 & 0 & 1 \end{bmatrix} \tag{25}$$

the flux $\hat{F}$ given in Eq.(6) is transformed to

$$\hat{F}^* = T\hat{F} = \frac{|\nabla\xi|}{J} \begin{bmatrix} \rho u^* \\ \rho u^{*2} + p \\ \rho u^* v^* \\ \rho u^* w^* \\ u^*(\rho e_0 + p) \end{bmatrix} \qquad Q^* = TQ = \begin{bmatrix} \rho \\ \rho u^* \\ \rho v^* \\ \rho w^* \\ \rho e_0 \end{bmatrix} \tag{26}$$

where, u^*, v^* and w^* are the contravariant velocity componets in the ξ^*, η^*, ζ^* directions.

Introducing the parameter vector which is given in Ref.12 as

$$\overline{w} = \sqrt{\rho}\begin{bmatrix} 1 \\ u^* \\ v^* \\ w^* \\ h_0 \end{bmatrix} = \begin{bmatrix} w_1 \\ w_2 \\ w_3 \\ w_4 \\ w_5 \end{bmatrix} \tag{27}$$

where $h_0 = e_0 + p/\rho$, the Q^* and the flux F^* in a local coordinate system can be expressed as

$$Q^* = \begin{bmatrix} w_1^2 \\ w_1 w_2 \\ w_1 w_3 \\ w_1 w_4 \\ w_1 w_5 - p \end{bmatrix} \qquad F^* = \frac{|\nabla \xi|}{J}\begin{bmatrix} w_1 w_2 \\ w_2^2 + p \\ w_2 w_3 \\ w_2 w_4 \\ w_2 w_5 \end{bmatrix} \tag{28}$$

Using Eq.(16), the pressure is written in terms of parameter variables and "equivalent" $\tilde{\gamma}$

$$\begin{aligned} p &= \frac{\tilde{\gamma} - 1}{\tilde{\gamma}}\left(\rho h_0 - \frac{\rho q^2}{2}\right) \\ &= \frac{\tilde{\gamma} - 1}{\tilde{\gamma}}\left(w_1 w_5 - \frac{w_2^2 + w_3^2 + w_4^2}{2}\right) \end{aligned} \tag{29}$$

Since ΔQ^* and ΔF^* can be written as

$$\begin{aligned} \Delta Q^* &= \tilde{B}^* \Delta \overline{w} \\ \Delta F^* &= \frac{|\nabla \xi|}{J} \tilde{C}^* \Delta \overline{w} \end{aligned} \tag{30}$$

the matrix $\tilde{A}^*$ where $\Delta F^* = \frac{|\nabla\xi|}{J}\tilde{A}^*\Delta Q^*$ is given by

$$\tilde{A}^* = \tilde{C}^*\tilde{B}^{*-1} \tag{31}$$

Here, $\Delta\overline{w}$ terms represent the jumps of variables at a cell interface, $(\overline{w}_R - \overline{w}_L)$. In order to find $\tilde{B}^*$ and $\tilde{C}^*$, Δp is needed from Eq.(28), which is given as

$$\begin{aligned}\Delta p = & <(\frac{\tilde{\gamma}-1}{\tilde{\gamma}})>\Delta(w_1w_5 - \frac{w_2^2+w_3^2+w_4^2}{2}) \\ & + <w_1w_5 - \frac{w_2^2+w_3^2+w_4^2}{2}>\Delta(\frac{\tilde{\gamma}-1}{\tilde{\gamma}})\end{aligned} \tag{32}$$

where

$$\begin{aligned}\Delta(w_1w_5 - \frac{w_2^2+w_3^2+w_4^2}{2}) = & <w_1>\Delta w_5 + <w_5>\Delta w_1 \\ & - <w_2>\Delta w_2 - <w_3>\Delta w_3 - <w_4>\Delta w_4\end{aligned}$$

Here $<\overline{w}>$ terms represent the arithmetic mean value, $\frac{1}{2}(\overline{w}_R + \overline{w}_L)$. Realizing that $\tilde{\gamma}$ is constrained to be $1 < \tilde{\gamma} \leq \frac{5}{3}$, $\Delta\tilde{\gamma}$ can be assumed to be relatively small to the other flow quantities across a cell face (Ref.21). Under this assumption, the average terms and the jump term of Eq.(32) can be written in the Taylor expansion form as

$$\begin{aligned}<\frac{\tilde{\gamma}-1}{\tilde{\gamma}}> &= \frac{<\tilde{\gamma}>-1}{<\tilde{\gamma}>} + O(\Delta\tilde{\gamma})^2 \\ \Delta(\frac{\tilde{\gamma}-1}{\tilde{\gamma}}) &= \frac{\Delta<\tilde{\gamma}>}{<\tilde{\gamma}>^2} + O(\Delta\tilde{\gamma})^3\end{aligned}$$

and

$$< w_1 w_5 - \frac{w_2^2 + w_3^2 + w_4^2}{2} > = \frac{< \tilde{\gamma} > < p >}{< \tilde{\gamma} >^2 - 1} + \frac{1}{4} \frac{\Delta p \, \Delta \tilde{\gamma}}{(< \gamma > - 1)^2} + H.O.T$$

Thus the Δp can be expressed as

$$\begin{aligned} \Delta p = & \left(\frac{< \tilde{\gamma} > - 1}{< \tilde{\gamma} >} \right) \Delta \left(w_5 w_1 - \frac{w_2^2 + w_{32} + w_4^2}{2} \right) \\ & + \frac{< p > \Delta \tilde{\gamma}}{< \tilde{\gamma} > (< \tilde{\gamma} > - 1)} + O(\Delta \tilde{\gamma})^2 \end{aligned} \tag{33}$$

In order to complete the Eq.(33), the $\Delta \tilde{\gamma}$ term is approximated by following the approach of Colella and Glaz (Ref.23) which is valid only for an isentropic flow. From Eq.(16), the derivative of $\tilde{\gamma}$ is given as

$$d\tilde{\gamma} = \frac{1}{\rho e} dp - \frac{p}{\rho^2 e} d\rho - \frac{p}{\rho e^2} de$$

Since for an isentropic flow, $de = \frac{p}{\rho^2} d\rho$ from the first law of thermodynamics and $a^2 = \frac{dp}{d\rho}$ from the definition, the above equation can be rewritten as

$$d\tilde{\gamma} = (\tilde{\gamma} - 1)\left(1 - \frac{\tilde{\gamma} p}{\rho a^2}\right) \frac{dp}{p}$$

And using Eq.(17),

$$d\tilde{\gamma} = (\tilde{\gamma} - 1)\left[1 - \frac{\tilde{\gamma}}{\Gamma}\right] \frac{dp}{p}$$

Since the jumps in $\tilde{\gamma}$ and Γ are assumed to be very small, $\Delta\tilde{\gamma}$ can be finally approximated from the above equation as

$$\Delta\tilde{\gamma} = (<\tilde{\gamma}> - 1)[1 - \frac{<\tilde{\gamma}>}{<\tilde{\Gamma}>}]\frac{\Delta p}{<p>} \tag{34}$$

Using Eq.(34), Eq.(33) is written as

$$\Delta p[1 - (1 - \frac{<\tilde{\gamma}>}{<\Gamma>})\frac{1}{<\tilde{\gamma}>}] = \frac{<\tilde{\gamma}> - 1}{<\tilde{\gamma}>}\,\Delta(w_1 w_5 - \frac{w_2^2 + w_3^2 + w_4^2}{2})$$

Further assuming that $<\tilde{\gamma}>$ is nearly equal to $<\Gamma>$ (Ref.21),i.e.

$$\varepsilon = (\frac{<\tilde{\gamma}>}{<\Gamma>} - 1)\frac{1}{<\tilde{\gamma}>} << 1 \tag{35}$$

Δp is obtained in terms of parameter variables as

$$\Delta p = \frac{<\tilde{\gamma}> - 1}{<\tilde{\gamma}>}(1 - \varepsilon)\,\Delta(w_1 w_5 - \frac{w_2^2 + w_3^2 + w_4^2}{2}) \tag{36}$$

where

$$\Delta(w_1 w_5 - \frac{w_2^2 + w_3^2 + w_4^2}{2}) = <w_1>\Delta w_5 + <w_5>\Delta w_1 - <w_2>\Delta w_2 - <w_3>\Delta w_3 - <w_4>\Delta w_4$$

Using Eq.(25) and Eq.(33), $\tilde{B}^*$ and $\tilde{C}^*$, which are defined in Eq.(27), can be obtained as

$$\tilde{B}^* = \begin{bmatrix} 2<w_1> & 0 & 0 & 0 & 0 \\ <w_2> & <w_1> & 0 & 0 & 0 \\ <w_3> & 0 & <w_1> & 0 & 0 \\ <w_4> & 0 & 0 & <w_1> & 0 \\ b_{51} & b_{52} & b_{53} & b_{54} & b_{55} \end{bmatrix} \tag{37}$$

where

$$b_{51} = \frac{1+\varepsilon(<\tilde{\gamma}>-1)}{<\tilde{\gamma}>}<w_5> \qquad b_{52} = \frac{<\tilde{\gamma}>-1}{<\tilde{\gamma}>}(1-\varepsilon)<w_2>$$

$$b_{53} = \frac{<\tilde{\gamma}>-1}{<\tilde{\gamma}>}(1-\varepsilon)<w_3> \qquad b_{54} = \frac{<\tilde{\gamma}>-1}{<\tilde{\gamma}>}(1-\varepsilon)<w_4>$$

$$b_{55} = \frac{1+\varepsilon(<\tilde{\gamma}>-1)}{<\tilde{\gamma}>}<w_1>$$

and

$$\tilde{C}^* = \begin{bmatrix} <w_2> & <w_1> & 0 & 0 & 0 \\ c_{21} & c_{22} & c_{23} & c_{24} & c_{25} \\ 0 & <w_3> & <w_2> & 0 & 0 \\ 0 & <w_4> & 0 & <w_2> & 0 \\ 0 & <w_5> & 0 & 0 & <w_2> \end{bmatrix} \tag{38}$$

where

$$c_{21} = \frac{<\tilde{\gamma}> - 1}{<\tilde{\gamma}>}(1-\varepsilon)<w_5> \qquad c_{22} = \frac{<\tilde{\gamma}> + 1 + \varepsilon(<\tilde{\gamma}> - 1)}{<\tilde{\gamma}>}<w_2>$$

$$c_{23} = -\frac{<\tilde{\gamma}> - 1}{<\tilde{\gamma}>}(1-\varepsilon)<w_3> \qquad c_{24} = -\frac{<\tilde{\gamma}> - 1}{<\tilde{\gamma}>}(1-\varepsilon)<w_4>$$

$$c_{25} = \frac{<\tilde{\gamma}> - 1}{<\tilde{\gamma}>}<w_1>$$

Utilizing Eq.(35), Eq.(37), and Eq.(38) and introducing the Roe's averages which are defined as

$$\begin{aligned}
\tilde{u}^* &= \frac{<w_2>}{<w_1>} = \frac{<\sqrt{\rho}\,u^*>}{<\sqrt{\rho}>} \\
\tilde{v}^* &= \frac{<w_3>}{<w_1>} = \frac{<\sqrt{\rho}\,v^*>}{<\sqrt{\rho}>} \\
\tilde{w}^* &= \frac{<w_4>}{<w_1>} = \frac{<\sqrt{\rho}\,w^*>}{<\sqrt{\rho}>} \\
\tilde{h}_0 &= \frac{<w_5>}{<w_1>} = \frac{<\sqrt{\rho}\,h_0>}{<\sqrt{\rho}>}
\end{aligned} \tag{39}$$

the matrix $\tilde{A}^* = \tilde{C}^* \tilde{B}^{*-1}$ can be determined as

$$\tilde{A}^* = \begin{bmatrix}
0 & 1 & 1 & 0 & 0 \\
a_{21} & (3-\alpha)\tilde{u}^* & -(\alpha-1)\tilde{v}^* & -(\alpha-1)\tilde{w}^* & (\alpha-1) \\
-\tilde{u}^*\tilde{v}^* & \tilde{u}^* & \tilde{u}^* & 0 & 0 \\
-\tilde{u}^*\tilde{w}^* & \tilde{w}^* & 0 & \tilde{u}^* & 0 \\
a_{51} & a_{52} & -(\alpha-1)\tilde{u}^*\tilde{v}^* & -(\alpha-1)\tilde{u}^*\tilde{w}^* & \alpha\tilde{u}^*
\end{bmatrix} \tag{40}$$

where

$$
\begin{aligned}
a_{21} &= -\tilde{u}^{*2} + \frac{(\alpha-1)\tilde{q}^2}{2} \\
a_{51} &= -\tilde{u}^{*}\tilde{h}_0 + \frac{(\alpha-1)\tilde{u}^{*}\tilde{q}^2}{2} \\
a_{52} &= \tilde{h}_0 - (\alpha-1)\tilde{u}^{*2} \\
\alpha &= \frac{<\tilde{\gamma}>}{1+\varepsilon(<\tilde{\gamma}>-1)} \\
q^2 &= \tilde{u}^{*2} + \tilde{v}^{*2} + \tilde{w}^{*2}
\end{aligned}
$$

The eigenvalues and eigenvectors of $\tilde{A}^*$ are obtained as

$$
\begin{aligned}
\lambda_1^* &= \lambda_2^* = \lambda_3^* = \tilde{u}^* \\
\lambda_4^* &= \tilde{u}^* + \tilde{a} \\
\lambda_5^* &= \tilde{u}^* - \tilde{a}
\end{aligned}
\tag{41}
$$

and

$$
\hat{e}_1^* = \begin{bmatrix} 1 \\ \tilde{u}^* \\ \tilde{v}^* \\ \tilde{w}^* \\ q^2/2 \end{bmatrix} \qquad \hat{e}_2^* = \begin{bmatrix} 0 \\ 0 \\ 1 \\ 0 \\ \tilde{v}^* \end{bmatrix} \qquad \hat{e}_3^* = \begin{bmatrix} 0 \\ 0 \\ 0 \\ 1 \\ \tilde{w}^* \end{bmatrix}
$$

$$
\hat{e}_4^* = \begin{bmatrix} 1 \\ \tilde{u}^* + \tilde{a} \\ \tilde{v}^* \\ \tilde{w}^* \\ \tilde{h}_0 + \tilde{a}\tilde{u}^* \end{bmatrix} \qquad \hat{e}_5^* = \begin{bmatrix} 1 \\ \tilde{u}^* - \tilde{a} \\ \tilde{v}^* \\ \tilde{w}^* \\ \tilde{h}_0 - \tilde{a}\tilde{u}^* \end{bmatrix} \tag{42}
$$

where

$$\tilde{a}^2 = \frac{(<\tilde{\gamma}> - 1)(1-\varepsilon)}{1+\varepsilon(<\tilde{\gamma}> - 1)} (\tilde{h}_0 - \frac{\tilde{u}^{*2} + \tilde{v}^{*2} + \tilde{w}^{*2}}{2}) \tag{43}$$

Under the assumption of Eq.(35), Eq.(43) is reduced to the true speed of sound given in Eq.(17).

$$\tilde{a}^2 = \frac{(<\tilde{\gamma}> - 1)<\Gamma>}{<\tilde{\gamma}>} (\tilde{h}_0 - \frac{\tilde{u}^{*2} + \tilde{v}^{*2} + \tilde{w}^{*2}}{2}) \tag{44}$$

From the above equations, it can be seen that for a perect gas case where $<\tilde{\gamma}> = <\Gamma> = \gamma$, the original formulation of Roe (Ref.12) is obtained.

Hence, using the above results, Eq.(24) can be written in terms of the local coordinate values as

$$\begin{aligned} \hat{F}_{i+\frac{1}{2}} &= \frac{1}{2}(\hat{F}_R + \hat{F}_L - |\tilde{A}|\Delta Q) \\ &= \frac{1}{2}(\hat{F}_R + \hat{F}_L - S|\Lambda|S^{-1}\Delta Q) \\ &= \frac{1}{2}(\hat{F}_R + \hat{F}_L - \sum_i |\Delta \hat{F}_i|) \end{aligned} \tag{45}$$

where

$$|\tilde{A}| = \frac{|\nabla\xi|}{J} |T^{-1}\tilde{A}^* T|$$

$$\Lambda = \frac{|\nabla\xi|}{J} |\Lambda^*|$$

$$S = T^{-1}S^*$$

Even though the flux differences in Eq.(45), $\Delta\hat{F}_i$, are derived in terms of the jumps in the conservative variables, $\Delta\hat{F}_i$ can be expressed in terms of the jumps in the primitive variables, (ρ, u, v, w, p), to get the more compact forms.

Thus, the flux difference associated with the repeated eigenvalue, λ_1 , is given by

$$|\Delta\hat{F}_1| = |\lambda_1|\left\{(\Delta\rho - \frac{\Delta p}{\tilde{a}^2})\begin{bmatrix} 1 \\ \tilde{u} \\ \tilde{v} \\ \tilde{w} \\ \frac{q^2}{2} \end{bmatrix} + \tilde{\rho}\begin{bmatrix} 0 \\ \Delta u - \hat{\xi}_x\Delta\bar{u} \\ \Delta v - \hat{\xi}_y\Delta\bar{u} \\ \Delta w - \hat{\xi}_z\Delta\bar{u} \\ \Delta(\frac{q^2}{2}) - \tilde{\bar{u}}\Delta\bar{u} \end{bmatrix}\right\} \tag{46}$$

and the flux differences associated with the λ_4 and λ_5 eigenvalues are given by

$$|\Delta\hat{F}_{4,5}| = |\lambda_{4,5}|\,\frac{(\Delta p \pm \tilde{\rho}\tilde{a}\Delta\bar{u})}{\tilde{a}^2}\begin{bmatrix} 1 \\ \tilde{u} \pm \tilde{a}\hat{\xi}_x \\ \tilde{v} \pm \tilde{a}\hat{\xi}_y \\ \tilde{w} \pm \tilde{a}\hat{\xi}_z \\ \tilde{h}_0 \pm \tilde{a}\tilde{\bar{u}} \end{bmatrix} \tag{47}$$

where

$$
\begin{aligned}
\lambda_1 &= \frac{|\nabla\xi|}{J}\tilde{\bar{u}} \\
\lambda_4 &= \frac{|\nabla\xi|}{J}(\tilde{\bar{u}} + \tilde{a}) \\
\lambda_5 &= \frac{|\nabla\xi|}{J}(\tilde{\bar{u}} - \tilde{a}) \\
\tilde{\bar{u}} &= \hat{\xi}_x\tilde{u} + \hat{\xi}_y\tilde{v} + \hat{\xi}_z\tilde{w}
\end{aligned}
\tag{48}
$$

Note that in Eq.(46) and Eq.(47), Roe averaged evaluations of Eq.(39) are implied for all terms. In particular the speed of sound averaging, defined in Eq.(44) must be used for a real gas.

The flux differences in the other two directions are given in the similar ways because the derivation procedure is based on a local coordinate system at a cell face.

4.4 Spatial Accuracy

The state variable at the cell face is constructed from non-oscillatory interpolation of the primitive variables $Q^p = [\rho, u, v, w, p, \tilde{\gamma}]^T$. First order accurate differencing corresponds to

$$
\begin{aligned}
(Q^p_L)_{i+\frac{1}{2}} &= Q^p_i \\
(Q^p_R)_{i+\frac{1}{2}} &= Q^p_{i+1}
\end{aligned}
$$

Higher order accurate differencing is given by

$$
\begin{aligned}
(Q_L^p)_{i+\frac{1}{2}} &= Q_i^p + \frac{1}{4}[(1-\kappa)\overline{\nabla} + (1+\kappa)\overline{\Delta}]Q_i^p \\
(Q_R^p)_{i+\frac{1}{2}} &= Q_{i+1}^p - \frac{1}{4}[(1+\kappa)\overline{\nabla} + (1+\kappa)\overline{\Delta}]Q_{i+1}^p
\end{aligned}
\tag{49}
$$

where the operator ∇ and Δ represent backward and forward differences. The bars over the differences in Eq.(49) serve to limit the higher-order correction in regions of strong gradients, thereby providing smooth profiles at the expense of a local decrease in accuracy. Here the so-called min-mod limiter (Ref.52) is chosen, which is given by

$$
\begin{aligned}
\overline{\nabla}Q &= \mathit{minmod}(\nabla Q, \beta\Delta Q) \\
\overline{\Delta}Q &= \mathit{minmod}(\Delta Q, \beta\nabla Q)
\end{aligned}
\tag{50}
$$

where

$$
\mathit{minmod}\,(x,y) = \mathit{sgn}(x)\max[0, \min(x\,\mathit{sgn}(y), y\,\mathit{sgn}(x))]
$$

and $\beta = (3-\kappa)/(1-\kappa)$. Without using the limiter, Eq.(49) yields a one-parameter family of second-order accurate difference schemes. One member, corresponding to $\kappa = 1/3$, is third-order accurate.

4.5 Extension to Viscous Flows

The viscous terms in the thin-layer Navier-Stokes equations have only ζ direction components, which are given in Eq.(6) in the finite volume formulation as

$$\hat{H}_v = \frac{M_\infty}{Re_L} \mu J \left(\frac{|\nabla\zeta|}{J}\right)^2 \hat{T}_\zeta \tag{51}$$

where

$$\hat{T} = \begin{bmatrix} 0 \\ (1 + \hat{\zeta}_x^2/3)u + (\hat{\zeta}_y v + \hat{\zeta}_z w)\hat{\zeta}_x/3 \\ (1 + \hat{\zeta}_y^2/3)v + (\hat{\zeta}_x u + \hat{\zeta}_z w)\hat{\zeta}_y/3 \\ (1 + \hat{\zeta}_z^2/3)w + (\hat{\zeta}_x u + \hat{\zeta}_y v)\hat{\zeta}_z/3 \\ \frac{1}{2}[(1 + \hat{\zeta}_x^2/3)u^2 + (1 + \hat{\zeta}_y^2/3)v^2 + (1 + \hat{\zeta}_z^2/3)w^2] \\ + \frac{1}{3}[\hat{\zeta}_x\hat{\zeta}_y uv + \hat{\zeta}_x\hat{\zeta}_z uw + \hat{\zeta}_y\hat{\zeta}_z vw] + \alpha \end{bmatrix}$$

and α_ζ is given in Eq.(6).

The viscous terms are discretized by central differencing as

$$\begin{aligned} \left(\frac{\partial \hat{H}_v}{\partial \zeta}\right)_k &= (\hat{H}_v)_{k+\frac{1}{2}} - (\hat{H}_v)_{k-\frac{1}{2}} \\ &= \frac{M_\infty}{Re_L}\{[\mu J\left(\frac{|\nabla\zeta|}{J}\right)^2]_{k+\frac{1}{2}}(\hat{T}_{k+1} - \hat{T}_k) - [\mu J\left(\frac{|\nabla\zeta|}{J}\right)^2]_{k-\frac{1}{2}}(\hat{T}_k - \hat{T}_{k-1})\} \end{aligned} \tag{52}$$

Here, the cell volume term is required at the cell interface and is determined by the average of neighboring volumes.

5. Implicit Algorithm

5.1 Euler Implicit Time Integration

To complete the discretization of the governing equations, Euler implicit time integration scheme is used. Even though it has only first order accuracy in time, it shows a fast convergence rate to steady state solutions.

The Euler implicit time discretization of Eq.(4) is given by

$$V \frac{\Delta Q^n}{\Delta t} = - R(Q^{n+1}) \tag{53}$$

where $R(Q^{n+1})$ is the steady state residual evaluated at time level $n + 1$ and should be zero at steady state. The steady state residual is given from Eq.(6) by

$$R(Q^{n+1}) = \hat{F}^{n+1}_{i+\frac{1}{2}} - \hat{F}^{n+1}_{i-\frac{1}{2}} + \hat{G}^{n+1}_{j+\frac{1}{2}} - \hat{G}^{n+1}_{j-\frac{1}{2}} + (\hat{H}^{n+1} - \hat{H}^{n+1}_{v})_{k+\frac{1}{2}} - (\hat{H}^{n+1} - \hat{H}^{n+1}_{v})_{k-\frac{1}{2}} \tag{54}$$

Eq.(53) is linearized by using a Taylor expansion about time level n to give

$$[\frac{V}{\Delta t} I + \frac{\partial R}{\partial Q}]^n \Delta Q^n = -R(Q^n) \tag{55}$$

where

$$\Delta Q^n = Q^{n+1} - Q^n$$

$$\frac{\partial R}{\partial Q} = (\frac{\partial \hat{F}}{\partial Q})_{i+\frac{1}{2}} - (\frac{\partial \hat{F}}{\partial Q})_{i-\frac{1}{2}} + (\frac{\partial \hat{G}}{\partial Q})_{j+\frac{1}{2}} - (\frac{\partial \hat{G}}{\partial Q})_{j-\frac{1}{2}} + (\frac{\partial \hat{H}}{\partial Q} - \frac{\partial \hat{H}_v}{\partial Q})_{k+\frac{1}{2}} - (\frac{\partial \hat{H}}{\partial Q} - \frac{\partial \hat{H}_v}{\partial Q})_{k-\frac{1}{2}}$$

and I is an identity matrix.

Since Eq.(55) represents a large banded, 5 x 5 block matrix equation, the spatial discretization of the inviscid Jacobians of Eq.(55), is always taken as first order accurate to reduce the bandwidth of the matrix and computational effort. This does not affect the spatial accuracy of steady state solutions because it is determined only by the spatial differencing of $R(Q)$.

5.2 Evaluation of the Jacobians for a Real Gas.

The exact Jacobians of the inviscid flux vectors for a real gas require derivatives of $\tilde{\gamma}$ but it is impractical and not necessary to evaluate them. Hence, following the approach of Grossman and Walters (Ref.21-22), those terms are ignored to obtain the approximate Jacobians. Because this assumption is applied only to the implicit part of Eq.(55), it does not affect the steady state solutions. Also for $\tilde{\gamma} = \Gamma = \gamma$, the approximate Jacobians have the same functional form as the perfect gas case.

5.2.1 Inviscid Jacobians of Van Leer's FVS

In the Van Leer's FVS, the residual is given by

$$\begin{aligned} R(Q) = {} & \hat{F}^{+}(Q_L)_{i+\frac{1}{2}} + \hat{F}^{-}(Q_R)_{i+\frac{1}{2}} - \hat{F}^{+}(Q_L)_{i-\frac{1}{2}} - \hat{F}^{-}(Q_R)_{i-\frac{1}{2}} \\ & + \hat{G}^{+}(Q_L)_{j+\frac{1}{2}} + \hat{G}^{-}(Q_R)_{j+\frac{1}{2}} - \hat{G}^{+}(Q_L)_{j-\frac{1}{2}} - \hat{G}^{-}(Q_R)_{j-\frac{1}{2}} \\ & + \hat{H}^{+}(Q_L)_{k+\frac{1}{2}} + \hat{H}^{-}(Q_R)_{k+\frac{1}{2}} - \hat{H}^{+}(Q_L)_{k-\frac{1}{2}} - \hat{H}^{-}(Q_R)_{k-\frac{1}{2}} \\ & (\hat{H}_v)_{k+\frac{1}{2}} - (\hat{H}_v)_{k-\frac{1}{2}} \end{aligned} \tag{56}$$

where the flux vectors are given by Eq.(22). Combing Eq.(56) and Eq.(55) with the first order accuracy in the implicit terms yields

$$
\begin{aligned}
&\left(\frac{V}{\Delta t} I + B_\xi + B_\eta + B_\zeta\right)\Delta Q^n + A_\xi \Delta Q^n_{i-1} + C_\xi \Delta Q^n_{i+1} \\
&\quad + A_\eta \Delta Q^n_{j-1} + C_\eta \Delta Q^n_{j+1} + A_\zeta \Delta Q^n_{k-1} + C_\zeta \Delta Q^n_{k+1} \\
&\quad + \left(\frac{\partial \hat{H}_v}{\partial Q}\right)_{k+\frac{1}{2}} - \left(\frac{\partial \hat{H}_v}{\partial Q}\right)_{k-\frac{1}{2}} = -R(Q^n)
\end{aligned}
\tag{57}
$$

where

$$
\begin{aligned}
A_\xi &= -\left(\frac{\partial \hat{F}^+}{\partial Q}\right)_{i-\frac{1}{2}} \\
B_\xi &= \left(\frac{\partial \hat{F}^+}{\partial Q}\right)_{i+\frac{1}{2}} - \left(\frac{\partial \hat{F}^-}{\partial Q}\right)_{i-\frac{1}{2}} \\
C_\xi &= \left(\frac{\partial \hat{F}^-}{\partial Q}\right)_{i+\frac{1}{2}}
\end{aligned}
$$

and for η and ζ, $\hat{F}$ and i are replaced by $\hat{G}$, j and $\hat{H}$, k, respectively.

5.2.2 Inviscid Jacobians of Roe's FDS

In the Roe's FDS, the residual is given by

$$
\begin{aligned}
R(Q) = & \frac{1}{2}[\hat{F}(Q_R)_{i+\frac{1}{2}} + \hat{F}(Q_L)_{i+\frac{1}{2}} - |\tilde{A}|(Q_R - Q_L)_{i+\frac{1}{2}}] \\
& - \frac{1}{2}[\hat{F}(Q_R)_{i-\frac{1}{2}} + \hat{F}(Q_L)_{i-\frac{1}{2}} - |\tilde{A}|(Q_R - Q_L)_{i-\frac{1}{2}}] \\
& + \frac{1}{2}[\hat{G}(Q_R)_{j+\frac{1}{2}} + \hat{G}(Q_L)_{j+\frac{1}{2}} - |\tilde{A}|(Q_R - Q_L)_{j+\frac{1}{2}}] \\
& + \frac{1}{2}[\hat{G}(Q_R)_{j-\frac{1}{2}} + \hat{G}(Q_L)_{j-\frac{1}{2}} - |\tilde{A}|(Q_R - Q_L)_{j-\frac{1}{2}}] \\
& + \frac{1}{2}[\hat{H}(Q_R)_{k+\frac{1}{2}} + \hat{H}(Q_L)_{k+\frac{1}{2}} - |\tilde{A}|(Q_R - Q_L)_{k+\frac{1}{2}}] \\
& + \frac{1}{2}[\hat{H}(Q_R)_{k-\frac{1}{2}} + \hat{H}(Q_L)_{k-\frac{1}{2}} - |\tilde{A}|(Q_R - Q_L)_{k-\frac{1}{2}}] \\
& + (\hat{H}_v)_{k+\frac{1}{2}} - (\hat{H}_v)_{k-\frac{1}{2}}
\end{aligned}
\tag{58}
$$

As seen above, the linearization of Eq.(58) includes the linearization of $|\tilde{A}|$ terms. Since the term $\frac{\partial|\tilde{A}|}{\partial Q}$ is difficult to obtain and impractical for numerical implementation, $\frac{\partial|\tilde{A}|}{\partial Q}$ terms are neglected in the implicit part. This approximation was found to be extremely reliable by Barth (Ref.53). Using Eq.(58), Eq.(55) with the first order accuracy in the implicit terms gives

$$
\begin{aligned}
& (\frac{V}{\Delta t} I + B_\xi + B_\eta + B_\zeta)\Delta Q^n + A_\xi \Delta Q^n_{i-1} + C_\xi \Delta Q^n_{i+1} \\
& \quad + A_\eta \Delta Q^n_{j-1} + C_\eta \Delta Q^n_{j+1} + A_\zeta \Delta Q^n_{k-1} + C_\zeta \Delta Q^n_{k+1} \\
& \quad + (\frac{\partial \hat{H}_v}{\partial Q})_{k+\frac{1}{2}} - (\frac{\partial \hat{H}_v}{\partial Q})_{k-\frac{1}{2}} = -R(Q^n)
\end{aligned}
\tag{59}
$$

where

$$A_\xi = -\frac{1}{2}[(\frac{\partial \hat{F}_L}{\partial Q})_{i-\frac{1}{2}} - |\tilde{A}|_{i-\frac{1}{2}}]$$

$$B_\xi = \frac{1}{2}[(\frac{\partial \hat{F}^+}{\partial Q})_{i+\frac{1}{2}} - |\tilde{A}|_{i+\frac{1}{2}} - (\frac{\partial \hat{F}^-}{\partial Q})_{i-\frac{1}{2}} + |\tilde{A}|_{i-\frac{1}{2}}]$$

$$C_\xi = \frac{1}{2}[(\frac{\partial \hat{F}^-}{\partial Q})_{i+\frac{1}{2}} - |\tilde{A}|_{i+\frac{1}{2}}]$$

and for η and ζ, $\hat{F}$ and i are replaced by $\hat{G}$, j and $\hat{H}$, k, respectively.

5.2.3 Viscous Jacobian terms

From Eq.(51) and (52), the linearization of the viscous flux term is given by

$$\begin{aligned}\frac{\partial}{\partial \zeta}(\frac{\partial \hat{H}_v}{\partial Q})_k &= (\frac{\partial \hat{H}_v}{\partial Q})_{k+\frac{1}{2}} - (\frac{\partial \hat{H}_v}{\partial Q})_{k-\frac{1}{2}} \\ &= (A_v \Delta Q^n_{k-1} + B_v \Delta Q^n + C_v \Delta Q^n_{k+1})\end{aligned} \tag{60}$$

where

$$A_v = \frac{M_\infty}{Re_L}[\mu J(\frac{|\nabla \zeta|}{J})^2]_{k-\frac{1}{2}}(\frac{\partial \hat{T}}{\partial Q})_{k-1}$$

$$B_v = -\frac{M_\infty}{Re_L}\{[\mu J(\frac{|\nabla \zeta|}{J})^2]_{k+\frac{1}{2}} + [\mu J(\frac{|\nabla \zeta|}{J})^2]_{k-\frac{1}{2}}\}(\frac{\partial \hat{T}}{\partial Q})_k$$

$$C_v = \frac{M_\infty}{Re_L}[\mu J(\frac{|\nabla \zeta|}{J})^2]_{k+\frac{1}{2}}(\frac{\partial \hat{T}}{\partial Q})_{k+1}$$

5.3 Hybrid Algorithm

From the results of the previous section, Eq.(55) may be rewritten as

$$\begin{aligned}&(\frac{V}{\Delta t} I + B_\xi + B_\eta + B_\zeta - B_v)\Delta Q^n + A_\xi \Delta Q^n_{i-1} + C_\xi \Delta Q^n_{i+1} \\ &+ A_\eta \Delta Q^n_{j-1} + C_\eta \Delta Q^n_{j+1} + (A_\zeta - A_v)\Delta Q^n_{k-1} + (C_\zeta - C_v)\Delta Q^n_{k+1} = R(Q^n)\end{aligned} \tag{61}$$

where A_α, B_α, C_α, $\alpha = \xi, \eta, \zeta, v$ are given in Eq.(57), (59) and (60). As mentioned before, Eq.(61) represents a large banded (5 x 5)-block matrix equation so that it is impractical to solve Eq.(61) directly due to required computer memory size. As alternative methods, approximate factorization (AF) or line relaxation algorithm can be considered.

The AF algorithm (Ref.49) with upwind differencing of the residuals is only conditionally stable for a scalar convection equation (Ref.19), so that it has a time-step limitation. It has the significant advantage, however, of being completely vectorizable. The line relaxation algorithms are unconditionally stable for a scalar convection equation (Ref.19,51) and can have quadratic convergence with implicit boundary condition treatment (Ref.51) but, as a disadvantage, are not completely vectorizable.

In order to take the advantage of these algorithms, a hybrid approach is adopted, using relaxation in the streamwise direction and AF in the crossflow plane. The hybrid algorithm avoids the $(\Delta t)^3$ splitting error terms incurred in the 3-D AF method to overcome the severe time-step limitation. Also the hybrid

algorithm is vectorizable by planes and can recover conventional space-marching techniques for completely supersonic flows. In the streamwise direction (ξ – direction), a nonlinear residual update is used to reduce computational efforts. Thus on a forward sweep, $\Delta Q^n_{i+1} = 0$ and on a backward sweep, $\Delta Q^n_{i-1} = 0$.

According to the hybrid algorithm, Eq.(61) can be written as

$$
\begin{aligned}
&[\hat{M} + \delta_\eta \frac{\partial \hat{G}}{\partial Q}]\hat{M}^{-1}[\hat{M} + \delta_\zeta(\frac{\partial \hat{H}}{\partial Q} - \frac{\partial \hat{H}_v}{\partial Q})]\Delta Q^n \\
&\quad = R(Q^{n+1}_{i-2}, Q^{n+1}_{i-1}, Q^n_i, Q^n_{i+1}, Q^n_{i+2}) \quad \textit{on a forward sweep} \\
&\quad = R(Q^n_{i-2}, Q^n_{i-1}, Q^n_i, Q^{n+1}_{i+1}, Q^{n+1}_{i+2}) \quad \textit{on a backward sweep}
\end{aligned}
\tag{62}
$$

where

$$
\hat{M} = \frac{V}{\Delta} I + B_\xi
$$

$$
\delta_\eta \frac{\partial \hat{G}}{\partial Q} \Delta Q^n = B_\eta \Delta Q^n + A_\eta \Delta Q^n_{j-1} + C_\eta \Delta Q_{nj+1}
$$

$$
\delta_\zeta(\frac{\partial \hat{H}}{\partial Q} - \frac{\partial \hat{H}_v}{\partial Q})\Delta Q^n = (B_\zeta + B_v)\Delta Q^n + (A_\zeta + A_v)\Delta Q^n_{k-1} + (C_\zeta + C_v)\Delta Q^n_{k+1}
$$

The numerical solution of Eq.(62) is solved by the sequence.

$$
\begin{aligned}
&(i)\ [\hat{M} + \delta_\eta \frac{\partial \hat{G}}{\partial Q}]\,\Delta Q^* = R(Q^{n+1}_{i-2}, Q^{n+1}_{i-1}, Q^n_i, Q^n_{i+1}, Q^n_{i+2}) \\
&(ii)\ [\hat{M} + \delta_\zeta(\frac{\partial \hat{H}}{\partial Q} - \frac{\partial \hat{H}_v}{\partial Q})]\Delta Q^n = \hat{M}\Delta Q^* \\
&(iii)\ Q^{n+1} = Q^n + \Delta Q^n
\end{aligned}
\tag{63}
$$

5.4 Modified Algorithm for Space Marching

For a supersonic inviscid flow in the streamwise direction, there is no downstream influence. However for a supersonic viscous flow, a subsonic part exists in the boundary layer. In order to suppress this downstream influence in the boundary layer and to apply space marching technique to attached viscous flow calculations, the Vigneron technique (Ref.44,50) is implemented.

For this purpose, the streamwise unsplit flux vector, $\hat{F}$ given in Eq.(6), can be modified as follows

$$\hat{F} = \frac{|\nabla\xi|}{J}\begin{bmatrix} \rho\bar{u} \\ \rho u\bar{u} + \omega\hat{\xi}_x p \\ \rho v\bar{u} + \omega\hat{\xi}_y p \\ \rho w\bar{u} + \omega\hat{\xi}_z p \\ (\rho e_0 + p)\bar{u} \end{bmatrix} \tag{64}$$

The case $\omega = 1$ yields the general thin-layer N-S equations. With the "equivalent" gamma formulation for a real gas, the Jacobian matrix of the above flux vector has eigenvalues

$$\begin{aligned} \lambda_i &= \bar{u} \qquad i = 1,2,3 \\ \lambda_{4,5} &= \frac{1}{2}\{\bar{u}[\tilde{\gamma} + 1 - (\tilde{\gamma} - 1)\omega] \pm \alpha\} \end{aligned} \tag{65}$$

where

$$\alpha = \sqrt{[(1-\omega)(\tilde{\gamma}-1)]^2\bar{u}^2 + 4\omega(\hat{\xi}_x^2 + \hat{\xi}_y^2 + \hat{\xi}_z^2)\tilde{a}^2}$$

$$\tilde{a} = \tilde{\gamma}\frac{p}{\rho}$$

and for $\omega = 1$, $\lambda_{4,5} = \bar{u} \pm \tilde{a}$. Here non-negative eigenvalues result if

$$\omega < \frac{\tilde{\gamma}\tilde{M}_\xi^2}{(\tilde{\gamma}-1)\tilde{M}_\xi^2 + 1} \tag{66}$$

where $\tilde{M}_\xi = \bar{u}/\tilde{a}$. Thus, with ω contrained by Eq.(66), the Jacobian matrix will have all non-negative eigenvalues and a space marching technique can be used. The modified unsplit flux $\hat{F}$ and Jacobian $\frac{\partial \hat{F}}{\partial Q}$ are used in the streamwise direction. The value of ω used in the calculations was obtained from

$$\begin{aligned} f(M_\xi) &= \frac{\sigma\tilde{\gamma}M_\xi^2}{1 + (\tilde{\gamma}-1)M_\xi^2} \\ \omega &= f(M_\xi) \quad for \quad f(M_\xi) < 1 \\ \omega &= 1 \qquad for \quad f(M_\xi) \geq 1 \end{aligned} \tag{67}$$

where σ is a safety factor and $\sigma = 0.95$ is used.

The restriction of the modified algorithm is that it can not be applied to the separated flow in the streamwise direction due to its limiting the streamwise pressure gradient. However, its solution provides an extremely good initial condition for the thin-layer N-S equations (Ref.44). Also this algorithm can retain the second-order accuracy in the streamwise direction so that its solution

is more accurate than the solutions of conventional parabolized N-S algorithms (Ref.44,54).

5.5 Application to Multi-Zone grids

On a multi-zone grid, all solution procedures are exactly same as single zone calculations except for the zonal boundary treatments. At the zonal boundary cell shown in Fig.3, Eq.(62) is written as

$$\begin{aligned}[\hat{M} + \delta_\eta \frac{\partial \hat{G}}{\partial Q}]\hat{M}^{-1}[\hat{M} + \delta_\zeta(\frac{\partial \hat{H}}{\partial Q} - \frac{\partial \hat{H}_v}{\partial Q})]\Delta Q_1^2 \\ = R(Q^1_{imax-2}, Q^1_{imax-1}, Q^2_1, Q^2_2, Q^2_3)\end{aligned} \tag{68}$$

where the superscript 1 and 2 are the zone numbers and the subscript means i index. As seen here, the previous zone values appear only in the residual term due to the nonlinear updating of solution. Since the flux terms in the ξ direction where the grid is patched contain the previous zone values, they are interpolated from the previous zone values using the Ramshaw procedure to complete the calculation. For higher order calculations, Q_{imax-1} of zone 1 is also interpolated.

6. Results and Discussions

6.1 Time Comparison

In order to compare the two rezoning algorithms from a numerical efficiency standpoint, simple rectangular grids in both zones were constructed and values of a single dummy variable were interpolated from zone 1 onto zone 2. Mesh refinement studies were performed and the results of timing the calculations on the VPS-32 at the NASA Langley Research Center are reported in Table 1. As predicted in Section 3.2, an examination of the data in the table reveals that the measured work associated with clipping does indeed increase by a factor of 16 as the grid is doubled in both zones whereas the computational cost of the Ramshaw procedure increases by roughly 4.

6.2 Test Problems

In order to validate the implicit zonal algorithm, both 2-D and 3-D problems were calculated and compared with experimental data and analytic solutions.

6.2.1 Supersonic 2-D Wedge Problem

As the first test case, a high-temperature supersonic flow over a 10^0 wedge followed by a 10^0 expansion was considered. The computational domain is divided into 3 zones and grids are patched at the zonal boundaries as shown in Fig.7. The first zone has 41x2x51 grid points. The second zone has 51x2x51 grid points and the last zone has 111x2x51 grid points. At the inflow boundary, all conditions were fixed at the reference conditions of $T_\infty = 3573^0K$, $p_\infty = 101325N/m^2$, $\rho_\infty = 0.0883Kg/m^3$, and $M_\infty = 5.0$. The outflow boundary is supersonic, therefore, all values were extrapolated from interior point values. The wall tangency was enforced on the surface and symmetry conditions were used on the grid centerline. A plot of the surface temperature distribution is shown in Fig.8. Both the real-gas FDS of Roe and the real-gas FVS of Van Leer results agree with the analytic equilibrium air solution. Also these patched grid solutions are exactly matched to the single grid results in Ref.22. As seen in Fig.9-a and 9-b, the shock and the expansion fan move through the zonal boundary without distortion.

6.2.2 Shock-Boundary Layer Interaction

Another 2-D test problem is that of an oblique shock wave impinging on a laminar boundary layer developing on a flat plate. The conditions correspond to those of Ref.56 at $M_\infty = 2.0$ and $Re_L = 2.96 \times 10^5$ where the Reynolds number is based on the length from the leading edge to the shock impingement point. The computational grid has 2 zones where 31x2x113 grid points in the first zone and 31x2x114 grid points in the second zone as shown in Fig.10. All conditions are fixed at the inflow and top boundary. Adiabatic no-slip boundary conditions are forced at the flat plate surface. At the outflow boundary, values of Q^p are extrapolated from interior points. The Van Leer FVS with second order accuracy is used in the streamwise direction and the Roe FDS with third order accuracy is used in the normal direction along with the min-mod limiter in both directions. The pressure contours in Fig.11 show the compression and expansion waves downstream of the shock impingement, which are caused by the interaction of the incoming shock wave with the separated boundary layer. Also, the incoming shock passes through the zonal boundary smoothly. Fig.12 show the comparison of skin friction from the present results with experiment (Ref.59). Here, the skin friction values vary smoothly through the zonal interface.

6.2.3 Analytic Forebody

Another test problem is the supersonic inviscid/viscous flow field about an analytic forebody representing the cockpit region of a high-performance aircraft. Results are compared with experimental data in Ref.57. The two zone grid for inviscid flow calculations is shown in Fig.13, which has 32x32x22 grid points in the first zone and 52x52x21 in the second zone. Pressure contours in the symmetry plane are shown in Fig.14. The calculations correspond to inviscid flow at $M_\infty = 1.7$ and zero angle of attack. The FVS of Van Leer with the second order accuracy was used in all directions. The figure shows that the shock and the expansion waves over the forebody vary smoothly through the region where the grids are patched. The surface pressure distribution along the upper and lower longitudinal planes of symmetry agree closely with the experimental results as shown in Fig.15. Close examination shows an improvement in results over the single grid (32x32x42) solutions as a result of the finer grid in the second zone. Also it can be seen that at standard atmospheric conditions, the equilibrium air solutions coincide with the perfect gas solutions as expected. The comparison in Fig.16 between pressure contours on the patched and the single grid in the plane just downstream of the patched grid interface shows that the bow shock is captured slightly better on the patched grid due to its finer grid.

In order to verify the possibility of the patched grid approach with a highly stretched grid, a viscous flow case was calculated. Fig.17 shows a highly stretched grid for a turbulent flow calculation, which has 31x61x23 grid points in

the first zone and 41x65x21 in the second zone. The parabolized N-S equations with second order FDS of Roe were solved at $Re_L = 2.33x10^6$ and the eddy viscosity model of Baldwin and Lomax was used. Fig.18 and Fig.19 show the pressure contours and the surface pressure distribution in the symmetry plan, whereas Fig.20 shows the pressure contours in the cross-plane ahead of and after the zonal interface. Note that the surface pressure distribution is more correctly predicted by the turbulent PNS equations than with the Euler equations.

6.3 Applications

With the results of the previous test problems, the patched grid approach has been applied to more realistic 3-D aerodynamic bodies including hypersonic aircraft, model SR-71, and the F-18 forebody-strake.

6.3.1 Hypersonic Aircraft

Single grid (65x65x51) calculations of the flowfield about this configuration have been performed with a perfect gas, thin-layer N-S code (Ref.8) and with an inviscid, real gas assumption (Ref.22). A patched grid was constructed for the two-zone inviscid, equilibrium air calculations presented here by replacing the twenty-two crossflow planes ahead of the delta wing with a polar grid in each plane containing 31x136 points as shown in Fig.21. The 2-zone grid calculation

was run at $M_\infty = 24.5$, $\alpha = 1.0$, $p_\infty = 51.63 N/m^2$, and $\rho_\infty = 0.00066974 Kg/m^3$. Van Leer's FVS was used with first order accuracy in the streamwise direction and second order accuracy in the crossflow plane. This redistribution of grid points allow a very crisp representation of the bow shock as indicated by the enlarged view of the pressure contours and grid in the last plane of the first zone, shown in Fig.22-a. Fig.22-b shows the pressure contours in the first plane downstream of the zonal interface. As seen in the figure, the contours are smooth in most of the plane but jagged in the region which has been locally refined. This has been discussed by Dukowicz in Ref.47. Interpolation from a fine mesh to a coarse mesh results in a smoothing of the data since the coarse cells sample data from several fine cells. However, in the reverse process, that of the interpolating onto a fine mesh from a coarser one, the fine mesh cells are able to 'see' the discontinuities in the data on the coarse mesh. This leads to the small region of jagged contour lines in Fig.22-b. Nonetheless, the calculation is fully conservative. The pressure contours in the last plane of the second zone are shown in Fig.23. Even though the computational results cannot be compared with experimental data, the overall features of the complex wave patterns are physically acceptable.

6.3.2 Model SR-71

In order to demonstrate the capability of the method to handle relatively complex geometries, the inviscid flowfield about the model SR-71 depicted in Fig.24 was calculated. In the calculation, the reference conditions of

$M_\infty = 3.0$, $p_\infty = 5460 N/m^2$, and $\rho_\infty = 0.088 Kg/m^3$ were employed and the second order accurate FVS of Van Leer with the equilibrium air assumption was used. The four zones which were independently generated, were patched together longitudinally. Fig.25 and 26 show the pressure contours in the cross planes just ahead of and just behind the first and third zonal interfaces respectively. Note the significant difference in the grids, particularly at the first interface as seen in Fig.25. In Fig.27, the flowfield near the end of the aircraft in a region where the vertical tails are present is shown. Contours of pressure in the top and bottom planes of symmetry are shown in Fig.28 clearly indicating the shock and expansion waves expected. Note that there is no distortion along the vertical lines in the figure which are locations where the grids are patched together.

6.3.3. F-18 Forebody with Strakes

The calculations of the inviscid flowfield about the F-18 forebody was performed in Ref.41 by using the clipping algorithm. Here, the results of a subsonic viscous flowfield calculation are presented. Two grids which have 31x65x27 points in the first zone and 65x65x30 in the second zone are patched together at the strake apex as shown in Fig.29. At the interface, the grid lines are coincident only at the surface and in the symmetry planes as seen in Fig.30. The calculation was performed at $M_\infty = 0.6$, $\alpha = 20^0$, and $Re = 95000/inch$. The FDS of Roe in the cross plane and the FVS of Van leer in the streamwise direction were used with third order accuary and with the min-mod limiter. Fig.31 shows the pressure

contours in the symmetry planes where the separated and reattached flow field can be seen. The pressure contours around the forebody in the cross planes just ahead of and just behind the zonal interface are presented in Fig.32. The primary vortex formed above the strake can be seen in the Fig.33-a. The complicated nature of this high alpha flowfield can be observed in Fig.32 and Fig.33. A comparison of experimental and numerical streamline patterns is given in Ref.58 and shows excellent overall agreement.

7. Concluding Remarks

In order to resolve the grid generation problems of 3-D complex aerodynamic bodies and to simulate the real gas effect of high temperature flowfields, an efficient computational procedure has been developed.

The real gas formulation by Grossman and Walters is easily incorporated into existing perfect gas upwind codes, especially the Van Leer FVS and the Roe FDS codes. As seen in the results of the wedge problem, the real gas solutions predict much lower and more accurate surface temperatures than the perfect gas solution as expected. Also the real gas solutions at the sea level conditions are coincident with the perfect gas solutions as seen in the analytic forebody calculations. For equilibrium air simulations with curve fit equation of state, an increase of about 60% in computational work over a perfect gas calculation is observed.

As experienced especially in the model SR-71 calculations, the improved geometry handling capability of the patched grid approach over conventional

single approaches is evident. Since the zonal boundaries are implicitly treated, using the patched grid approach does not affect the convergence rate of the algorithm. Furthermore, due to the efficiency of the rezoning algorithm of Ramshaw, it is now possible to apply the fully conservative patched approach to separated flow calculations as seen in the result of the F-18 forebody-strake problem.

Even though the zonal approach has been applied to grids longitudinally patched together in space, it can be easily extended to a laterally patched multi-zone grid such as an engine inlet and body interaction problem. However, the purpose of this work was to show the feasibility of performing conservative zonal calculations in three-dimensions, particularly in support of NASA's high-alpha research program, and this has been accomplished. In addition, the technique can be extended to handle a moving grid problem such as a rotor-stator interaction problem. One could also apply adaptive grid techniques in each zone to get more accurate solutions since the grids are generated indepenently and have minimum constraints due to neighbouring zones. In terms of code development, an important next step would be to generalize the zonal structure to accept the arrangement of grids in an arbitrary fashion. Clearly, there is a lot more that can be accomplished with the multi-zone technology.

References

1. Jameson, A. "Success and Challenges in Computational Aerodynamics ", AIAA 8th Computational Fluid Dynamics Conference, Paper No 87-1184, June 1987.

2. Kutler, P., Steger, J.L. and Bailey, F.R. " Status of Computational Fluid Dynamics in the United States ", AIAA 8th Computational Fluid Dynamics Conference, Paper No 87-1135, June 1987.

3. Shang, J.S. and Scherr, S.J. " Numerical Simulation of the Flow Field Around a Complete Aircraft ", AGARD CP 412, April 1986.

4. Chaussee, D.S. " High Speed Viscous Flow Calculations About Complex Configurations ", AGARD CP 412, April 1986.

5. Kusunose, K., Marcum, D.L., Chen, H.C. and Yu, N.J. " Transonic Analysis of Complex Airplane Configurations ", AIAA Paper No 87-1196, June 1987

6. Kumar, A. and Anderson, G.Y. " Study of Hypersonic Inlet Flow Fields with a Three-Dimentional Navier-Stokes Code ", AIAA Paper No 86-1426

7. Rizk, Y. Chaussee, D. and Steger, J. " Numerical Simulation of the Hypersonic Flow Around Lifting Vehicles ", AGARD CP 428

8. Richardson, P. F. and Morrison, J.H. " Displacement Surface Calculations or a Hypersonic Aircraft ", AIAA Paper No 87-1190, June 1987

9. Deiwert, G.S. " Aerothermodynamics Research at NASA Ames ", AGARD CP 428

10. Kutler, P., Reinhardt, W.A. and Warming, R.F. " Multishocked, Three-Dmensonal Supersonic Flowfields with Real Gas Effects ", *AIAA Journal,*, Vol.11, No.4, pp657-664 1973

11. Moretti, G., Grossman, B., and Marconi, J. JR., " A Complete Numerical Technique for the Calculation of Three-Dimensional Inviscid Supersonic Flows ", AIAA Paper No. 72-192, January 1972

12. Roe, P.L. " Characteristic Based Schemes for the Euler Equations ", Ann. Rev. Fluid Mech., Vol. 18, 1986, pp.337-365.

13. Van Leer, B. " Flux-Vector Splitting for the Euler Equations ", ICASE Report No. 82-30.

14. Harten, A. " High Resolution Schemes for Hypersonic Conservation Laws ", *Journal of Computational Physics,* Vol.49 pp357-393 1983

15. Harten, A., Lax, P.D. and Van Leer, B. " On Upstream Differencing and Godunov Type Schemes for Hyperbolic Conservation Laws ", SIAM Rev. Vol.25, No.1 pp35-62, Jan. 1983

16. Steger, J.L. and Warming, R.F. " Flux Vector Splitting of the Inviscid Gasdynamic Equations with Application to Finite-Difference Methods ", *Journal of Computational Physics,* Vol.40 pp263-293 1981

17. Thomas, J.L. and Walters, R.W. " Upwind Relaxation Algorithms for the Navier-Stokes Equations ", AIAA Paper 85-1501, July 1985

18. Chakravarthy, S.R. " High Resolution Upwind Formulations for the Navier-Stokes Equations ", von Karman Institute for Fluid Dynamics LS 1988-05, Vol.2 March 1988

19. Thomas, J.L., Van Leer, B. and Walters, R.W. " Implicit Flux-Split Schemes for the Euler Equations ", AIAA Paper 85-1680, July 1985

20. Van Leer, B., Thomas, J.L., Roe, P.l. and Newsome, R.W. " A Comparison of Numerical Flux Formulars for the Euler and Navier-Stokes Equations ", AIAA Paper 87-1104, June 1987

21. Grossman, B and Walters, R.W. " An Analysis of Flux-Split Algorithms for Euler's Equations with Real Gases "", AIAA 8th Computational Fluid Dynamics Conference, paper no. 87-1117 cp, June 1987.

22. Grossman, B and Walters, R.W. " Flux-Split Algorithms for the Multi-Dimensional Euler Equations with Real Gases ", Symposiom on Physical Aspects of Numerical Gasdynamics, August 1987.

23. Colella, P. and Glaz, P.M. " Efficient Solution Algorithms for the Riemann Problem for Real Gases ", *Journal of Computational Physics,* Vol.59, 1985, pp264-289

24. Eberhardt, S. and Palmer, G. " A Two-Dimensional TVD Numerical Scheme for Inviscid High Mach Number Flows in Chemical Equilibrium ", AIAA Paper 86-1284, June 1986

25. Srinivasan, S., Tannehill, J.C., and Weilmuenster, K.J. " Simplified Curve Fits for the Thermodynamic Properties of Equilibrium Air ", NASA Reference Publication 1181, August 1987.

26. Clarke, D.K., Salas, M.D. and Hassan, H.A. " Euler Calculation for Multi-Element Aerofoils Using Cartesian Grids ", *AIAA Journal* Vol.24, No.3, March 1986

27. Choi, S.K. and Grossman, B. " A Flux-Vector Split, Finite-Volume Method for Euler's Equations on Non-Mapped Grids ", AIAA Paper No. 88-0227, January 1988.

28. Jameson, A., Baker., T.J. and Weatherill, N.P., " Calculation of Inviscid Transonic Flow over a Complete Aircraft ", AIAA Paper No. 86-0103, Jan. 1986

29. Jameson, A. and Baker, T.J., " Improvement to the Aircraft Euler Method ", AIAA Paper 87-0452, Jan. 1987

30. Loehner, R., " Simulation of Strongly Unsteady Flows by the Finite Element Method ", AIAA Paper 87-0555, Jan. 1987

31. Thompson, J.F., Warsi, Z.U.A. and Wayne Mastin, C. *Numreical Grid Generation* North-Holland, 1985

32. Weatherill, N.P. and Forsey, C.R. " Grid Generation and Flow Calculations for Aircraft Geometries ", *Journal of Aircraft* , Vol.22, No.10, Oct. 1985

33. Thompson, J.F. " Multi-Zone Euler Marching Technique for Flow over Single and Multi-Body Configurations " AIAA Paper No. 87-0592, January 1987.

34. Steger, J.L. and Benek, J.A. " On the Use of Composite Grid Schemes in Computational Aerodynamics ", Computer Methods in Applied Mechanics and Engineering, Vol. 64, pp 301-320, 1987.

35. Hessenius, K.A. and Rai, M.M. " Three dimensional, Conservative, Euler Computations using Patched Grid Systems and Explicit Methods ", AIAA 86-1081, May 1986.

36. Rai, M.M. " Unsteady Three-Dimensional Navier Stokes Simulations of Turbine Rotor-Stator Interaction ", AIAA 87-2058.

37. Szema, K.Y., Chakaravarthy, S.R., Riba, W.T., Byerly, J., and Dresser, H.S. " Multi-Zone Euler Marching Technique for Flow over Single and Multi-Body Configurations ", AIAA paper no. 87-0592, January 1987.

38. Walters, R.W., Thomas, J.L., and Switzer, G.F. " Aspects and Applications of Patched Grid Calculations ", AIAA 86-1063, May, 1986.

39. Nakahashi, K. and Obayashi, S. " FDM-FEM Zonal Approach for Viscous Flow Computation over Multiple-Bodies ", AIAA 87-1184, January, 1987.

40. Kathong, M., Tiwari, S.N., and Smith, R.E. " A Conservative Approach for Flow Field Calculations on Multiple Grids ", AIAA 88-0224.

41. Walters, R.W., Reu, T., McGrory, W.D., Thomas, J.L. and Richardson, P.F., " A Longitudinally-Patched Grid Approach with Applications to High Speed Flows ", AIAA 88-0715, AIAA 26th Aerospace Science Meeting, Reno, Nevada, January 1988.

42. Walters R.W., Reu, T., Thomas, J.L. and McGrory, W.D., " Zonal Techniques for Flowfield Simulation about Aircraft ", Symposium on Advances and Trends in Computational Structural Mechanics and Fluid Dynamics, October 17-19, 1988

43. Schmatz, M.A., " Simulation of Viscous Flows by Zonal Solutions of the Euler, Boundary-Layer and Navier-Stokes Equations ", *Z. Flugwiss. Weltraumforsch* , No.11 pp281-290, 1987

44. Newsome, R.W., Walters, R.W., and Thomas, J.L., " An Efficient Iteration Strategy for Upwind Relaxation Solutions of the Thin-Layer Navier-Stokes Equations ", AIAA 8th Computational Fluid Dynamics Conference, Paper No 87-1113 CP, June 1987

45. Newmann, W.M. and Sproulli, R.F., *Principles of Interactive Computer Graphics* McGraw-Hill, New York, 1979

46. Ramshaw, J.D. " Conservative Rezoning Algorithms for Generalized Two-Dimensional Meshes ", *Journal of Computational Physics* , Vol. 59, pp 193-199, 1985.

47. Dukowicz, J.K. " Conservative Rezoning (Remapping) for General Quadrilateral Meshes ", *Journal of Computational Physics* , Vol. 54, pp 411-424, 1984.

48. Baldwin, B.S. and Lomax, H., " Thin Layer Approximation and Algebraic Model for Separeted Turbulent Flows ", AIAA Paper No.78-257, January 1978

49. Vatsa V.N., Thomas, J.L., and Wedan, B.W., " Navier-Stokes Computations of Prolate Spheroids at Angle of Attack ", AIAA Paper No.87-2627, August 1987

50. Vigneron, Y.C., Rakich, J.V., and Tannehill, J.C., " Calculation of Supersonic Viscous Flow over Delta Wings with Sharp Subsonic Leading Edges ", AIAA Paper No.78-1137, July 1978

51. Walters, R.W. and Dwoyer, D.L., " An Efficient Iteration Strategy Based on Upwind/Relaxation Schemes for the Euler Equations ", AIAA Paper No.85-1529 CP, July 1985

52. Anderson, W.K., Thomas, J.L., and Van Leer, B., " A Comparison of Finite Volume Flux Vector Splitting for the Euler Equations ", AIAA Paper No.85-0122, January 1985

53. Barth, T.J., " Analysis of Implicit Local Linearization Technique for Upwind and TVD Algorithms ", AIAA Paper No.87-0595, January 1987

54. Lawrence, S.L., Tannehill, J.C., and Chaussee, D.S., "An Upwind Algorithm for the Parabolized Navier-Stokes Equations ", AIAA Paper No.86-1117, May 1986

55. Mehlhorn, K., *Multi-Dimensional Searching and Computational Geometry* , Springer-Verlag, 1984

56. Thomas, J.L., Walters, R.W., Rudy, D.H., and Swanson, R.C., "Upwind Relaxation Algorithms for Euler/Navier-Stokes Equations ", NASA Langley Research Center Symposium on Aerodynamics, April 23-25, 1985

57. Townsend, J.C., Howell, D.T., Collins, I.K., and Hayes, C., "Surface Pressure Data on a Series of Analytic Forebodies at Mach Numbers from 1.70 to 4.50 and Combines Angles of Attack and Sideslip" , NASA TM 80062, June 1979

58. Thomas, J.L., Walters, R.W., Reu, T., Ghaffari, F., Weston, R.P., and Luckring, J.M., " A Patched-Grid Algorithm for Complex Configurations Directed Towards the F-18 Aircraft ", Under preparation for AIAA 27th Aerospace Sciences Meeting, Jan. 9-12, 1989

59. Hakkinen, R.J., Greber, I., Trilling, L., and Arbarbanel, S.S., " The Interaction of an Oblique Shock Wave with a Laminar Boundary Layer ", NASA Memo-2-18-59W, March 1959.

60. MacCormack, R.W. and Baldwin, B.S., " A Numerical Method for Solving the Navier-Stokes Equations with Application to Shock-Boundary Layer Interactions ", AIAA Paper No. 75-1, January 1975.

61. Bruno, C., " Nonequilibrium Reacting Flows ", von Karman Institute for Fluid Dynamics, LS 1987-04, Vol. 2, March 1987.

62. Hayes, W.D. and Probstein, R.F., *Hypersonic Flow Theory* , Academic Press, 1959.

Figures

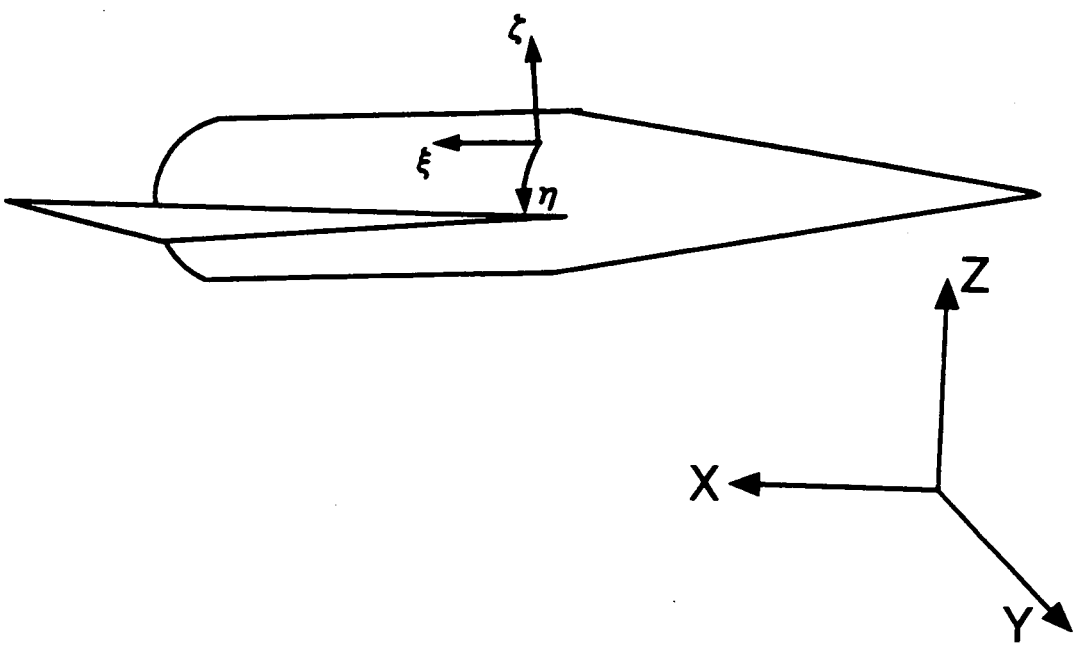

Figure 1. Body fitted coordinate system.

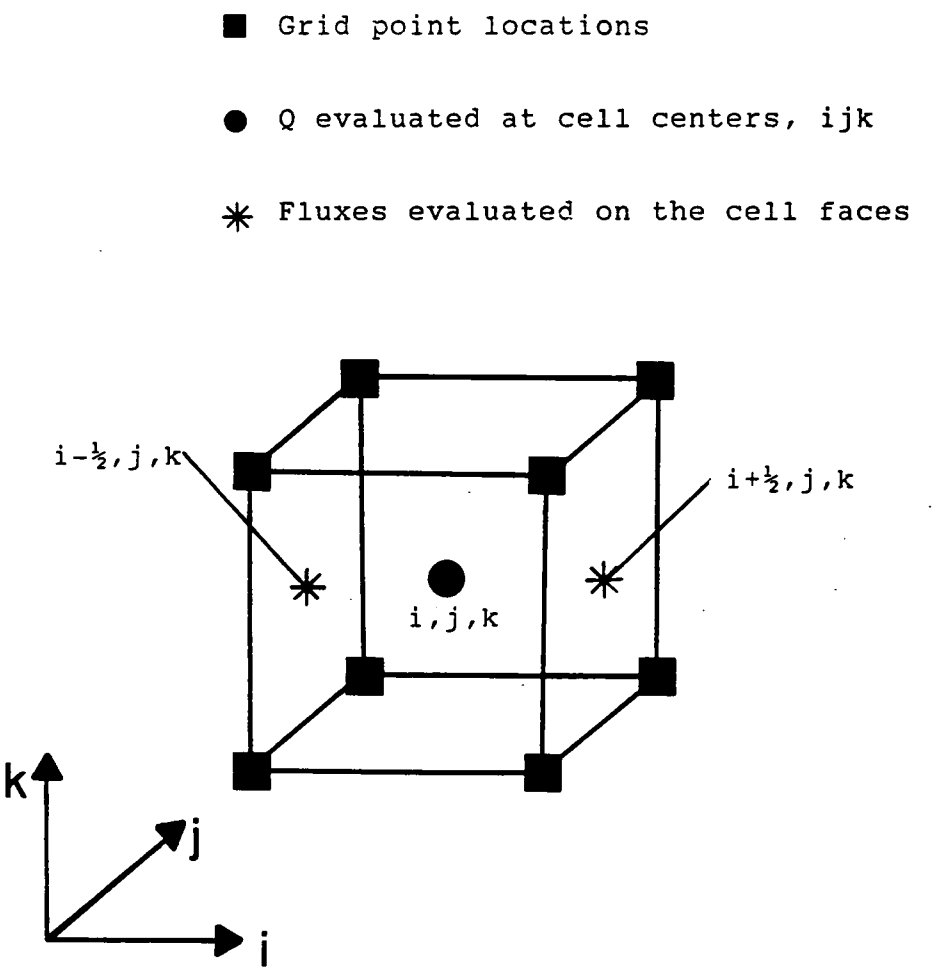

Figure 2. Cell-centered finite volume formulation.

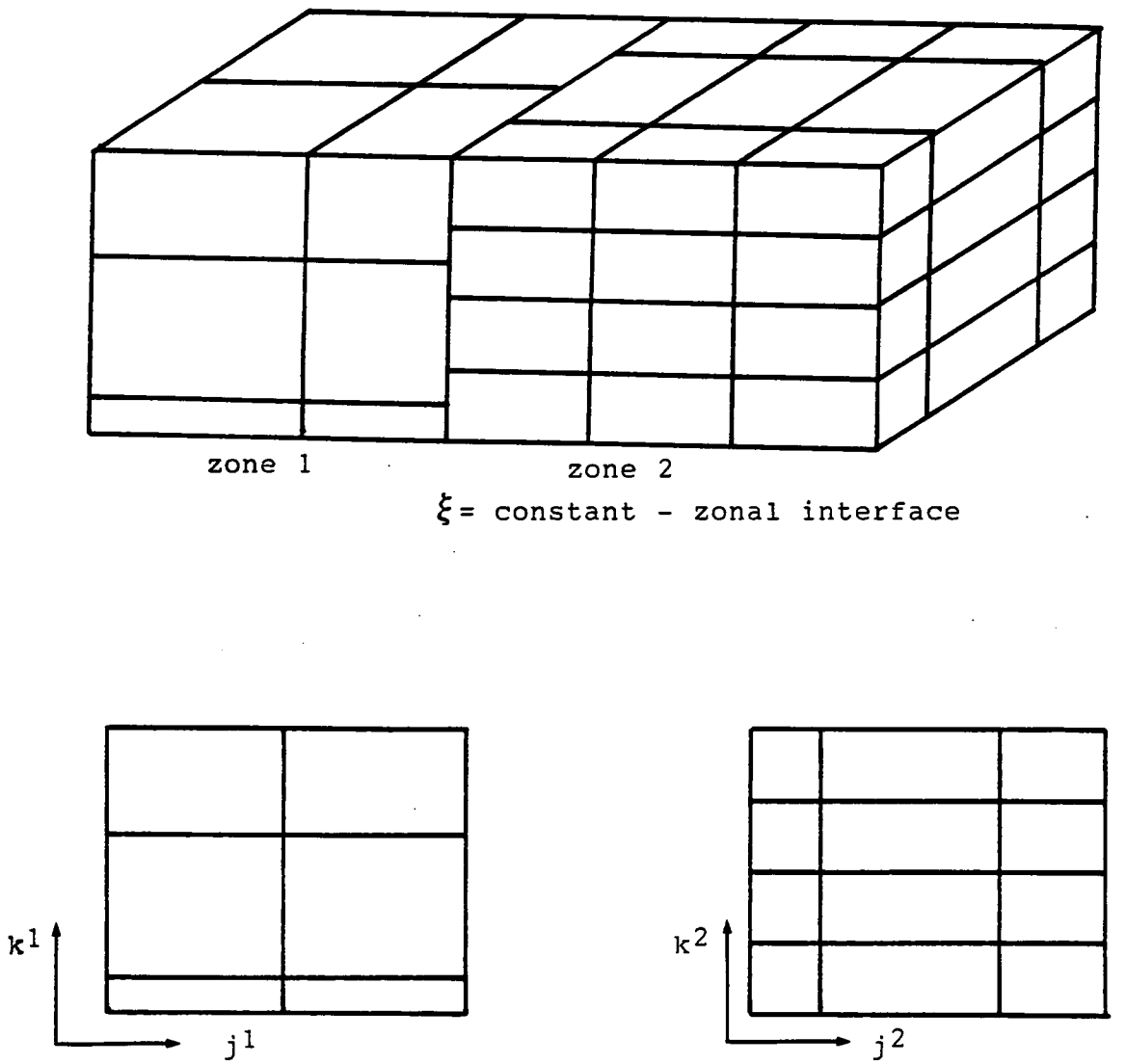

Figure 3. Schemetic view of a patched grid

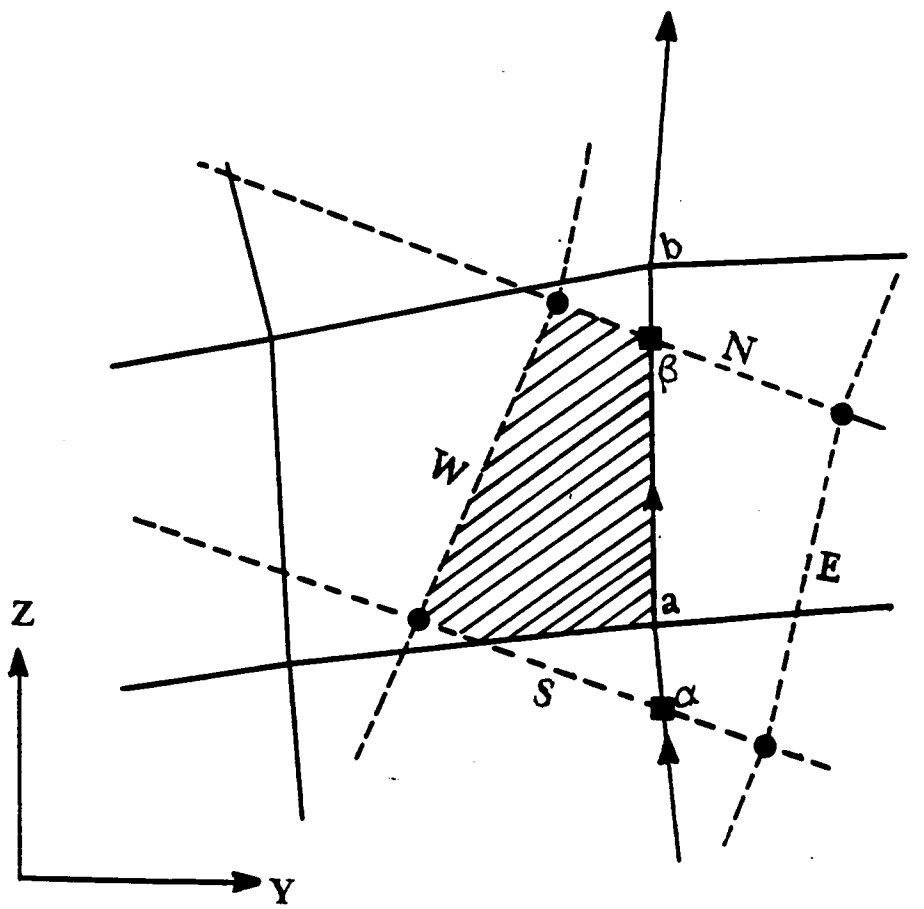

Figure 4. Arbitrary overlapping cell faces at a zonal interface.

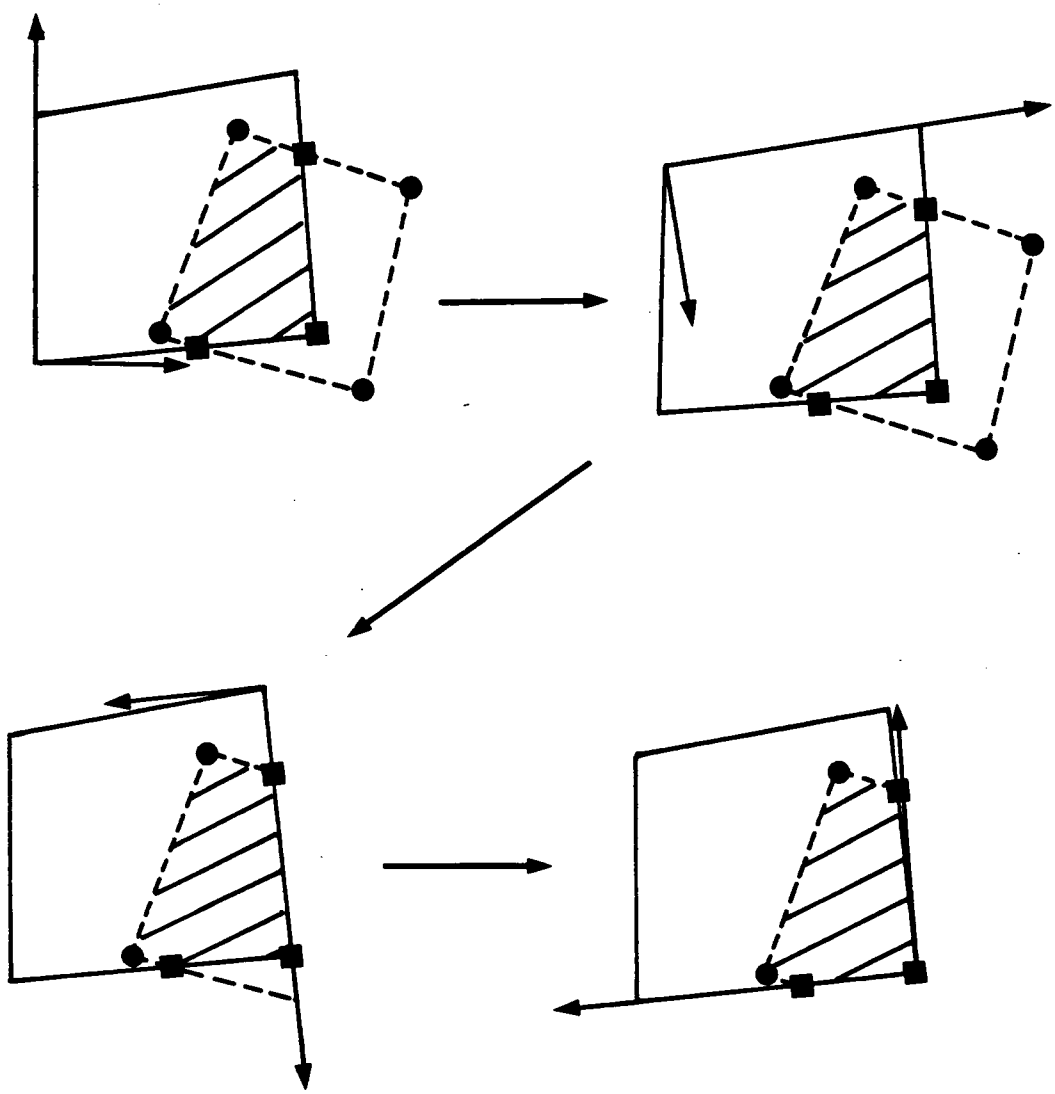

Figure 5. Clipping procedure.

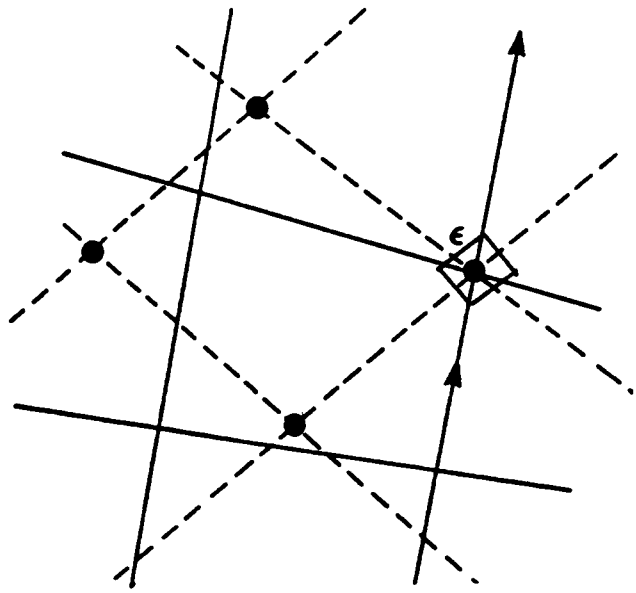

(a)

--------- zone 1 grid
———————— zone 2 grid

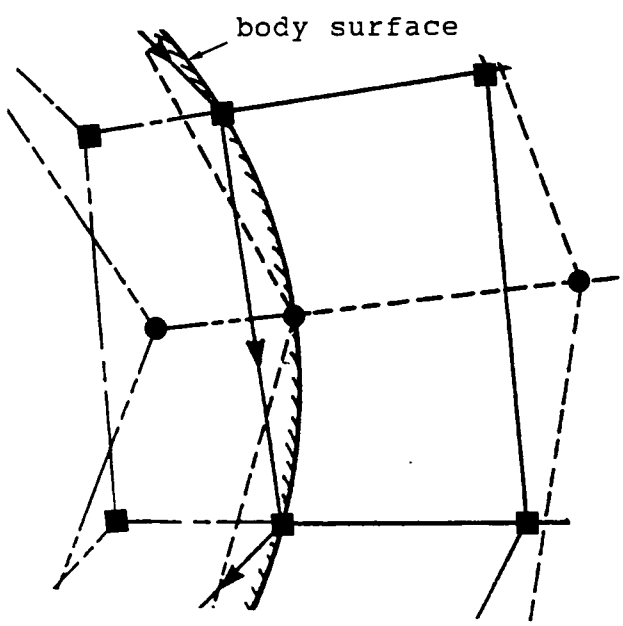

Figure 6. Special considerations for Ramshaw algorithm.

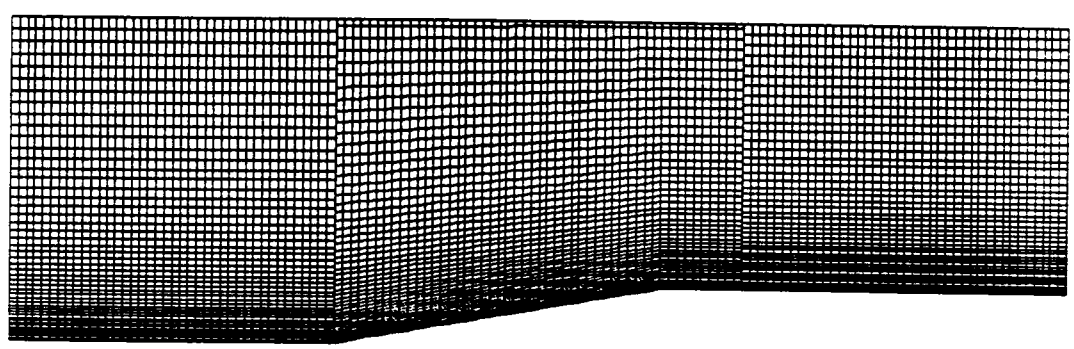

Figure 7. Enlarged view of a 10^0 wedge patched grid.

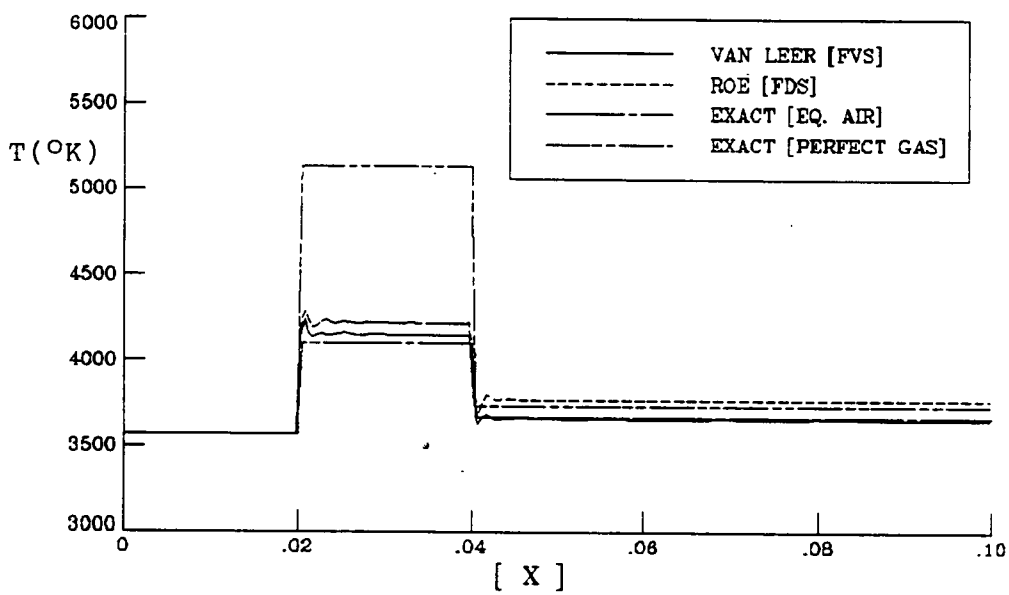

Figure 8. Lower surface temperature distribution of a 10 ^{0} wedge.

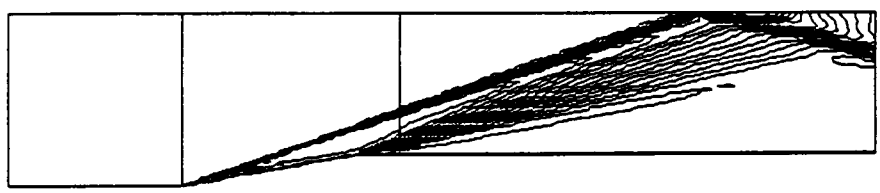

(a)

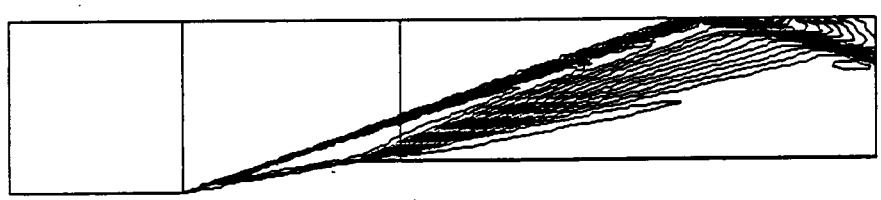

(b)

Figure 9. Temperature contours of (a) Roe's FDS and (b) Van Leer's FVS.

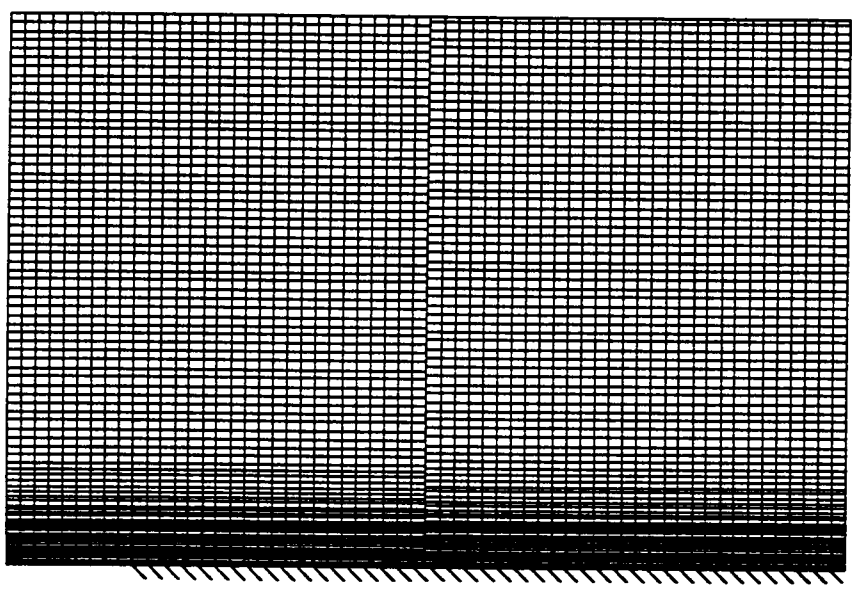

Figure 10. Two zone patched grid of a flat plate.

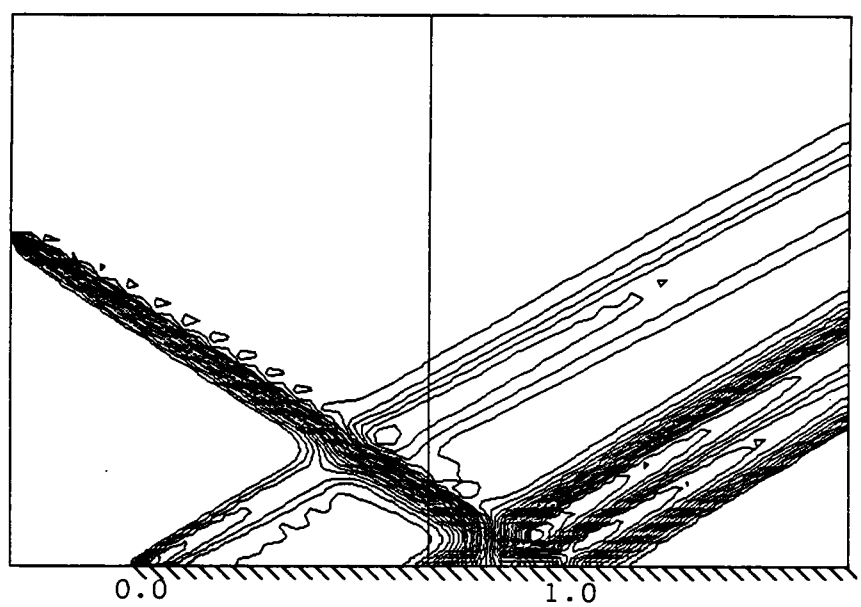

Figure 11. Pressure contours of shock-boundary layer interaction problem.

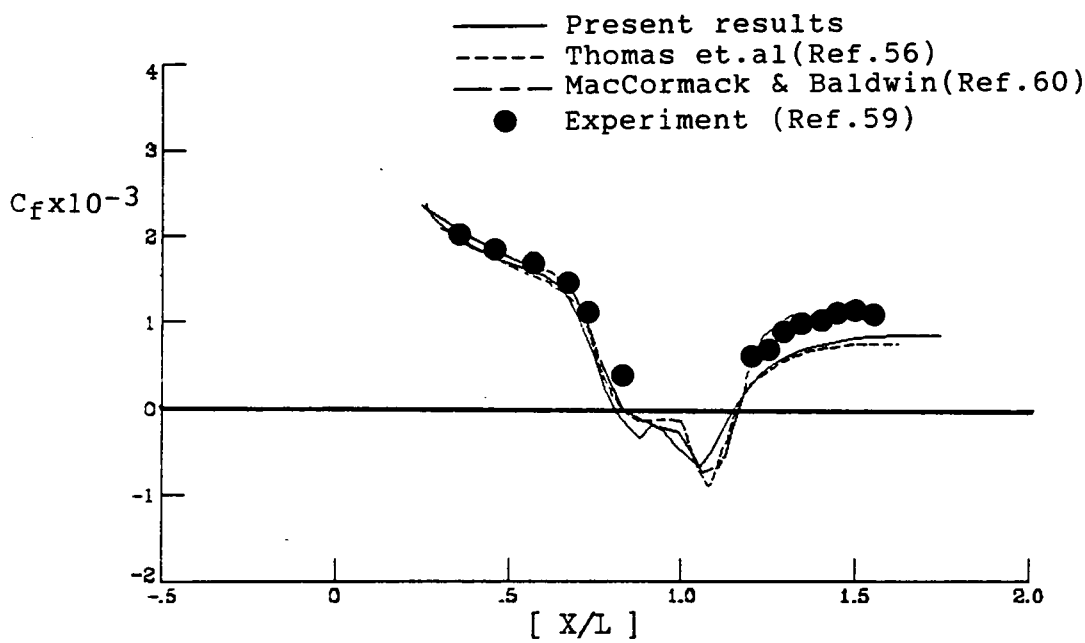

Figure 12. Comparison of wall skin friction coefficient distribution with experiment.

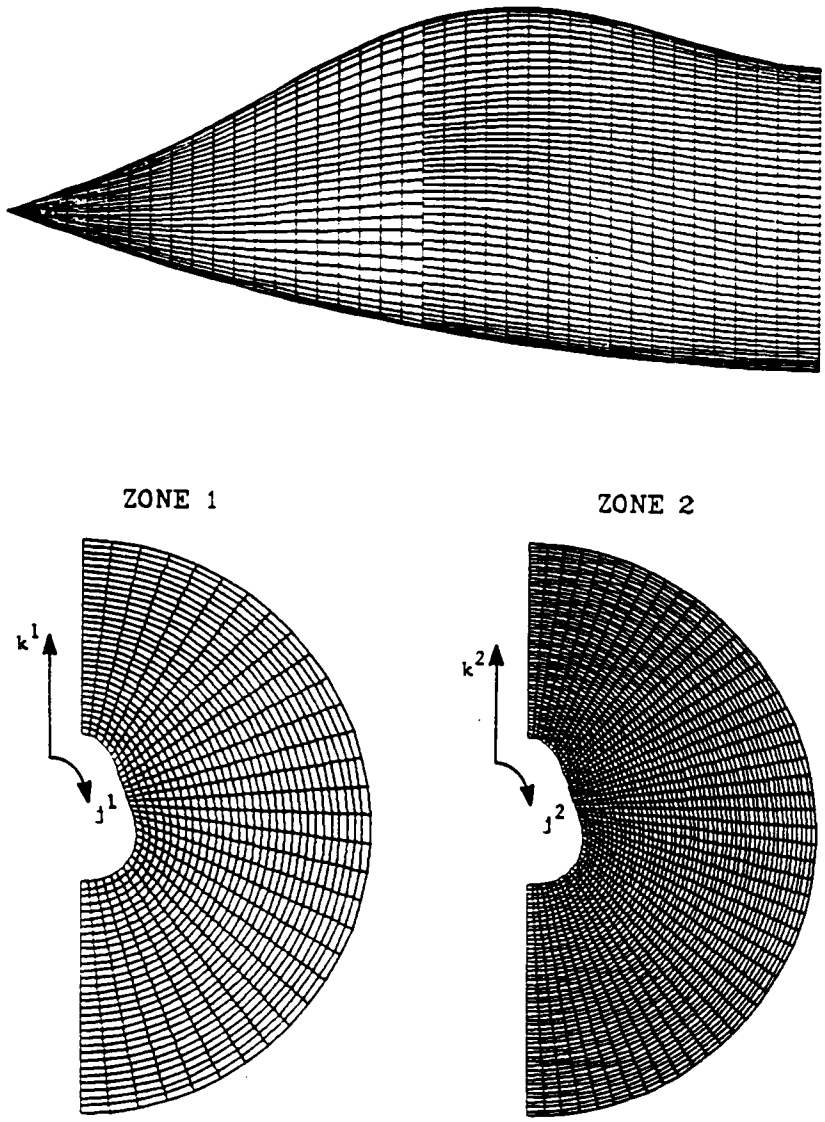

Figure 13. Two zone patched grid of an analytic forebody.

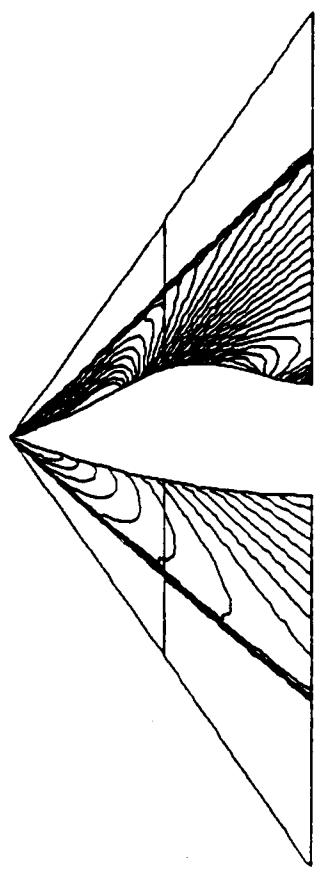

Figure 14. Pressure contours in the symmetry plane of the anayltic forebody.

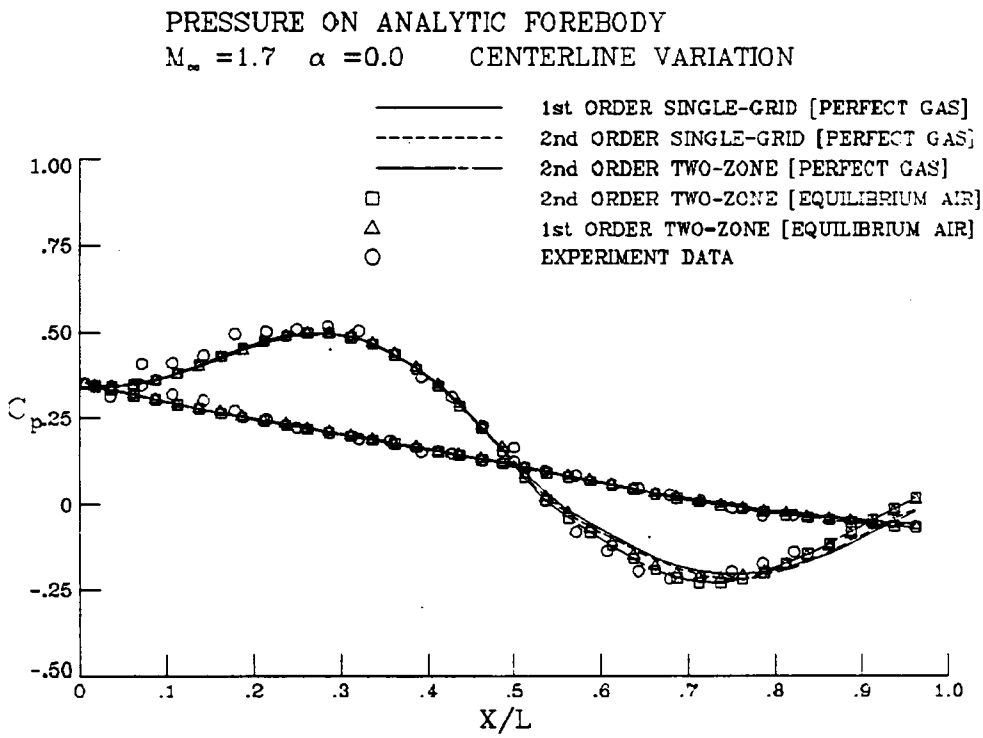

Figure 15. Comparison of the longitudinal surface pressure distribution with experiment (Ref.57) in the symmetry plane.

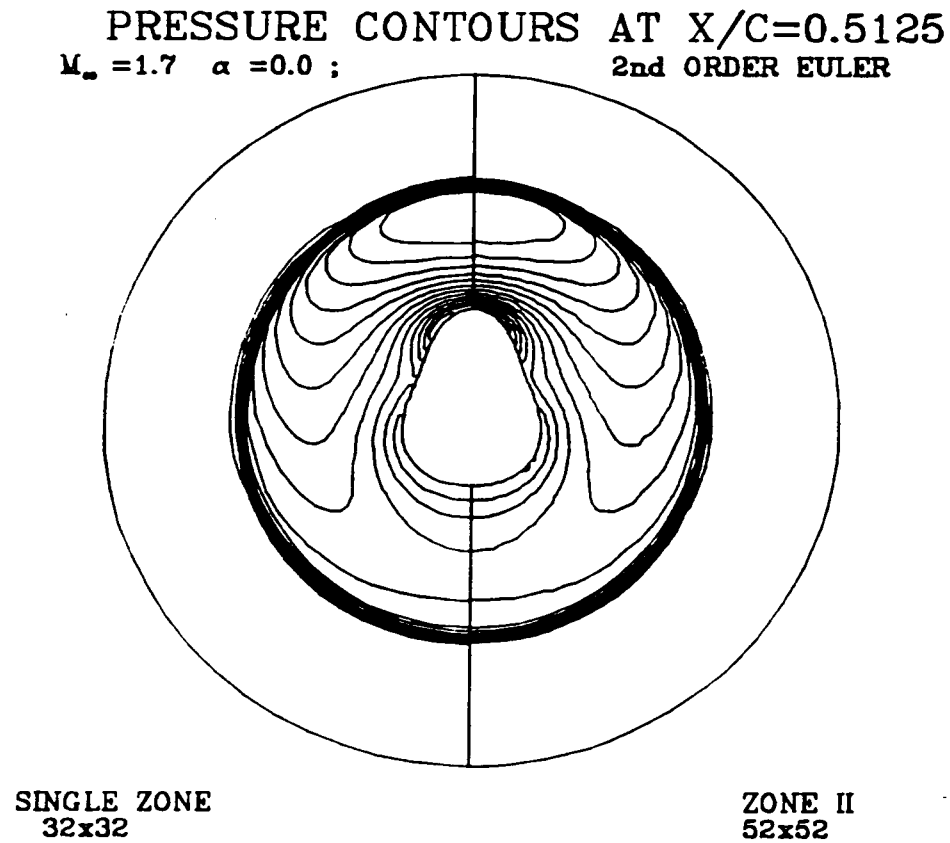

Figure 16. Comparison of pressure contours in the first plane downstream of the zonal interface with single grid pressure contours.

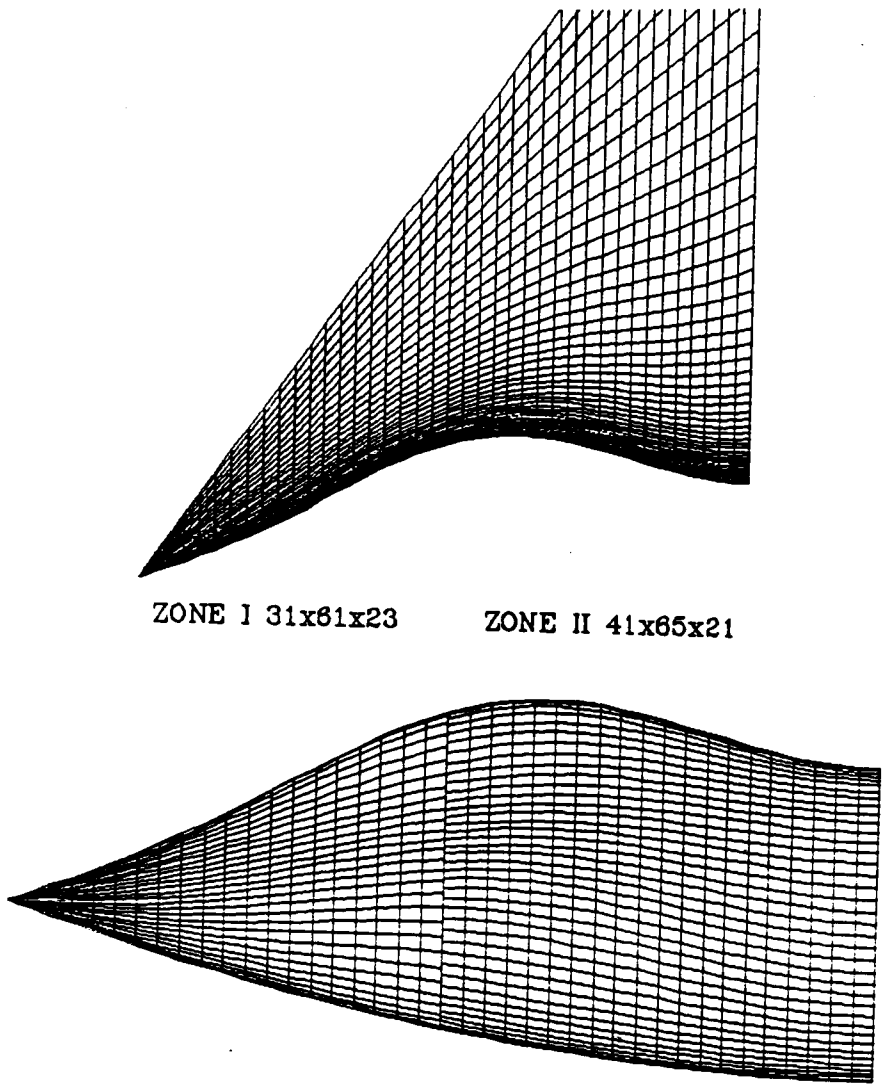

Figure 17. Highly stretched two zone patched grid of an analytic forebody.

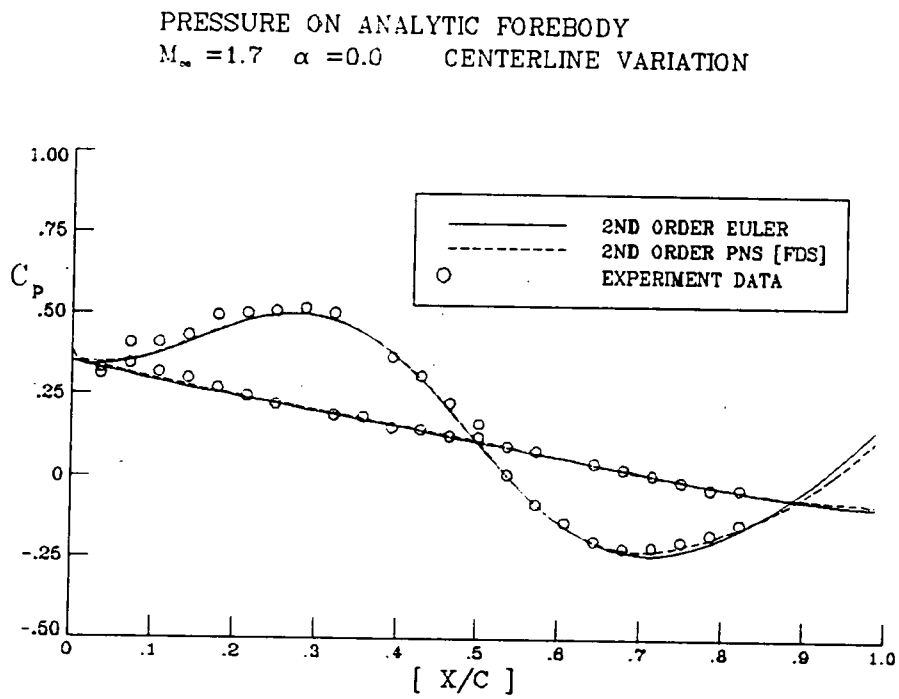

Figure 18. Pressure contours in the symmetry plane of the anayltic forebody.

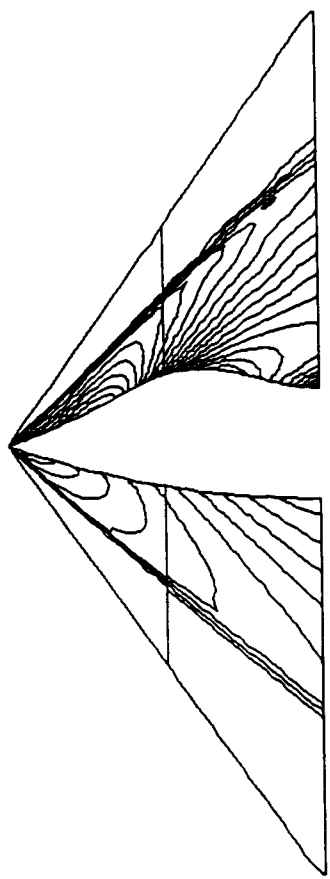

Figure 19. Comparison of the longitudinal surface pressure distribution with experiment (Ref.57) in the symmetry plane.

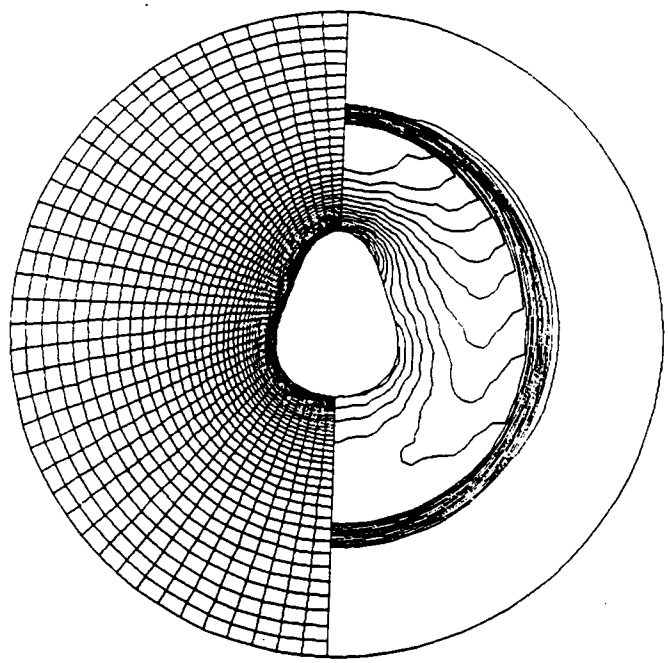

(a)

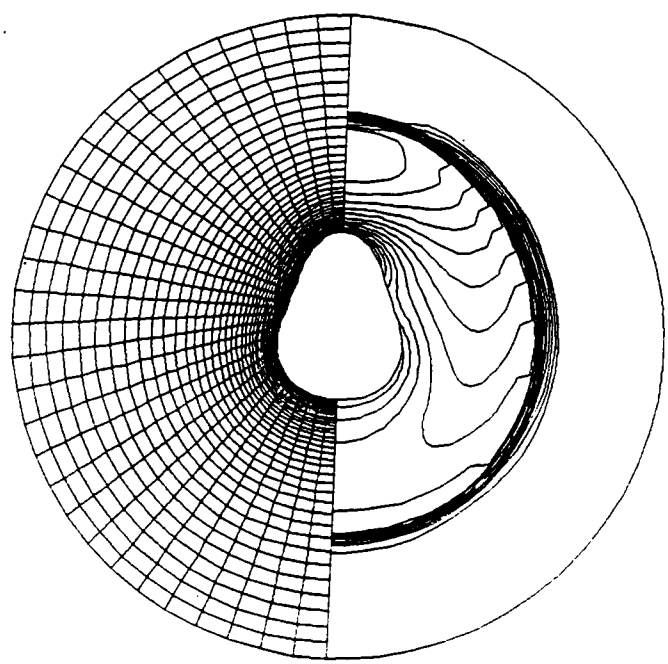

(b)

Figure 20. Pressure contours in the planes just (a) ahead of and (b) behind the zonal interface.

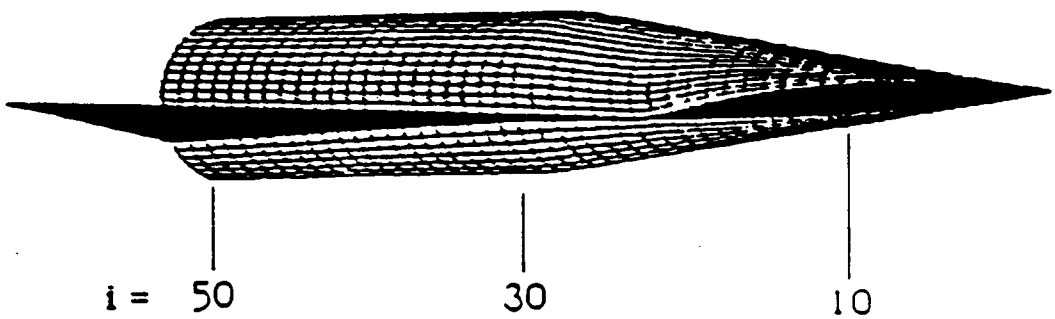

(a)

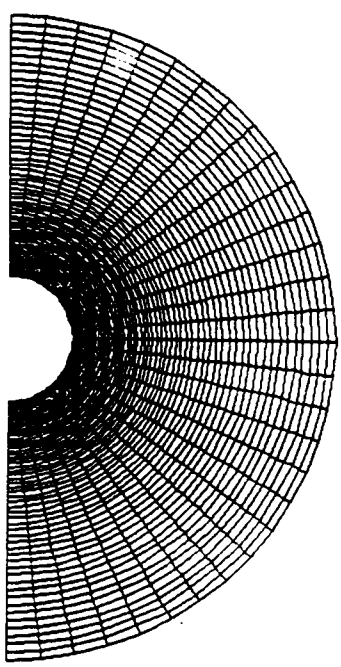

(b) 31x136

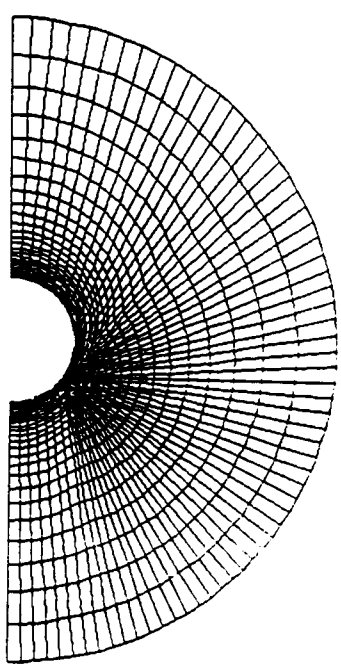

(c) 65x65

Figure 21. (a) Hypersonic aircraft (single grid from Ref.8), (b) Zone 1 cross-plane grid, and (c) Zone 2 cross-plane grid at the zonal interface.

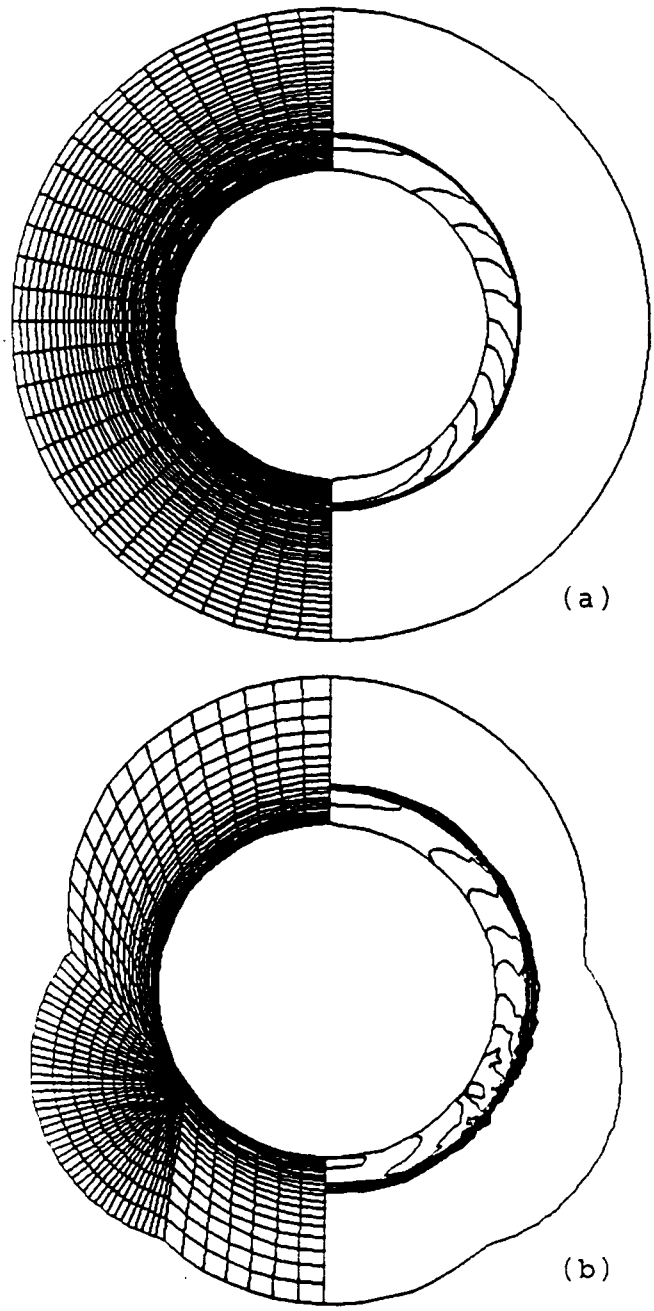

Figure 22. Pressure contours in the cross planes immediately (a) ahead of and (b) behind the zonal interface of the hypersonic aircraft.

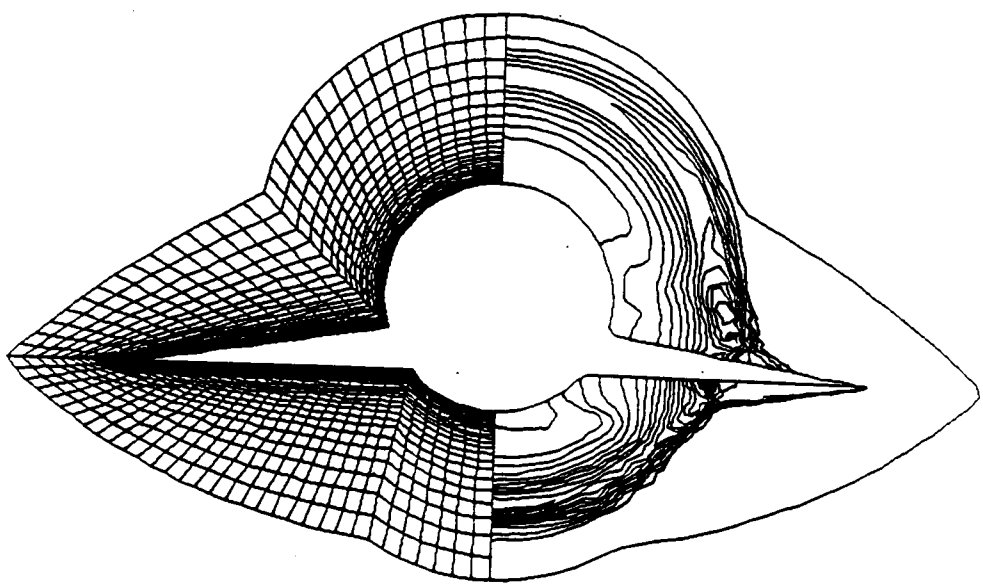

Figure 23. Pressure contours in the last plane of the hypersonic aircraft.

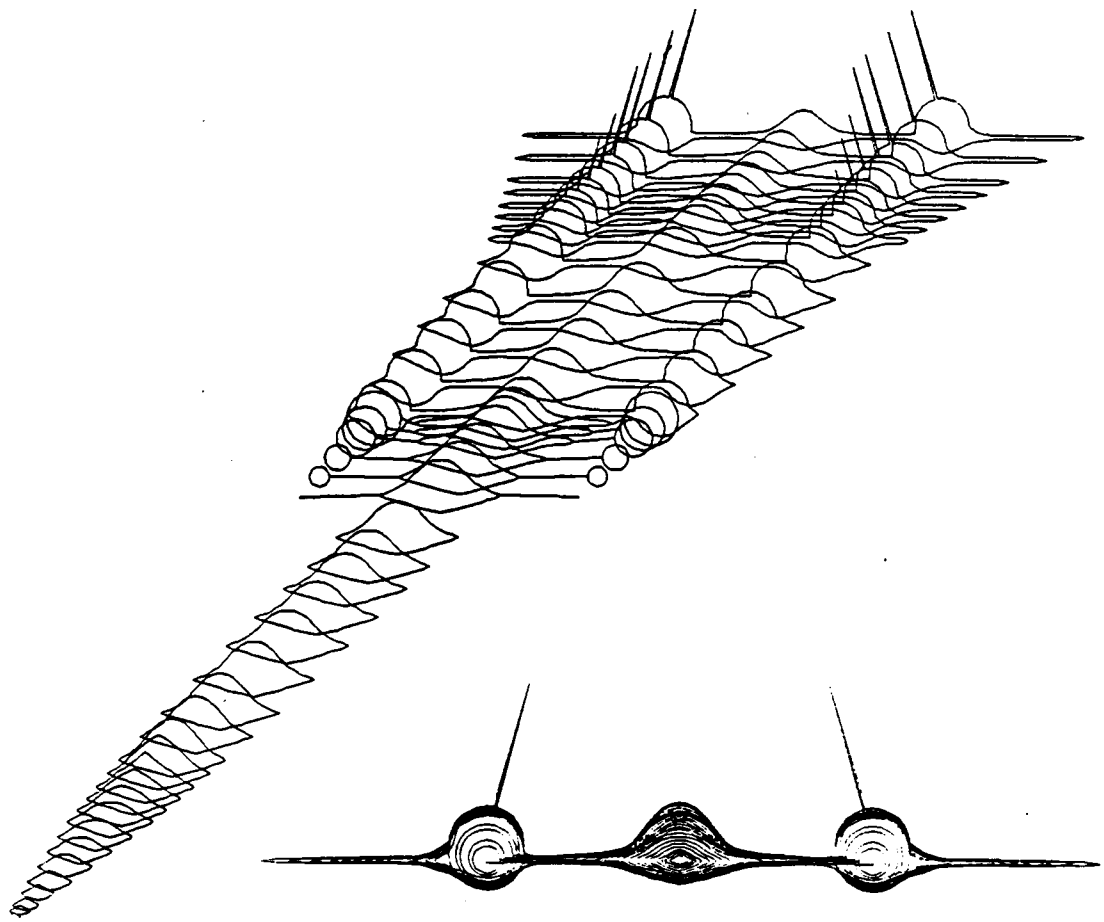

Figure 24. Model SR-71

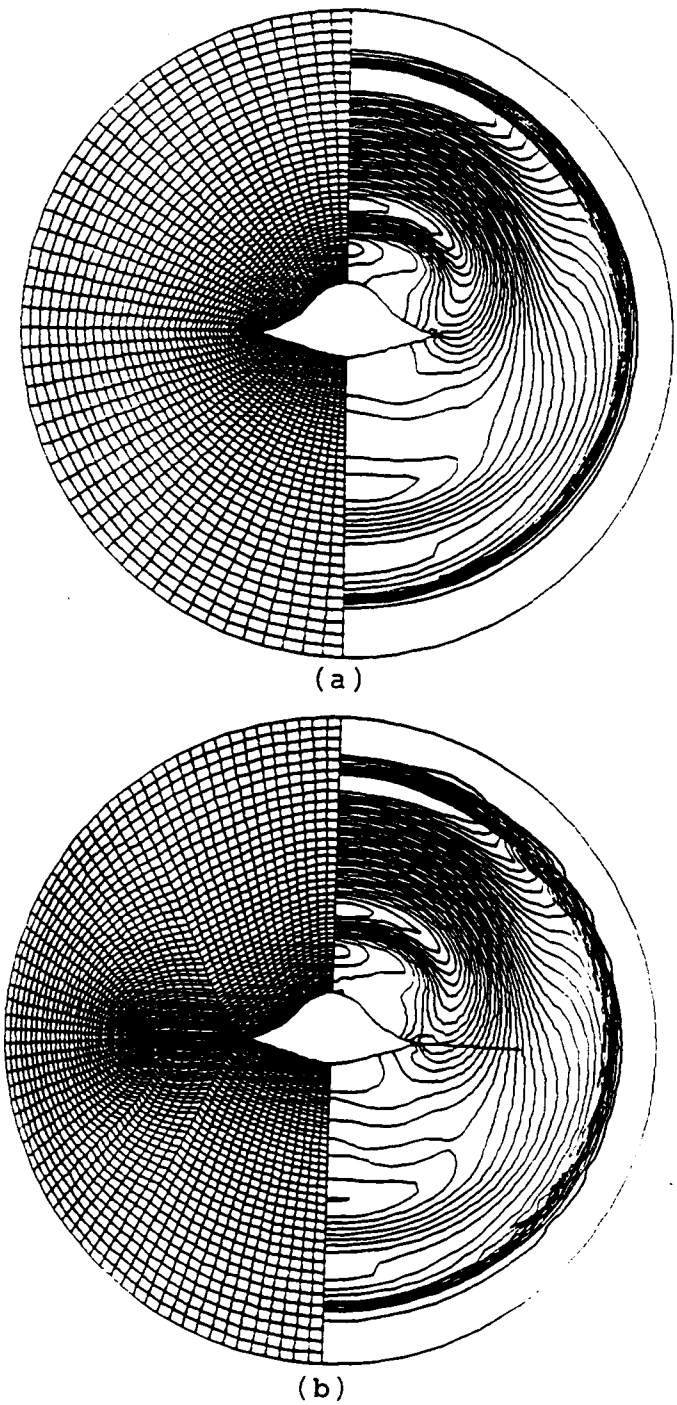

Figure 25. Pressure contours in the cross planes (a) just ahead of and (b) just behind the first zonal interface.

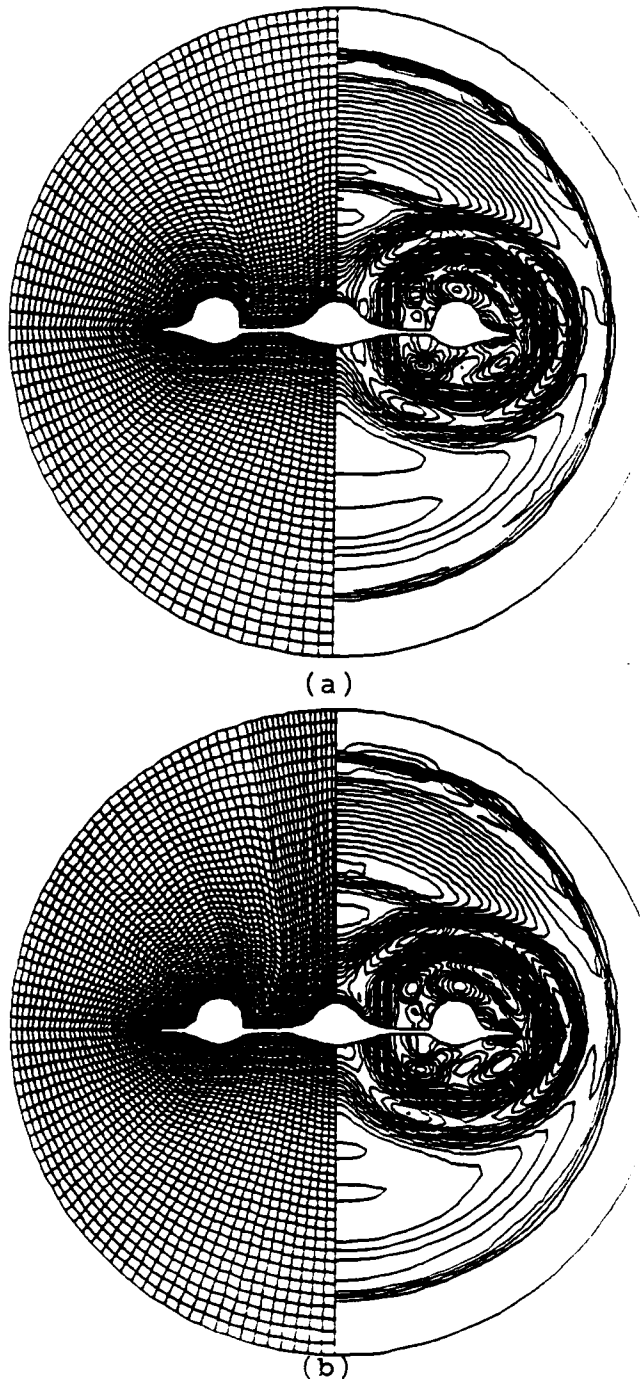

Figure 26. Pressure contours in the cross planes (a) just ahead of and (b) just behind the third zonal interface.

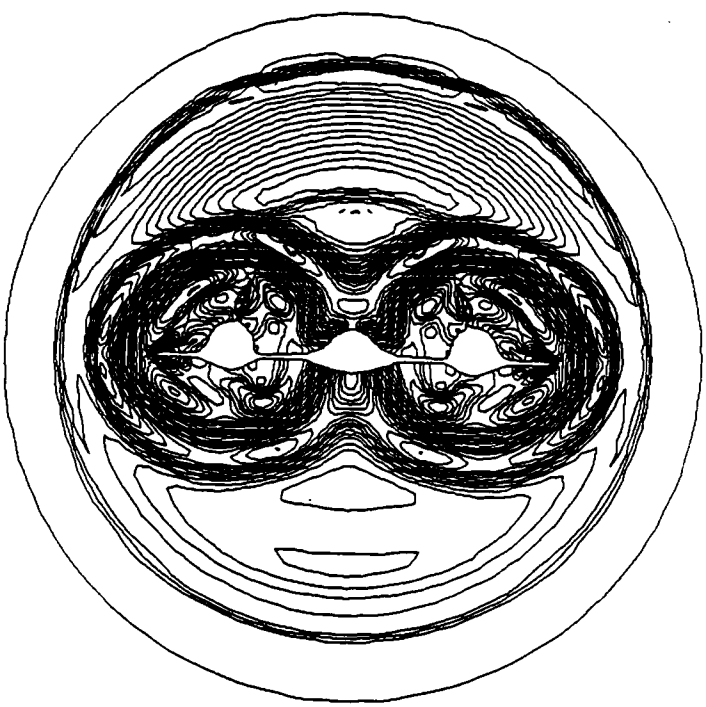

Figure 27. Pressure contours in the last plane.

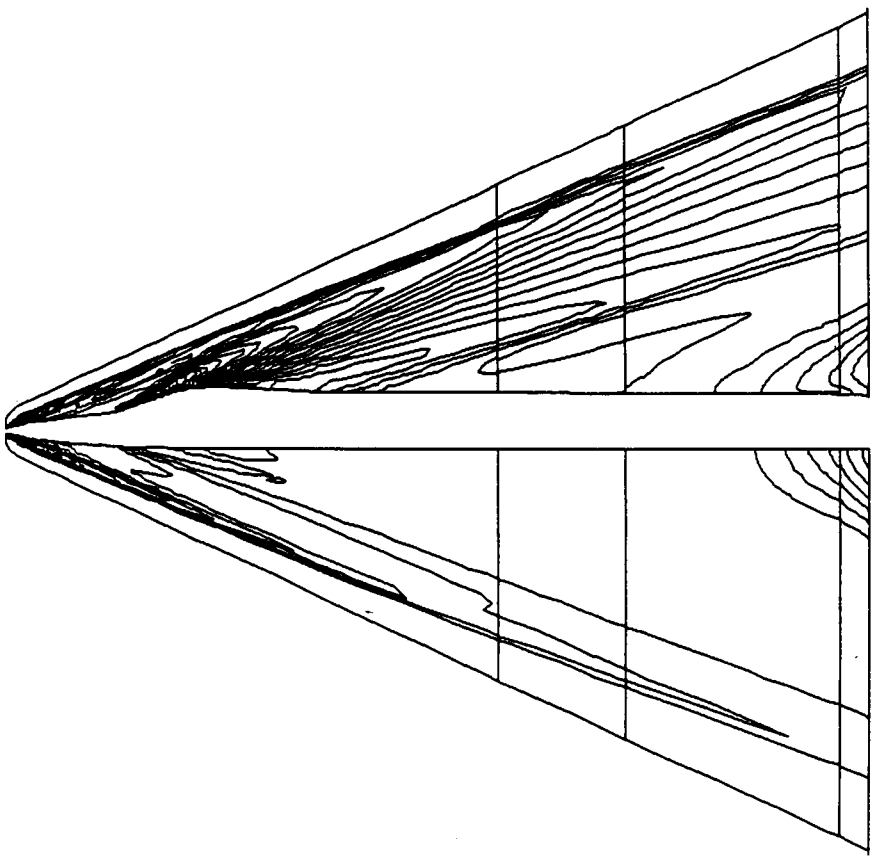

Figure 28. Pressure contours in the plane of symmetry.

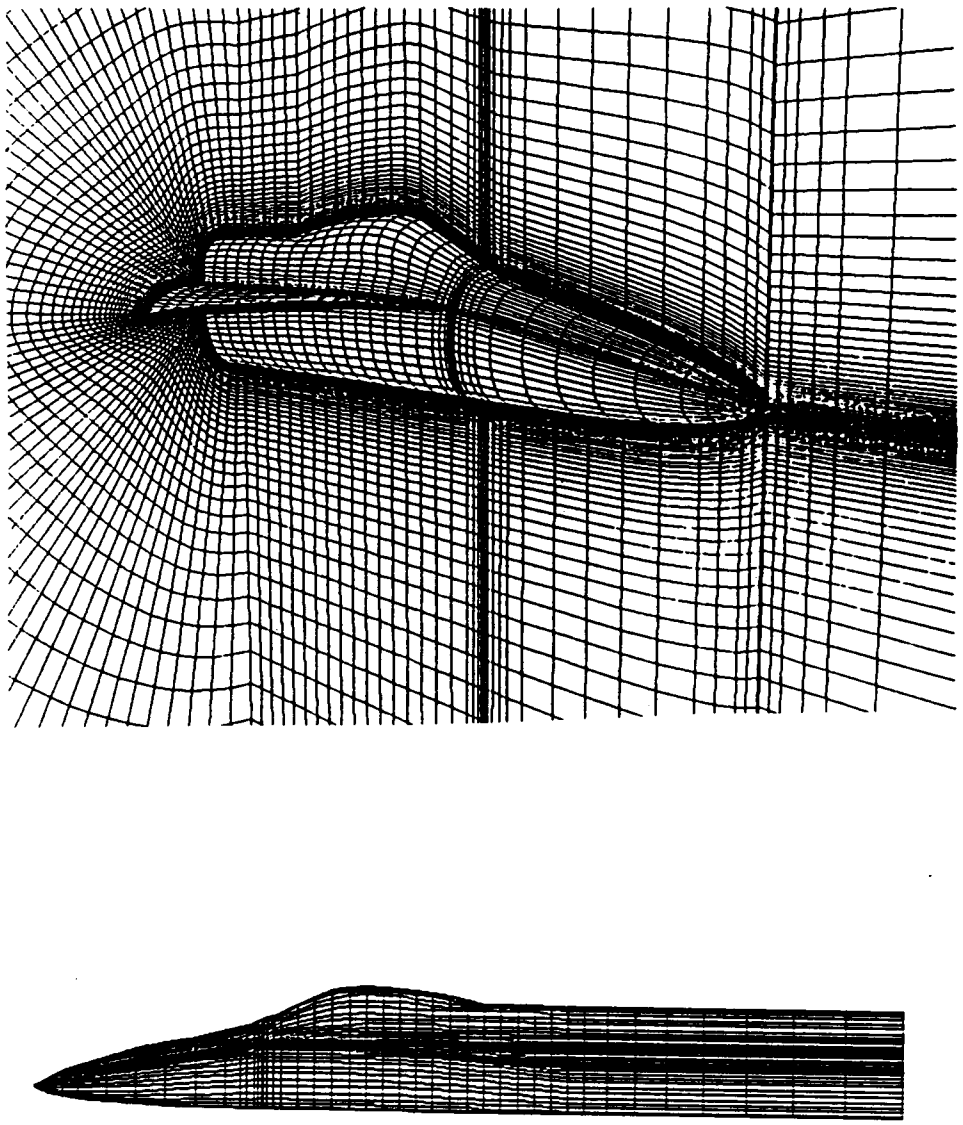

Figure 29. Computational grid of F-18, (a) enlarged view and (b) surface grid.

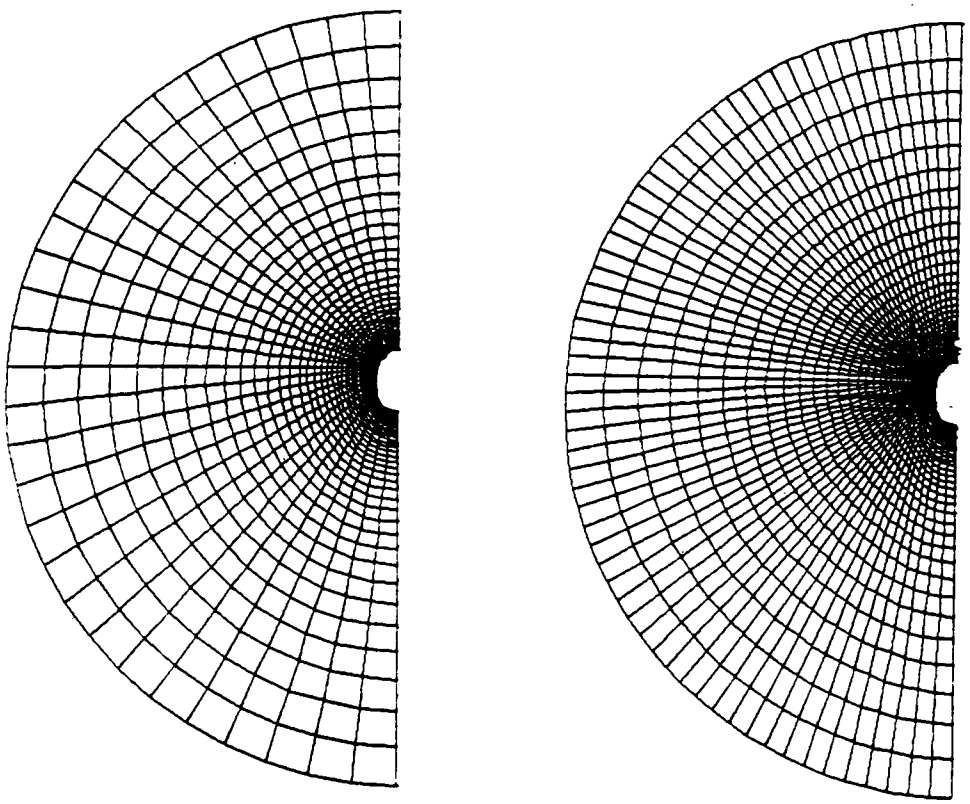

Figure 30. F-18 cross plane grid of (a) zone 1 and (b) zone 2 at the zonal interface.

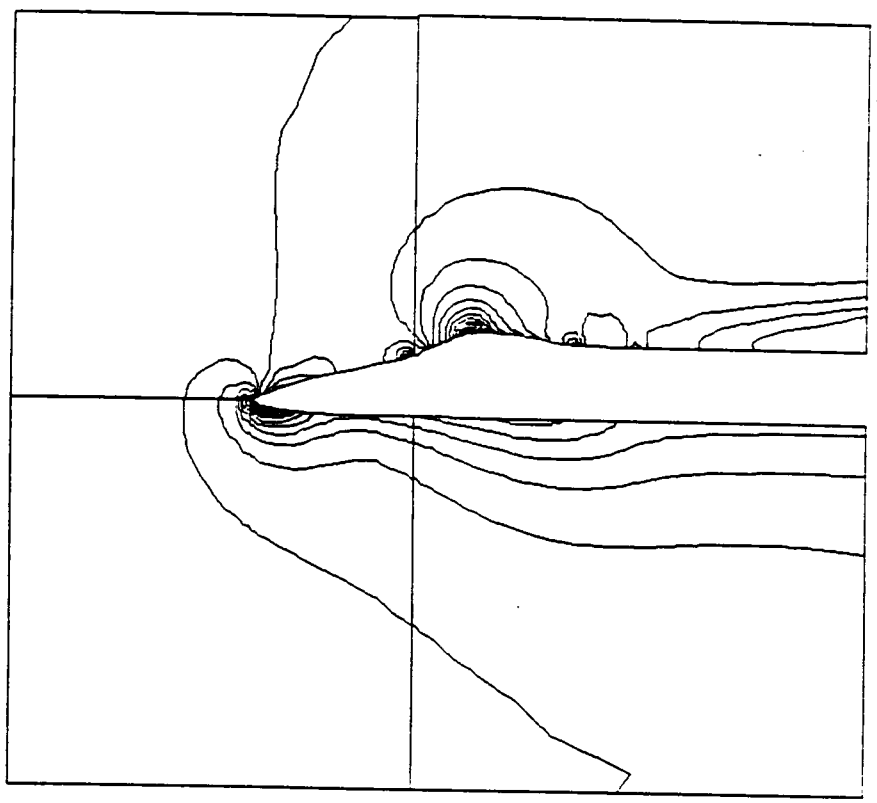

Figure 31. Pressure contours in the plane of symmetry.

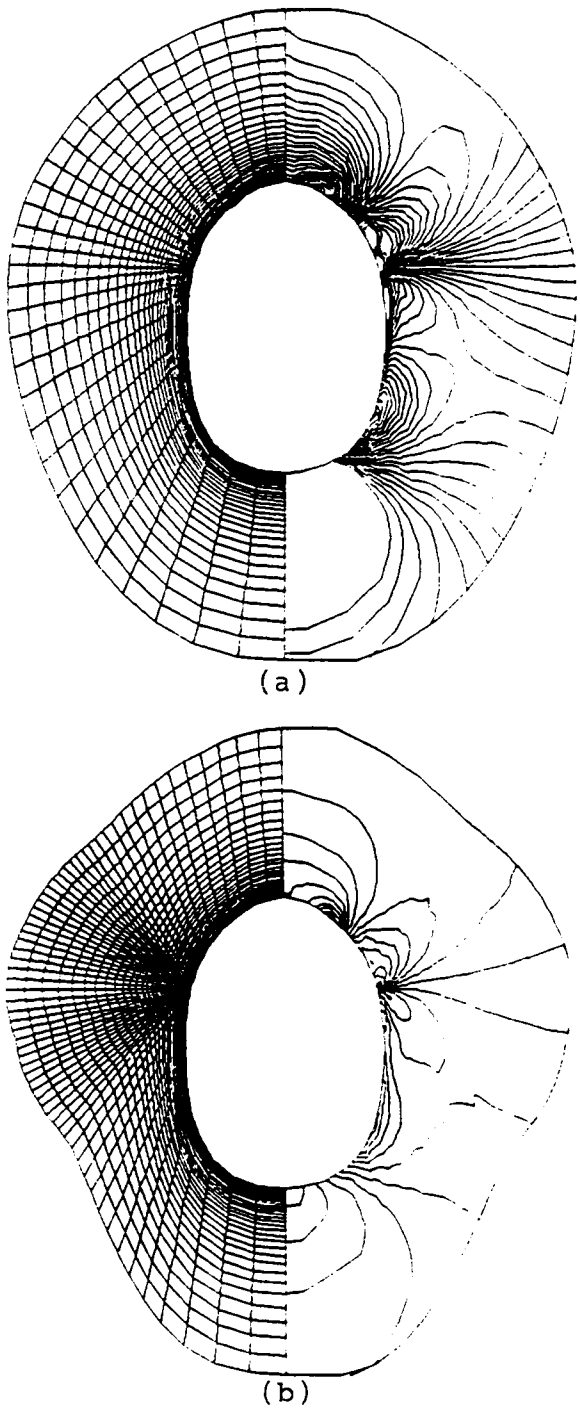

Figure 32. Enlarged view of pressure contours in the cross plane just (a) ahead of and (b) behind the zonal interface.

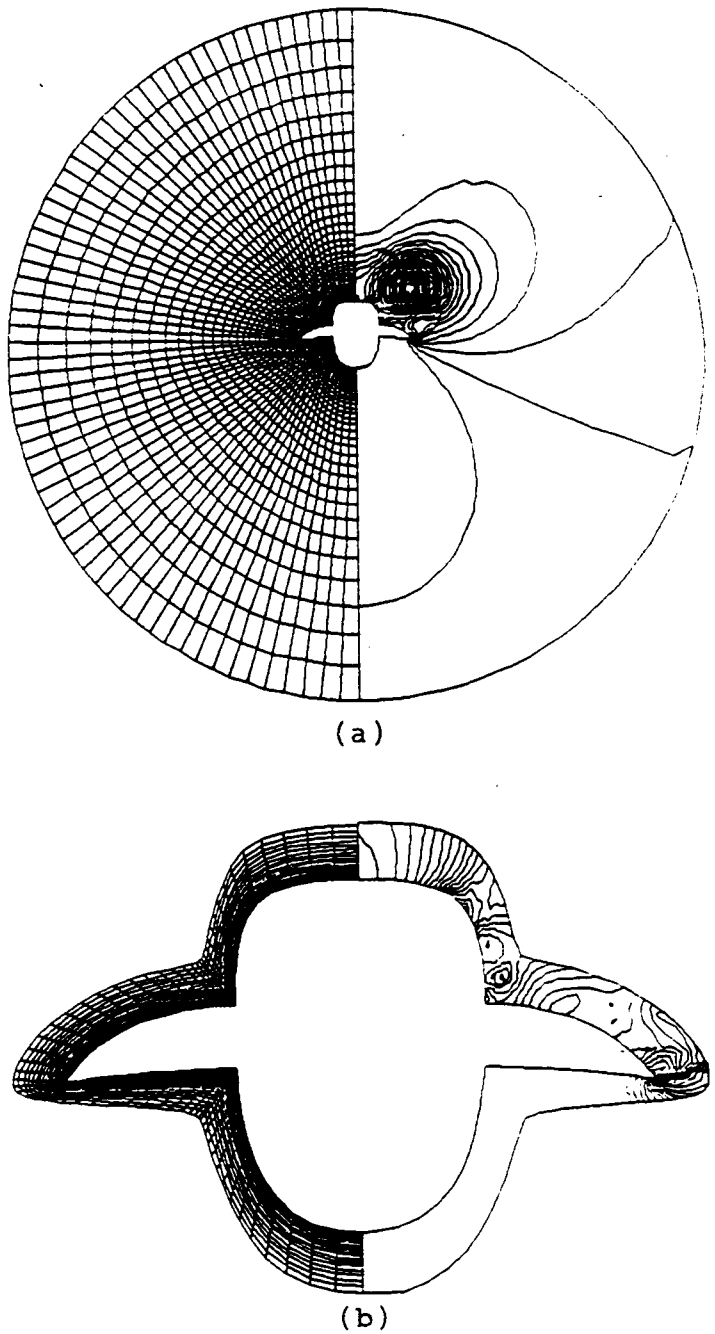

Figure 33. (a) pressure contours in the last plane and (b) the enlarged view.

Tables

Table 1.

Relative CPU time of Conservative Interpolation

Zone 1 Mesh	Zone 2 Mesh	Clipping	Ramshaw
11 x 11	11 x 11	13.3	1.0
21 x 21	21 x 21	208.9	3.9
31 x 31	31 x 31	1040.77	8.4
41 x 41	41 x 41	3271.4	14.9
32 x 32	52 x 52	3331.47	16.1

Appendix A. Nondimensionalization of the Navier-Stokes Equations

The vector form of the Navier-Stokes equations for an equilibrium gas in Cartesian coordinates without body forces or external heat addition can be written as

$$\frac{\partial \overline{Q}}{\partial \bar{t}} + \frac{\partial(\overline{F} - \overline{F}_v)}{\partial \bar{x}} + \frac{\partial(\overline{G} - \overline{G}_v)}{\partial \bar{y}} + \frac{\partial(\overline{H} - \overline{H}_v)}{\partial \bar{z}} = 0 \qquad (A-1)$$

where $\overline{Q}$ is the vector of conservative variables

$$\overline{Q} = [\overline{\rho}, \overline{\rho u}, \overline{\rho v}, \overline{\rho w}, \overline{\rho e}_0]^T$$

$\overline{F}$, $\overline{G}$ and $\overline{H}$ are flux vectors associated with the Euler equations which are

$$\overline{F} = [\overline{\rho u}, \overline{\rho u}^2 + \overline{p}, \overline{\rho u v}, \overline{\rho u w}, (\overline{\rho e}_0 + \overline{p})\overline{u}]^T$$
$$\overline{G} = [\overline{\rho v}, \overline{\rho u v} + \overline{p}, \overline{\rho v}^2, \overline{\rho u w}, (\overline{\rho e}_0 + \overline{p})\overline{v}]^T$$
$$\overline{H} = [\overline{\rho w}, \overline{\rho u w} + \overline{p}, \overline{\rho v w}, \overline{\rho u w}^2, (\overline{\rho e}_0 + \overline{p})\overline{w}]^T$$

$\overline{F}_v$, $\overline{G}_v$ and $\overline{H}_v$, which are flux vectors containing the shear stress and heat flux terms are given by

$$\overline{F}_v = [0, \overline{\tau}_{\bar{x}\bar{x}}, \overline{\tau}_{\bar{x}\bar{y}}, \overline{\tau}_{\bar{x}\bar{z}}, b_{\bar{x}}]^T$$
$$\overline{G}_v = [0, \overline{\tau}_{\bar{y}\bar{x}}, \overline{\tau}_{\bar{y}\bar{y}}, \overline{\tau}_{\bar{y}\bar{z}}, b_{\bar{y}}]^T$$
$$\overline{H}_v = [0, \overline{\tau}_{\bar{z}\bar{x}}, \overline{\tau}_{\bar{z}\bar{y}}, \overline{\tau}_{\bar{z}\bar{z}}, b_{\bar{z}}]^T$$

The shear stress and heat flux terms are given in tensor notation as

$$\overline{\tau}_{\bar{x}_i\bar{x}_j} = \overline{\mu}\left(\frac{\partial \overline{u}_i}{\partial \overline{x}_j} + \frac{\partial \overline{u}_j}{\partial \overline{x}_i}\right) + \overline{\lambda}\left(\frac{\partial \overline{u}_k}{\partial \overline{x}_k}\right)\delta_{ij}$$
$$b_{\bar{x}_i} = \overline{u}_j \overline{\tau}_{\bar{x}_i\bar{x}_j} - \dot{q}_{\bar{x}_i}$$
$$\dot{q}_{\bar{x}_i} = -k\frac{\partial \overline{T}}{\partial \overline{x}_i}$$

Here, unity Lewis number and equimolecular weights are assumed in the heat flux terms (Ref.61-62).

One of the many possible ways of nondimensionalization is to choose the freestream values as references.

$$x=\frac{\bar{x}}{\bar{L}} \qquad y=\frac{\bar{y}}{\bar{L}} \qquad z=\frac{\bar{z}}{\bar{L}}$$

$$t=\frac{\bar{t}}{\bar{L}/\bar{a}_\infty} \qquad u=\frac{\bar{u}}{\bar{a}_\infty} \qquad v=\frac{\bar{v}}{\bar{a}_\infty}$$

$$w=\frac{\bar{w}}{\bar{a}_\infty} \qquad p=\frac{\bar{p}}{\bar{\rho}_\infty \bar{a}_\infty^2} \qquad T=\frac{\bar{T}}{\bar{T}_\infty}$$

$$\rho e_0=\frac{\bar{\rho}\bar{e}_0}{\bar{\rho}_\infty \bar{a}_\infty^2} \qquad \mu=\frac{\bar{\mu}}{\bar{\mu}_\infty} \qquad \lambda=\frac{\bar{\lambda}}{\bar{\mu}_\infty}$$

$\bar{L}$ is the reference length used in the Reynolds number $Re_L=\dfrac{\bar{\rho}_\infty \bar{q}_\infty \bar{L}}{\bar{\mu}_\infty}$ where $\bar{q}^2=\bar{u}^2+\bar{v}^2+\bar{w}^2$.

Substituting the nondimensional relations into the Navier-Stokes equations results in the following nondimensional equations:

$$\frac{\partial Q}{\partial t}+\frac{\partial (F-F_v)}{\partial x}+\frac{\partial (G-G_v)}{\partial y}+\frac{\partial (H-H_v)}{\partial z}=0 \qquad (A-2)$$

where

$$Q=[\,\rho,\ \rho u,\ \rho v,\ \rho w,\ \rho e_0\,]^T$$

$$F=[\,\rho u,\ \rho u^2+p,\ \rho uv,\ \rho uw,\ (\rho e_0+p)u\,]^T$$

$$G=[\,\rho v,\ \rho uv,\ \rho v^2+p,\ \rho vw,\ (\rho e_0+p)v\,]^T$$

$$H=[\,\rho w,\ \rho uw,\ \rho vw,\ \rho w^2+p,\ (\rho e_0+p)w\,]^T$$

$$F_v=[\,0,\ \tau_{xx},\ \tau_{xy},\ \tau_{xz},\ b_x\,]^T$$

$$G_v=[\,0,\ \tau_{yx},\ \tau_{yy},\ \tau_{yz},\ b_y\,]^T$$

$$H_v=[\,0,\ \tau_{zx},\ \tau_{zy},\ \tau_{zz},\ b_z\,]^T$$

The shear stress terms are given in tensor notataion as

$$\tau_{x_i x_j} = \frac{M_\infty}{Re_L}\left[\mu\left(\frac{\partial u_i}{\partial x_j} + \frac{\partial u_j}{\partial x_i}\right) + \lambda \frac{\partial u_k}{\partial x_k}\delta_{ij}\right]$$

$$b_{x_i} = u_j \tau_{x_i x_j} - \dot{q}_{x_i}$$

$$\dot{q}_{x_i} = -M_\infty \frac{\mu}{Re_L} \frac{\bar{k}\bar{T}_\infty}{\bar{\mu}\bar{a}_\infty^2} \frac{\partial T}{\partial x_i}$$

$$M_\infty = \frac{\bar{q}_\infty}{\bar{a}_\infty} \qquad Re_L = \frac{\bar{\rho}_\infty \bar{q}_\infty \bar{L}}{\bar{\mu}_\infty}$$

$$q = (u^2 + v^2 + w^2)$$

The bulk viscosity, λ, is evaluated using Stokes hypothesis i.e., $\lambda + \frac{2}{3}\mu = 0$.

To simulate real gas effects, equilibrium air is considered as a real gas model. The simplified curve fits developed by Srivivasan et.al (Ref.25) are used to calculate the thermodynamic variables and the gas properties of equilibrium air. The pressure is given as a function of density and specific internal energy as

$$\bar{p} = \bar{p}(\bar{\rho}, \bar{e})$$

In addition,

$$\bar{T} = \bar{T}(\bar{p}, \bar{\rho})$$
$$\bar{\mu} = \bar{\mu}(\bar{e}, \bar{\rho})$$
$$\bar{k} = \bar{k}(\bar{e}, \bar{\rho})$$

For perfect gas calculations, the pressure is determined from the perfect gas law

$$p = (\gamma - 1)\left[\rho e_0 - \frac{\rho q^2}{2}\right]$$

The molecular viscosity is determined from the Sutherlands law

$$\mu = \left(\frac{\overline{\mu}}{\overline{\mu}_\infty}\right) = \left(\frac{\overline{T}}{\overline{T}_\infty}\right)^{\frac{3}{2}} \left(\frac{\overline{T}_\infty + \overline{c}}{\overline{T} + \overline{c}}\right)$$

where $\overline{c}$ is Sutherlands constant ($= 110.4°K$). The conductivity of gas is determined assuming $Pr = \overline{\mu}\overline{C}_p/\overline{k}$ is constant. Also, using the thermodynamic relations of the perfect gas, the heat flux terms, $\dot{q}_{x_i}$, can be written in terms of Prandtl number and speed of sound as

$$\dot{q}_{x_i} = -\frac{M_\infty \mu}{Re_L Pr(\gamma - 1)} \frac{\partial a^2}{\partial x_i}$$

where $Pr = \dfrac{\overline{C}_p \overline{\mu}}{\overline{k}}$.

Appendix B. Coordinate Transformation

For complicated body geometries, it is convenient to transform the governing equations from physical (x, y, z) space to computational (ξ, η, ζ) space. Consider a general transformation given by

$$\begin{aligned} \xi &= \xi(x, y, z) \\ \eta &= \eta(x, y, z) \\ \zeta &= \zeta(x, y, z) \\ t &= t \end{aligned} \qquad (B-1)$$

where $\Delta\xi = \Delta\xi_{i+\frac{1}{2}} - \Delta\xi_{i-\frac{1}{2}} = 1$ and likewise $\Delta\eta = \Delta\zeta = 1$.

Using the chain rule, the partial derivatives with respect to ξ, η, ζ become

$$\frac{\partial}{\partial\xi} = x_\xi \frac{\partial}{\partial x} + y_\xi \frac{\partial}{\partial y} + z_\xi \frac{\partial}{\partial z}$$

$$\frac{\partial}{\partial\eta} = x_\eta \frac{\partial}{\partial x} + y_\eta \frac{\partial}{\partial y} + z_\eta \frac{\partial}{\partial z}$$

$$\frac{\partial}{\partial \zeta} = x_\zeta \frac{\partial}{\partial x} + y_\zeta \frac{\partial}{\partial y} + z_\zeta \frac{\partial}{\partial z}$$

Solving the above equations and taking derivatives of ξ, η, ζ , the results are

$$\frac{\xi_x}{J} = y_\eta z_\zeta - z_\eta y_\zeta \qquad \frac{\eta_x}{J} = z_\xi y_\zeta - y_\xi z_\zeta \qquad \frac{\zeta_x}{J} = y_\xi z_\eta - z_\xi y_\eta$$

$$\frac{\xi_y}{J} = z_\eta x_\zeta - x_\eta z_\zeta \qquad \frac{\eta_y}{J} = x_\xi z_\zeta - z_\xi x_\zeta \qquad \frac{\zeta_y}{J} = z_\xi x_\eta - x_\xi z_\eta$$

$$\frac{\xi_z}{J} = x_\eta y_\zeta - y_\eta x_\zeta \qquad \frac{\eta_z}{J} = y_\xi x_\zeta - x_\xi y_\zeta \qquad \frac{\zeta_z}{J} = x_\xi y_\eta - y_\xi x_\eta$$

where J is the Jacobian of the transformation matrix and is given by

$$J = \left| \frac{\partial(x, y, z)}{\partial(\xi, \eta, \zeta)} \right|^{-1}$$

$$= [x_\xi y_\eta z_\zeta + x_\zeta y_\xi z_\eta + x_\eta y_\zeta z_\xi - x_\xi y_\zeta z_\eta - x_\eta y_\xi z_\zeta - x_\zeta y_\eta z_\xi]^{-1}$$

The spatial derivatives with respect to x, y and z can be written in ξ, η and ζ by using the chain rule as

$$\frac{\partial}{\partial x} = \xi_x \frac{\partial}{\partial \xi} + \eta_x \frac{\partial}{\partial \eta} + \zeta_x \frac{\partial}{\partial \zeta}$$

$$\frac{\partial}{\partial y} = \xi_y \frac{\partial}{\partial \xi} + \eta_y \frac{\partial}{\partial \eta} + \zeta_y \frac{\partial}{\partial \zeta}$$

$$\frac{\partial}{\partial z} = \xi_z \frac{\partial}{\partial \xi} + \eta_z \frac{\partial}{\partial \eta} + \zeta_z \frac{\partial}{\partial \zeta}$$

Applying the above transformation to the nondimensionalized Navier-Stokes equations in Cartesian coodinates, the results can be written in strong conservative form as

$$\frac{1}{J}\frac{\partial Q}{\partial t}+\frac{\partial}{\partial \xi}(\hat{F}-\hat{F}_v)+\frac{\partial}{\partial \eta}(\hat{G}-\hat{G}_v)+\frac{\partial}{\partial \zeta}(\hat{H}-\hat{H}_v)=0 \qquad (B-2)$$

where

$$Q=\begin{bmatrix}\rho\\ \rho u\\ \rho v\\ \rho w\\ \rho e_0\end{bmatrix} \qquad \hat{F},\ \hat{G},\ \hat{H}=\frac{|\nabla k|}{J}\begin{bmatrix}\rho\bar{u}\\ \rho u\bar{u}+\hat{\xi}_x p\\ \rho v\bar{u}+\hat{\xi}_y p\\ \rho w\bar{u}+\hat{\xi}_z p\\ (\rho e_0+p)\bar{u}\end{bmatrix}$$

and

$$\hat{F}_v,\hat{G}_v,\hat{H}_v=\frac{|\nabla k|}{J}\begin{bmatrix}0\\ \hat{k}_x\tau_{xx}+\hat{k}_y\tau_{yx}+\hat{k}_z\tau_{zx}\\ \hat{k}_x\tau_{xy}+\hat{k}_y\tau_{yy}+\hat{k}_z\tau_{zy}\\ \hat{k}_x\tau_{xz}+\hat{k}_y\tau_{yz}+\hat{k}_z\tau_{zz}\\ \hat{k}_x\beta_x+\hat{k}_y\beta_y+\hat{k}_z\beta_z\end{bmatrix}$$

$$\bar{u}=\hat{k}_x u+\hat{k}_y v+\hat{k}_z w$$

$$\hat{k}=\frac{k}{|\nabla k|}, \qquad \textit{for } k=\xi,\ \eta,\ \zeta, \quad \textit{respectively.}$$

The transformation shear stress and heat flux terms are given as

$$\beta_x = u\tau_{xx} + v\tau_{yx} + w\tau_{zx} - \xi_x\dot{q}_\xi - \eta_x\dot{q}_\eta - \zeta_x\dot{q}_\zeta$$

$$\beta_y = u\tau_{xy} + v\tau_{yy} + w\tau_{zy} - \xi_y\dot{q}_\xi - \eta_y\dot{q}_\eta - \zeta_y\dot{q}_\zeta$$

$$\beta_z = u\tau_{xz} + v\tau_{yz} + w\tau_{zz} - \xi_z\dot{q}_\xi - \eta_z\dot{q}_\eta - \zeta_z\dot{q}_\zeta$$

$$\tau_{xx} = \frac{M_\infty\mu}{Re_L}\left[\frac{4}{3}(\xi_x u_\xi + \eta_x u_\eta + \zeta_x u_\zeta) - \frac{2}{3}(\xi_y v_\xi + \eta_y v_\eta + \zeta_y v_\zeta + \xi_z w_\xi + \eta_z w_\eta + \zeta_z w_\zeta)\right]$$

$$\tau_{yy} = \frac{M_\infty\mu}{Re_L}\left[\frac{4}{3}(\xi_y v_\xi + \eta_y v_\eta + \zeta_y v_\zeta) - \frac{2}{3}(\xi_x u_\xi + \eta_x u_\eta + \zeta_x u_\zeta + \xi_z w_\xi + \eta_z w_\eta + \zeta_z w_\zeta)\right]$$

$$\tau_{zz} = \frac{M_\infty\mu}{Re_L}\left[\frac{4}{3}(\xi_z w_\xi + \eta_z w_\eta + \zeta_z w_\zeta) - \frac{2}{3}(\xi_x u_\xi + \eta_x u_\eta + \zeta_x u_\zeta + \xi_y v_\xi + \eta_y v_\eta + \zeta_y v_\zeta)\right]$$

$$\tau_{xy} = \tau_{yx} = \frac{M_\infty\mu}{Re_L}(\xi_y u_\xi + \eta_y u_\eta + \zeta_y u_\zeta + \xi_x v_\xi + \eta_x v_\eta + \zeta_x v_\zeta)$$

$$\tau_{xz} = \tau_{zx} = \frac{M_\infty\mu}{Re_L}(\xi_z u_\xi + \eta_z u_\eta + \zeta_z u_\zeta + \xi_x w_\xi + \eta_x w_\eta + \zeta_x w_\zeta)$$

$$\tau_{yz} = \tau_{zy} = \frac{M_\infty\mu}{Re_L}(\xi_y w_\xi + \eta_y w_\eta + \zeta_y w_\zeta + \xi_z v_\xi + \eta_z v_\eta + \zeta_z v_\zeta)$$

$$\dot{q}_k = -\frac{M_\infty \mu}{Re_L} \frac{\bar{k}\bar{T}_\infty}{\bar{\mu}\bar{a}_\infty^2} \frac{\partial T}{\partial k} \qquad for\ k = (\xi, \eta, \zeta)$$

Appendix C. Flow Chart of the Clipping Algorithm

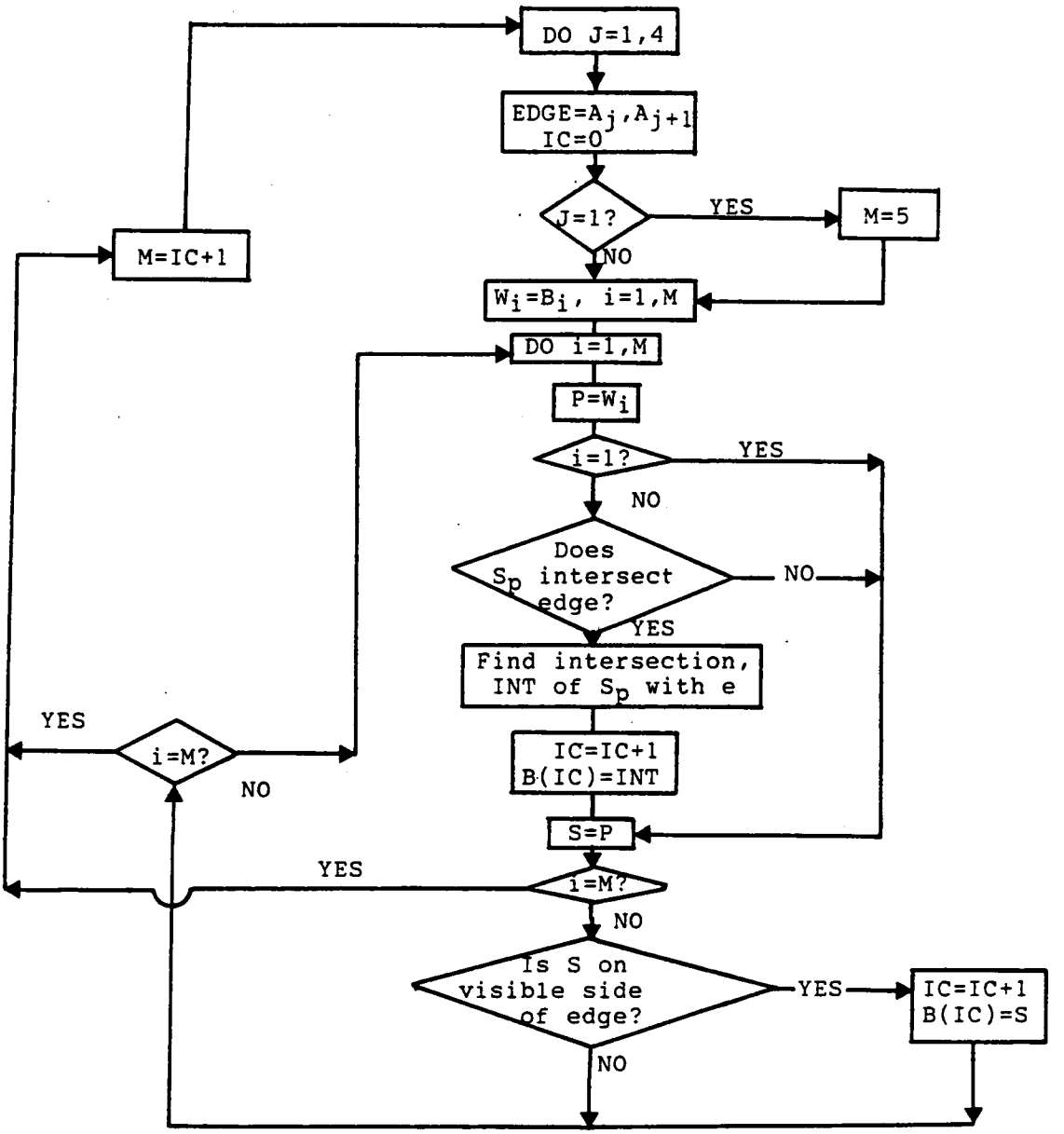
DO J=1,4
EDGE=A_j,A_{j+1}
IC=0
J=1?
YES
M=5
NO
M=IC+1
$W_i=B_i$, i=1,M
DO i=1,M
P=W_i
i=1?
YES
NO
Does S_p intersect edge?
NO
YES
Find intersection, INT of S_p with e
YES
i=M?
NO
IC=IC+1
B(IC)=INT
S=P
YES
i=M?
NO
Is S on visible side of edge?
YES
IC=IC+1
B(IC)=S
NO

Appendix D. Ramshaw algorithm

This appendix is a brief summary of the Ramshaw algorithm taken from Ref.46. The area of the polygon at the zonal interface, for example the shaded area in Fig.4, is given by

$$\Delta s^o = \frac{1}{2} \sum_s \varepsilon_s^P (y_1^s z_2^s - y_2^s z_1^s) \qquad (D-1)$$

where the summation is over all the sides s which are 'directed' line segments from point 1 to point 2 in each segment and ε_s^P is either +1 or -1 depending on whether the polygon lies to the left or to the right, respectively, of side s.

By realizing that each overlap increment, $[< \hat{F} > \Delta s^o]_{j1,k1}$ is itself the sum of contributions associated with the individual sides of the overlap area, one can evaluate these same contributions by simply sweeping over the sides or segments, s. If a side s is a segment of zone 1 then it is common to two adjacent cell faces

in zone 1, the left(L) cell face and the right(R) cell face. The L overlap area associated with side s lies entirely within the L cell face, whose averaged flux is $<\hat{F}>_{L^1}$, while the R overlap area lies entirely within the R cell face, whose averaged flux is $<\hat{F}>_{R^1}$. Both overlap areas lie entirely within the same cell face of the zone 2 grid and the contributions of sides s to $[<\hat{F}>\Delta s^o]_L$ and $[<\hat{F}>\Delta s^o]_R$ may be added to obtain the corresponding increment to $[<\hat{F}>\Delta s]_{j^2,k^2}$. According to Eq.(D-1), the contribution of side s to $[<\hat{F}>\Delta s^o]_L$ is $\frac{1}{2}<\hat{F}>_L(y_1^s z_2^s - z_1^s y_2^s)$, while that to $[<\hat{F}>\Delta s^o]_R$ is $-\frac{1}{2}<\hat{F}>_R(y_1^s z_2^s - y_2^s z_1^s)$. Therefore the flux of the zone 2 grid cell face containing side s is incremented by an amount

$$\Delta_s^1 = \frac{1}{2}(<\hat{F}>_L - <\hat{F}>_R)(y_1^s z_2^s - y_2^s z_1^s)$$

If a side s is a segment of the zone 2 grid then it is common to two adjacent cell faces of zone 2, the L and R cell faces. The L overlap area associated with side s lies entirely within the L cell face, while the R overlap area lies entirely within the R cell face. Both overlap areas common to side *s* lie entirely within the same cell face of the zone 1, whose averaged flux is $<\hat{F}>_{j^1k^1}$. The contribution of side s to $[<\hat{F}>\Delta s^o]_{L^1}$ will then be an increment to $[<\hat{F}>\Delta s]_{L^2}$, while that to $[<\hat{F}>\Delta s^o]_{R^1}$ will be an increment to $[<\hat{F}>\Delta s]_{R^2}$. The former contribution is

$$\Delta_s^2 = \frac{1}{2}<\hat{F}>_{j^1k^2}(y_1^s z_2^s - y_2^s z_1^s)$$

and the latter is just $-\Delta_s^2$. Therfore $[<\hat{F}>\Delta s]_{R^2}$ is to be decremented by the same amount. As a special case, when a line segment of the zone 2 coincides with a line segment of the zone 1, only the contribution of the zone 2 line segment is counted to avoid double counting.

Starting from boundary points in zone 1 and zone 2, this sweeping procedure is easily completed. First, sweep along k^2 = const. lines from $j^2 = 1$ to $j^2 = J^2$ in zone 2 and sweep along j^2 = const. lines from $k^2 = 1$ to $k^2 = K^2$ in zone 2. Repeat the procedure. In order to explain this in detail, suppose that we are sweeping along a particular line of zone 2, as shown in Fig.4 and that the work has just been done on segment $a\alpha$. We are located at the point a and are moving toward point b. We consider point a as endpoint 1 and we need to determine endpoint 2. During the determination of endpoint 2, it will be decided which zone 1 cell face the 'next' zone 2 segment will lie in. The procedure is summarized below.

1. Compute the intersection point of line segment ab with the line segments that form the N,S,E and W sides of the zone 1 cell face (J^1, K^1)

2. If there are no such intersection points then point s is endpoint 2 and it lies within cell face (J^1, K^1) of zone 1. For the next step, the point b becomes endpoint 1 and the above step is repeated. In this case, the next segment of the zone 2 line clearly lies in zone 1 cell face (J^1, K^1).

3. If there is an intersection point, then it defines endpoint 2, which is β in Fig.4. The next zone 2 segment will lie in the zone 1 cell face adjacent to the side

intersected by ab. In Fig.5, the 'next' zone 2 segment, bβ, will therefore lie in the zone 1 cell face (J^1, K^1 +1) which shares side N with cell face (J^1, K^1).

The procedure just outlined is simple and easy to program if the topological structure of the grid is used to determine which cell one enters upon leaving a given cell along a given line. However there are certain special cases which should be considered in programming. For an example, a line of one mesh can intersect with a vertex of the other mesh as seen in Fig.6a. In this case the next line segment location should be checked to determine which cell face the line segment enters. Throughout the calculations of this study, a tolerence ε which is based on the minimal grid length was used to resolve problems caused by round-off errors on the computer. If an end point of a sweeping line segment is close to a vertex point or line segment of the other mesh so that the distance is less than ε, the data of the end point was modified to lie exactly on the vertex point or the line segment of the other mesh as seen in Fig.6-a. Also, as an another case, sweeping along boundary grid lines should be treated in a special manner. Because, in the general case, 3-D solid body boundaries are curved, the boundary grid lines are not matched exactly to one another at the zonal interface as shown in Fig.6b. Though there may be several ways to handle this case, the extended grid was used in this study due to its simplicity in programming. As shown in Fig.6-b, ficticious cells which contain boundary grid lines of the other zone are considered along the boundary. The cell averaged fluxes of the ficticious cells are assumed the same as the boundary cell values. This boundary treatment was extended to handle the

branch cut in the second zone of SR-71 grid as seen in Fig.25-b and the the boundary cell values cross the branch cut were assigned to the ficticious cells.

The vita has been removed from the scanned document